INVESTIGATION OF TURBULENT JETS, SPRAYS, AND SUPERCRITICAL MIXING BY TIME RESOLVED RAINBOW SCHLIEREN DEFLECTOMETRY

by

CHRISTOPHER TABER WANSTALL

JOSHUA BITTLE, COMMITTEE CO-CHAIR
AJAY AGRAWAL, COMMITTEE CO-CHAIR
PAUL HUBNER
SUNDAR KRISHNAN
KALYAN SRINIVASAN

A DISSERTATION

Submitted in partial fulfillment of the requirements
for the degree of Doctor of Philosophy
in the Department of Mechanical Engineering
in the Graduate School of
The University of Alabama

TUSCALOOSA, ALABAMA

2020

ABSTRACT

As technological advancements have enabled higher efficiency compression ignition (CI) engines (diesel engines) by operating at higher pressures and temperatures, the mechanisms of fuel-air mixing are postulated to change. Thus, there is a greater need for experimental data to develop and verify new phenomena. However, the fast time scales and harsh environments associated with CI engines present many experimental difficulties and requires high quality non-intrusive diagnostics to obtain useful data. The diagnostics itself must be validated prior to its implementation in an engine environment.

The purpose of this research is to advance rainbow schlieren deflectometry (RSD) to study turbulent fuel sprays including the effects of supercritical mixing in CI engine environments. This objective is met by developing and applying quantitative RSD, for the first time, to three separate aspects of fuel sprays: 1) turbulent mixing, 2) phase boundaries, and 3) non-ideal gas mixing. First, quantitative RSD is demonstrated for turbulent mixing in a canonical helium jet. Rayleigh scattering data in the literature is used to validate the concentration measurements obtained by RSD. The results also provide explanations for phenomena occurring in the helium jet and provide data not yet present in the literature. Second, RSD is applied to high pressure multi-phase fuel sprays and new methodologies are developed to distinguish the liquid region from the vapor region and to quantify the in-between region on a probabilistic basis. Isolating liquid and vapor regions generally requires two separate diagnostics, e.g., Mie scattering (liquid region) and Rayleigh scattering (vapor region). However, the results of this study demonstrate that RSD can be used as a single diagnostic to measure both liquid and vapor boundaries. Third, the optical-to-thermodynamic relations associated with refractometry are investigated under non-ideal gas mixing conditions to develop a generalized relationship valid for both ideal or non-ideal gas mixing.

The last part of this research develops the theoretical tools to understand and experimentally realize supercritical mixing at diesel conditions. Guided by the theoretical analysis, RSD is applied to compare supercritical versus transcritical mixing at CI conditions using a constant pressure test rig. It is found that while fully supercritical mixing

offers benefits in diesel engines, i.e, faster mixing times (50% higher velocities), the absence of droplets which cause high levels of particulate emissions, etc., it would be difficult to achieve in practice because of the requirements of fuels with low critical temperature and/or substantial fuel preheating.

DEDICATION

To my dad, Chris Wanstall, and my grandfather, Dr. Eugene Carden, both engineers and men of God, who have taught me the key to wisdom is the humble pursuit of it.

LIST OF ABBREVIATIONS AND SYMBOLS

a Helmholtz Energy.

α Polarizability.

AP Additive Polarizability.

AR Additive Refractivity.

CFPR Constant Pressure Flow Rig.

CI Compression Ignition.

D Transverse Deflection Distance.

δ Full Width at Half Maximum (Chapter 2), Normalized Refractive Index (Chapter 4).

Dij Inversion Coefficients.

ECN Engine Combustion Network.

EOS Equation of State.

η Normalized Refractive Index.

f Focal Length.

Fr Froude Number.

g Gravitational Constant (Chapter 2,3,5), Gibbs function (Chapter 4).

H Hue.

h Enthalpy.

HSV Hue Saturation Value.

IG Ideal Gas.

κ Gladstone-Dale Constant.

ke Kinetic Energy.

L Liquid Length.

λ Light Wavelength.

M Molecular Weight.

μ Mean.

n Refractive Index.

P Pressure (Chapter 2,4,5), Liquid Probability (Chapter 3).

R Universal Gas Constant.

Re Reynolds Number.

r_e Effective Refractive Index.

ρ Density.

RSD Rainbow Schlieren Deflectometry.

Sc Schmidt Number.

σ Standard Deviation (Chapter 3), Rayleigh Scattering Cross Section (Chapter 4).

T Temperature.

θ Deflection Angle.

u Initial Velocity (Chapter 2), Internal Energy (Chapter 5).

$\dot{V}$ Volumetric Flow Rate.

X Mole Fraction.

z Axial Distance.

ACKNOWLEDGMENTS

First and foremost, I praise my only Rock and Redeemer, Jesus Christ, who gives me purpose. My life and work would be meaningless without your abiding love.

Next, I would like to give my inexpressible thanks to my patient and loving wife, Katrina. Her unwavering belief and support in me over the years is more than I could have ever asked for and has been my motivation when I needed it most.

I would also like to thank my parents, Chris and Rebekah Wanstall, who have always encouraged and supported me to pursue my dreams, and provided counsel when I have been unsure about the future.

I would like to express my gratitude to both of my advisors Dr. Ajay Agrawal and Dr. Joshua Bittle for providing me with the unique opportunity to pursue what I am passionate about and for encouraging me along the way. I am so grateful to have you both as mentors.

Next, I would like to thank my committee members Dr. Kalyan Srinivasan, Dr. Sundar Krishnan, and Dr. Paul Hubner for sacrificing their time to help review my work and provide invaluable insight that has increased the quality of this work.

Also, I would like to thank my present and former colleagues: Eddie Bogdanowicz, Kayla Bell, Danny Depperschmidt, Ross Depperschmidt, Zachary Harris, Mitch Johnson, Dalton Langner, Allen Loper, Rob Miller, Allen Parker, Shawn Reggeti, and Jonathan Tobias, many of whom have aided in the refinement of this dissertation through discussions, suggestions, or simply listening to my rambling thoughts.

Lastly, I would like to recognize all the people who work behind the scenes: Lisa Hinton, Genna Champion, Erika Hale, and Andrea Shepherd in the mechanical engineering office who ensure purchase ordering, payroll, and the completion of crucial tasks, making the lives of graduate students easier. I also thank all the machine shop employees, who have offered great assistance in manufacturing the parts needed for my work. The College of Engineering at the University of Alabama has provided me with opportunities that I

never imagined I would receive. For these, I will be thankful for the rest of my life.

CONTENTS

ABSTRACT ii

DEDICATION iv

LIST OF ABBREVIATIONS AND SYMBOLS v

ACKNOWLEDGMENTS vii

LIST OF TABLES xii

LIST OF FIGURES xix

1 INTRODUCTION 1

1.1 Background 1

1.2 Objective and Scope 5

2 QUANTITATIVE MIXING MEASUREMENTS IN A TURBULENT HELIUM JET USING RAINBOW SCHLIEREN DEFLECTOMETRY 8

2.1 Abstract 8

2.2 Introduction 8

2.3 Experimental Setup 10

2.4 Mathematical Background 12

2.5 Data Analysis 13

2.5.1 Rainbow Filter 13

2.5.2 Uncertainty Analysis 16

2.6 Results 17

2.6.1 Raw RSD Image Analysis 17

2.6.2 Quantitative RSD Image Analysis 18

2.6.3 Validation with Published Data 23

2.6.4 Full Field Measurements 28

2.6.5 Hardware Averaging 30
2.7 Conclusions 32

3 PHASE BOUNDARY DETECTION IN TRANSIENT, EVAPORATING HIGH-PRESSURE FUEL SPRAYS BY RAINBOW SCHLIEREN DEFLECTOMETRY 34
3.1 Abstract 34
3.2 Introduction 35
3.3 Experimental Setup 37
3.3.1 Constant Pressure Flow Rig (CPFR) 37
3.3.2 Rainbow Schlieren Deflecometry (RSD) 39
3.4 Data Analysis 40
3.5 Results 49
3.6 Discussion 52
3.7 Conclusions 57
3.8 Funding Information 58

4 IMPLICATIONS OF REAL-GAS BEHAVIOR ON REFRACTIVE INDEX CALCULATIONS FOR OPTICAL DIAGNOSTICS OF FUEL-AIR MIXING AT HIGH PRESSURES 59
4.1 Abstract 59
4.2 Introduction 59
4.3 Lorentz-Lorenz Equation 63
4.4 Polarizability Models 64
4.4.1 Single Component 64
4.4.2 Mixtures 66
4.5 Thermodynamic Models 66
4.5.1 Single Component 66
4.5.2 Mixtures 69
4.6 Refractive Index Models 70
4.6.1 Model Development 70

4.6.2 Model Validation 71
4.7 Application Examples 74
4.7.1 Adiabatic mixing and phase space 74
4.7.2 Model Comparison 77
4.7.3 Parametric Study 78
4.7.4 Supercritical Fuel-Oxidizer Mixing 81
4.8 Conclusions 82
4.9 Acknowledgements 84

5 CONSEQUENCES OF SUPERCRITICAL MIXING AT ENGINE RELEVANT CONDITIONS 85
5.1 Abstract 85
5.2 Introduction 85
5.3 Theoretical Background 87
5.4 Experimental Setup 98
5.4.1 Constant Pressure Flow Rig (CPFR) 98
5.4.2 Optical Diagnostics 100
5.5 Results 101
5.6 Conclusions 108

6 CONCLUSION 110
6.1 Summary 110
6.2 Future Scope and Recommendations 112

REFERENCES 113

LIST OF TABLES

2.1 **Helium jet flow conditions.** 11

3.1 **Operating conditions and camera specifications for different test cases.** 37

3.2 **Comparison of liquid boundary, outer liquid boundary and Siebers' model for the two n-heptane cases.** 54

5.1 **Air flow and fuel injection conditions for the CPFR along with camera acquisition rates.** 100

LIST OF FIGURES

1.1 Schematic illustrating dynamics of a subcritical fuel injection process. Reproduced from [81]. 2
1.2 Schematic illustrating dynamics of a supercritical fuel injection process. Reproduced from [81]. 3
2.1 Schematic of the experimental configuration. 10
2.2 Refractive index of a helium-air mixture versus helium mole fraction. . . 13
2.3 Profiles of several pixel-to-pixel calibration curves are shown. The solid-black, and red-dashed lines represent locations along the middle of the FOV image and along the centerline of the image, respectively. The hue prime filter is illustrated above the graph. 15
2.4 Combined instantaneous RSD images are shown for (a) $Re_0 = 800$ and (b) $Re_0 = 2500$. The black dashed line represents the middle of each FOV. . 19
2.5 Transition region shown for three different snapshots for $Re_0 = 800$. . . . 20
2.6 The frequency count of hue fluctuation via FFT analysis is shown for (a) $Re = 800$ and (b) $Re = 2500$. 21
2.7 An instantaneous (a) and average (b) deflection angle contours for $Re_0 = 2500$. 22
2.8 Average deflection angle as a function of the number of images is shown for (a) $Re_0 = 800$ and (b) $Re_0 = 2500$. The five different radial locations are at z=20 d for $Re_0 = 800$ and z=5 d for $Re_0 = 2500$. 23
2.9 (a) The deflection angle profile is shown along with the refractive index profile at z=20d for $Re = 800$. The unfiltered and filtered line are shown as the green-dashed and solid-red line, respectively. (b) The mole fraction profile is plotted along with the effect of velocity ($\pm 10\%$) on the mixing profiles at z=20d for $Re_0 = 800$. Uncertainty is shown as error bars for deflection angle, normalized refractive index, and mole fraction 24

2.10 (a) Non-dimensionalized and (b) absolute helium mole fraction helium mole fraction are presented (black lines) and compared with Ref. [107] (colored lines) for $Re_0 = 2500$. 25
2.11 The (a) full width at half maximum and (b) centerline mole fraction profiles are shown for $Re_0 = 2500$ and compared with Ref. [107]. 25
2.12 Mole fraction results are presented for Rayleigh scattering in Ref. [107] (colored lines) and RSD (black lines) for $Re_0 = 800$. Both (a) non-dimensionalized and (b) absolute helium mole fraction are shown. 27
2.13 The (a) full width at half maximum and (b) centerline mole fraction profiles are shown for $Re_0 = 800$ and compared with Ref. [107]. 28
2.14 Full field helium mole fraction for the case of $Re_0 = 800$ (left) and $Re_0 = 2500$ (right) 29
2.15 (Left) Radial profiles for $Re = 800$. (Right) Radial profiles for $Re = 2500$. 30
2.16 (Left) R^2 plotted versus axial distance for the location of 20d downstream. (Right) Two calibration curves are shown: a linear (solid green) and a non-linear (solid red) and their respective linear regression lines (dashed). 31
2.17 (a) Long exposure raw image for the case of $Re_0 = 800$ with (b) the results for mole fraction compared with Ref. [107]. 32
3.1 Constant pressure flow rig (CFPR) illustration. 38
3.2 Schematic of the RSD system. 39
3.3 The average liquid boundary of 2000 images during the quasi-steady period of a fuel spray is calculated using the RSD algorithm from Ref. [113] (red) and Mie scattering (black dashed-dotted). The results are compared to the liquid zone (blue-dashed line) determined from current RSD methodology. The boundaries are overlaid on the time-averaged Mie-scattering image. . 41

3.4 (Left) The HSI color space represented as a cone. (Right) A center plane slice from the HSI cone along the hue angle of 0° and 180 ° is shown. Regions A and B represent very low saturation with little and moderate attenuation occurring, respectively. Region C corresponds to significant attenuation, while D represents the area of reliable hue measurements. . . 42
3.5 (Top) An RGB snapshot of n-heptane at 245 C and 30 bar at 3.05ms aSOI. The corresponding hue (middle-top), saturation (middle-bottom) and intensity (bottom) images after converting from RGB to HSI. 43
3.6 Sensitivity analysis applied to Case 1 at 3.05 ms aSOI to determine the correct intensity threshold value. 44
3.7 (Top) The threshold comparison for a single injection. (Bottom) The 50 injection pixel count for Case 1 at 3.05 ms aSOI for all pixels above the threshold value. 45
3.8 Time evolution of injection count color-coded histogram for Case 1. . . . 46
3.9 All 90 centerline axial profiles of pixel count are plotted in gray during the quasi-steady period of the spray when the vapor has fully penetrated the field of view for Case 1. The mean of all 90 centerline profiles is shown as the red solid line. 46
3.10 Transient penetration of liquid, outer liquid and vapor penetration of Case 1. 49
3.11 Full liquid, outer liquid, and vapor cone angle versus time at an axial location of 15 mm for Case 1. The angles in this plot were calculated from the boundary from each color-coded histogram (Fig. 3.8) at each time step. 50
3.12 Full liquid, outer liquid, and vapor cone angle versus axial distance for the quasi-steady portion of the spray during Case 1. The cone angles in this plot were determined from an average of ninety boundaries of quasi-steady color-coded histograms in Fig. 3.8. 51
3.13 Transient evolution of injection count color-coded histogram for Case 3 consisting of 93 injections. 53

3.14 A liquid existence probability contour map is shown for the quasi-steady period of the spray. The inner and outer liquid boundary are as the solid black and dashed white lines, and represent the region of 95% and 0% probability, respectively. 55
3.15 Average saturation is determined for the quasi-steady period of the spray for Case 1. The liquid boundary (solid black curve) and outer liquid boundary (black long-dashed curve) are shown and compared to the liquid boundary using the methodology in Ref. [113] (black short-dashed line) 56
4.1 A plot showing the exponential of refractivity (r_e) based on the Lorentz-Lorenz (L-L) equation and the Dale-Gladstone (D-G) approximation for three different fuels. 64
4.2 Effect of pressure on polarizability of constituents of air (top) and hydrocarbons and carbon dioxide (bottom). The vertical axis shows the percent change in polarizability with respect to the value at STP (273 K and 1 bar) except 550 K and 1 bar for n-heptane. 65
4.3 Effect of pressure on density for hydrocarbons and carbon dioxide. The vertical axis shows the percent difference in density computed by real-gas and ideal gas models. Reference conditions are STP (273 K and 1 bar) except 550 K and 1 bar for n-heptane. 68
4.4 Refractive index difference versus pressure for a binary mixture of 78.2% CO_2 21.8% CH_4 at a temperature of 303 K compared with data from Ref. [48]. 73
4.5 Percent difference in predicted (by the AP model) and experimental refractive index data of Ref. [48] at a temperature of 303 [K]. 74
4.6 Temperature vs fuel mole fraction binary mixture of *n*-dodecane and nitrogen at Spray A conditions. The phase boundaries and vapor-liquid equilibrium region are also shown. 76
4.7 Equivalence ratio and mixture temperature as function of normalized refractive index difference for the IG, AR, and AP models. 77

4.8 Absolute error in the mixture temperature calculated using the IG model (ΔT=T$_{IG}$-T$_{AP}$) for n-dodecane and nitrogen as a function of ambient conditions (pairs for pressure and temperature assuming isentropic compression from P_i=2 bar T_i=360 K). The dashed white line represents the two-phase boundary. 79

4.9 Absolute error in the equivalence ratio calculated using the IG model ($\Delta\phi$=ϕ_{IG}-ϕ_{AP}) for n-dodecane and nitrogen as a function of ambient conditions (pairs for pressure and temperature assuming isentropic compression from P_i=2 bar T_i=360K) for gas phase mixtures. The solid and dashed white lines are error isolines of 5% and 10%, respectively. 79

4.10 Absolute error in the mixture temperature calculated using the AR model (ΔT=T$_{AR}$-T$_{AP}$) for n-dodecane and nitrogen as a function of ambient conditions (pairs for pressure and temperature assuming isentropic compression from P_i=2 bar T_i=360K). The dashed white line represents the two-phase boundary and the black dashed lines represent percent error isolines. 80

4.11 Absolute error in equivalence ratio is calculated using the AP and AR model ($\Delta\phi$=ϕ_{AR}-ϕ_{AP}) for n-dodecane and nitrogen as a function of ambient conditions (pairs for pressure and temperature assuming isentropic compression from P_i=2 bar T_i=360K) for gas phase mixtures. The right edge of the contour represents the phase boundary. Percent error isolines are overlaid as black dashed lines. 81

4.12 Calculated temperature versus fuel mole fraction for binary propane-nitrogen mixture at Spray A conditions using the IG, AR, and AP models. 82

4.13 Equivalence ratio and mixture temperature as function of normalized refractive index difference for binary propane-nitrogen mixture at Spray A conditions calculated using the IG, AR, and AP models. 83

5.1 Density contours versus pressure and temperature are shown for (a) nitrogen and (b) propane along the various thermodynamic regimes. 88

5.2 Phase diagram of a mixture with 80% propane and 20% nitrogen composition. The dashed and solid red line represents the saturated liquid and vapor lines, respectively. The individual vapor-liquid equilibrium lines are also shown for nitrogen (green) and propane (black) 91
5.3 Critical pressure (black line) and critical temperature (red line) are plotted versus propane mole fraction. 91
5.4 Adiabatic mixing lines are shown for propane mixing with nitrogen at 50 bar. The dashed lines represent where REFPROP failed to converge to a solution for the two-phase mixture. 92
5.5 Liquid-vapor equilibria is shown with respect to temperature and propane mole fraction. The dots represent the intersection of the saturated liquid and vapor lines. 94
5.6 A binary contour map is shown delineating fully continuous phase mixing versus the occurrence two-phase throughout the adiabatic mixing space. Nitrogen is kept at 500 K while propane inlet temperature is varied along with the ambient pressure. 95
5.7 96
5.8 A binary contour map is shown delineating fully continuous phase mixing versus the occurrence two-phase of propane injected into an environment of nitrogen at 50 bar and 500 K. The adiabatic mixing space is a function of the injection pressure and temperature where the injection state is modelled as (a) isenthalpic and (b) accounting for kinetic energy. 97
5.9 Adiabatic mixing lines (red lines) are show for an ambient pressure and temperature of (a) 50 bar and 500 K and (b) 30 bar and 300 K. Both cases start at the same injector conditions (190 bar and 417 K). The saturation lines for each case are shown in black. 98
5.10 Constant pressure flow rig (CPFR) illustration. 99
5.11 Illustration of the RSD system. 101

5.12 A sample raw RSD image is shown for a propane injected at 190 bar, 402 K into a (left) 30 bar, 300 K and (middle) 50 bar, 500 K ambient environment. The right image illustrates a high injection pressure of 1500 bar and 402 K into 50 bar, 500 K bar ambient environment. All images are at 4.58 ms ASOI. 102
5.13 The average jet penetration is shown versus injection duration for 30 bar (red line) and 50 bar (black line) along with a curve fit (green-dashed line) based on the analytical jet penetrations profiles from Ref. [80]. 104
5.14 Average jet velocity is plotted versus (a) time and (b) distance for 30 bar (red line) and 50 bar (black line). 105
5.15 The near field is visualized using RSD for a sample propane injection into a (a) 30 bar, 300 K and (b) 50 bar, 500 K ambient environment at 3.2 ms ASOI. 106
5.16 Liquid probability contour maps are shown for the (a) 30 bar case and (b) the 50 bar case at 3.2 ms ASOI. 108
5.17 The jet spreading angle is plotted for both the 30 bar (red line) and 50 bar (black line) at 3.2 ms ASOI. 109

CHAPTER 1
INTRODUCTION

1.1 Background

Driven by both a desire for improved system efficiency and the regulatory push towards increasingly stringent emissions standards, the need for clean combustion is imperative. The quality of any combustion process is highly influenced by the fuel-air mixture preparation. For example, in diesel engines, improved fuel-to-air mixing prior to ignition leads to a cleaner and more efficient process. Diesel engines operate by injecting fuel at extremely high pressures ($\approx 500 - 2000\,\text{bar}$) into the hot, compressed, dense air (or oxidizer) mixture, and then, the resulting fuel-air mixture auto-ignites. The time scale of the injection, mixing, and combustion process is typically on the order of one millisecond. Understanding and manipulating the fuel injection and mixing processes is a proven pathway to improved performance of these types of engines.

Classically, the fuel injection process is described as a high pressure liquid jet undergoing breakup, atomization, and vaporization and several other complex fluid mechanic sub-processes as shown in Fig. 1.1. This generic two-phase description has formed the basis of several conceptual and theoretic models in the literature [35, 78, 79, 105]. One observance from these studies is that the spray can be separated into two distinct zones depending upon the phase of the fuel. The liquid zone comprises the dense core with air entrainment in the near field and its subsequent breakup into ligaments and droplets. The vapor zone consists of the vaporized fuel mixing with the entrained ambient gas to form a combustible mixture. In practice, fuel droplets and vapor can exist concurrently in both zones. Thus, the liquid boundary is defined such that the liquid fuel is not detectable outside of it. Similarly, fuel vapor is not present outside of the vapor boundary. In the experimental spray literature, the liquid and vapor boundaries are commonly re-

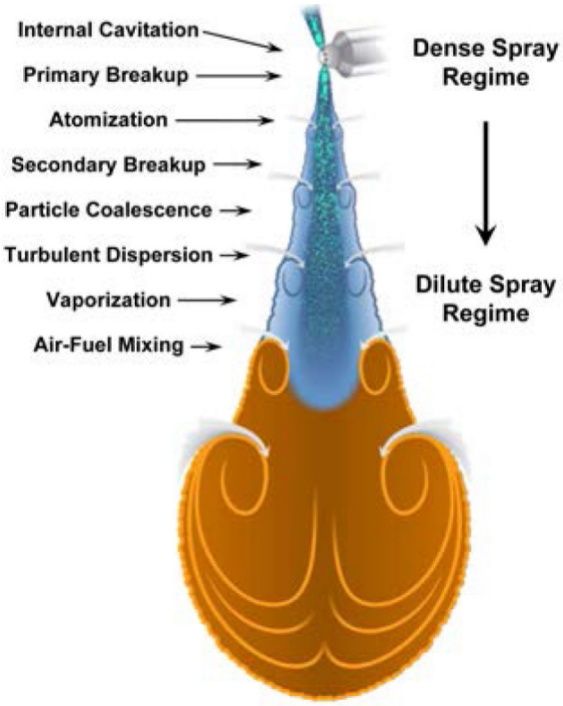

Figure 1.1: Schematic illustrating dynamics of a subcritical fuel injection process. Reproduced from [81].

ported to characterize the fuel-air mixing, for example, in terms of the cone angle and jet penetration distance versus time.

However, technological advancements that lead to higher intake pressures and compression ratios challenge the classic paradigm. As the ambient pressure is increased above the fuels critical pressure, the relative strength of surface tension of the fuel droplets is diminished. It is plausible that the decreasing role of inter-molecular forces can promote diffusion dominated mixing without the fuel atomization. In this scenario, turbulent diffusion dominated mixing occurs with continuously varying non-ideal thermodynamic and transport properties as shown in Fig. 1.2 [81]. Fully supercritical injection and mixing has been achieved in gasoline engines by substantially heating the fuel prior to injection and it has been shown to significantly reduce particulate emissions [34]. However, experimental observations reveal that the process in modern diesel engines follow a transcritical behavior where both classic evaporation and diffusive mixing are present [25, 42, 68].

The process of transcritical injection and mixing are not well understood. It is not clear if fully supercritical mixing in a diesel engine is realizable or under what condi-

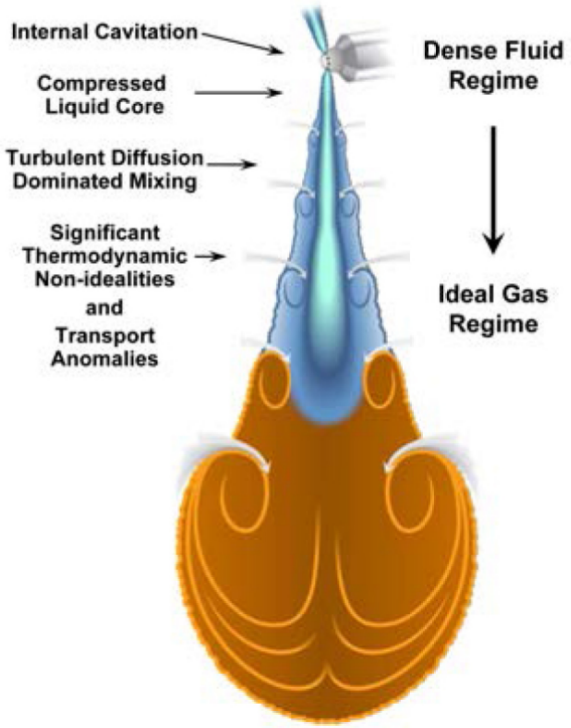

Figure 1.2: Schematic illustrating dynamics of a supercritical fuel injection process. Reproduced from [81].

tions the diffusive mixing overtakes as the dominant mechanism. Recently, Dahms and coworkers have produced several theoretical investigations of the interface dynamics of multicomponent mixtures transitioning to a supercritical state [26–28, 30]. These studies found that transition to a supercritical state is not only caused by a reduction in the surface tension but also by a reduction in the molecular mean free path at the interface and a broadening of the interface thickness. Thus, the transitional behavior is attributed to the following three factors: broadening interfaces (due to increasing temperature), reduction of mean free path (due to increasing pressure), and reduction in surface tension forces. Molecular dynamics simulations also showed that the two-phase interface at Spray A - the representative diesel condition outlined by the Engine Combustion Network (ECN) - does not diminish instantly; instead a gradual decrease occurs governed by non-equilibrium thermodynamics. Thus, high-fidelity experimental data are needed to improve the understanding of supercritical behavior in diesel engines.

Several experimental diagnostics have been developed for diesel spray and combustion studies, many of which are summarized and described by the ECN - an international col-

laboration among experimental and computational researchers in engine combustion [89]. Experimental diagnostics to evaluate the fuel-to-air mixing typically requires separate diagnostics in liquid and vapor zones in the spray. ECN summarizes recommendations using either Mie scattering or diffuse background illumination (DBI) to isolate the liquid zone [89]. Rayleigh scattering can be used outside the liquid zone to obtain the thermodynamic properties in the vapor zone assuming ideal gas mixing [41, 52]. Planar laser induced fluorescence (PLIF) has been used for mixing measurements in diesel sprays [85]. PLIF must ensure that the fluorescence properties of the fuel will not change during the experiment, thereby limiting it to mostly isothermal mixing applications. Existing experimental diagnostics constrained by isothermal mixing or ideal gas mixing makes it difficult to study super- or transcritical mixing processes under modern diesel engine conditions. Extending ideal gas limited diagnostics to possible non-ideal gas scenarios will limit the usefulness of acquired data. Therefore, advanced diagnostics applicable to non-isothermal mixing at real-gas conditions are needed.

Greenberg *et al.* [50] developed the Rainbow Schlieren Deflectometry (RSD) technique to overcome the limitations of the conventional line-of-sight techniques. In RSD, the knife-edge filter in a conventional grey scale schlieren system is replaced by a computer-generated rainbow (color) filter to quantitatively relate the angular deflection of a light ray to the color (or hue) in the rainbow schlieren image. RSD is based on Hue, Saturation, and Intensity (HSI) color model, and it employs digital imaging systems to facilitate quantitative measurements in non-reacting and reacting flows. RSD has been used to provide quantitative scalar flow measurements in simple canonical flows [4, 6, 7] and has also been applied to few practical flows [55, 86, 121] enabled by recent technological advancements in high intensity light sources and high-speed digital imaging systems. Recently, Agrawal and Wanstall [5] published a comprehensive review on the current development, implementation, and application of RSD to date. However, the RSD has not been applied to study fuel sprays except the this authors research group. Further, no study exists to demonstrate the ability of RSD to produce quantitative measurements in turbulent flows. Thus, the motivation of this dissertation is to develop the necessary tools and

methodology to study fuel-to-air mixing at high-pressure, supercritical conditions. This is achieved by 1) extending the RSD methodology to fuel sprays, and 2) understanding the relevant physics to achieve fully supercritical mixing in a diesel environment. The former will focus on the necessary modifications and considerations to adapt RSD to a fully turbulent two-phase (or single phase) non-ideal gas mixing environment. The latter will seek to answer the question, "Is fully supercritical mixing even possible in a diesel environment, and if so, what is the difference between a transcritical mixing state and a fully supercritical mixing state and does it offer potential path to improved diesel spray combustion in the future?".

1.2 Objective and Scope

The scope of this research encompasses building the necessary tools to evaluate supercritical mixing behavior is diesel engines. Thus, Chapter 2 applies RSD to investigate turbulent flows for the first time, and demonstrates its potential to acquire quantitative mixing measurements. Chapter 2 applies RSD to simultaneously identify, for the first time, liquid and vapor boundaries in two-phase flows at diesel conditions. Chapter 3 develops the theoretical background to apply RSD in non-ideal gas scenarios including supercritical conditions. Finally, Chapter 5 applies RSD to evaluate supercritical mixing in an optically accessible constant pressure test chamber to replicate diesel spray behavior. Following is a brief summary of the contents of these fours chapters to meet the objectives of the present research.

Chapter 2: Quantitative mixing measurements in a turbulent helium jet using rainbow schlieren deflectometry

> Although RSD has been used in several applications over the 20 plus years of research, RSD has never been validated in a turbulent environment to provide quantitative thermodynamic mixing measurements. Thus, the purpose of this work is to replicate and validate a canonical axisymmetric initially laminar helium jet. The outcome is to provide mixing measurements in several regions of the jet with

quantifiable uncertainty as well as give insight to binary gas jet mixing behavior. The methodology developed in this work provides the first step toward applying RSD in a fuel spray environment.

Chapter 3: Phase boundary detection in transient, evaporating high-pressure fuel sprays by rainbow schlieren deflectometry

One problem in two-phase fuel sprays is that the presence of liquid corrupts the signal when measuring vapor zone mixing measurements. Traditionally, this has required a separate diagnostic to delineate between the liquid zone and the vapor zone. The purpose of this work is to build a methodology using RSD to not only separate the liquid region of the spray but quantify liquid existence on a probabilistic basis. The objective of this study will bring to fruition the possibility of RSD to simultaneous quantify liquid existence and provide vapor zone mixing measurements. This chapter presents a new alternative application of RSD: quantifying line of sight liquid existence.

Chapter 4: Implications of real-gas behavior on refractive index calculations for optical diagnostics of fuel-air mixing at high pressures

Current optical-to-thermodynamic relations used in several optical diagnostics such as RSD and Rayleigh scattering assume ideal gas mixing. Often, these diagnostics are extended to situations where ideal gas mixing may not be valid, e.g., fuel-to-air mixing in diesel environments. It is not clear when the current implementation of these diagnostics become invalid. Thus, this chapter investigates the impact of fuel-to-air mixing at high pressure conditions on mixture optical and thermodynamic behaviors. The outcome provides a generalized optical to thermodynamic relationship valid ideal or non-ideal gas mixing situations, providing the necessary tools to extend RSD to non-ideal gas regions of fuel sprays.

Chapter 5: Consequences of supercritical mixing at engine relevant conditions

This study investigates the prerequisites required to obtain fully supercritical in a diesel-like environment by delving into the thermodynamics of binary mixtures.

The theoretical development is then experimentally applied to an optically accessible spray chamber. The experiments conducted in this work consist of injecting 100 injections of supercritical propane into a supercritical and subcritical environment of nitrogen to evaluate the differences between fully supercritical mixing and transcritical mixing. Rainbow schlieren deflectometry is used to quantify global parameters in the jet evolution as well as liquid existence. The results show differences in jet penetration, spreading rate, and jet velocity. The differences are attributed to observed condensation and low density expansion occurring at a microscopic level near the injector.

CHAPTER 2
QUANTITATIVE MIXING MEASUREMENTS IN A TURBULENT HELIUM JET USING RAINBOW SCHLIEREN DEFLECTOMETRY

2.1 Abstract

Rainbow schlieren deflectometry (RSD) is successfully applied to acquire quantitative concentration measurements in a turbulent environment for the first time. The RSD methodology is developed and validated using Rayleigh scattering data available in the literature. Experiments were performed in an initially laminar, momentum-driven helium jet injected into ambient air. Full-field measurements are acquired that span the laminar, transition, and fully turbulent regions of the jet. RSD is shown to provide accurate measurements in the turbulent regions, and it also confirms the self-similar nature of the fully turbulent jet. Analysis shows that the transition occurs across an axial span that decreases with increasing Reynolds number. Experiments with long exposure times were conducted to show that the hardware averaging of the RSD signal is acceptable only if the rainbow filter is linear. The methodology developed in this work provides the first step toward applying RSD in a fuel spray environment.

2.2 Introduction

Turbulent jets have been the subject of interest from the time of Prandtl's mixing length theory [95] to recent efforts in understanding the entrainment mechanisms along the shear layer [77, 116]. Canonical systems, such as binary mixing in an axisymmetric turbulent jet, offer insight into the underlying phenomena without the practical complexities, e.g., the relevant combustion processes in diesel or gas turbine engines. Several studies of turbulent binary gas jet mixing have been reported in the literature to provide

detailed scalar measurements using intrusive techniques (hot-wire anemometry, interference probes, etc.) and optical techniques such as laser induced fluorescence and Rayleigh scattering.

Papanicolaou and List [83] obtained a comprehensive set of velocity and concentration measurements in buoyant jets using laser Doppler anemometry and laser induced fluorescence. Dowling and coworkers [38–40] used Rayleigh scattering to show that the constant density axisymmetric jets exhibit self-similarity behavior in the full turbulent region. Pitts *et al.* [92–94, 97] also used Rayleigh scattering to demonstrate self-similarity in variable density jets. They concluded that the variable density jets reach an asymptotic scaling state regardless of the initial conditions contingent on a fully developed, momentum driven regime. Westerweel *et al.* [118, 119] used planar laser induced fluorescence (PLIF) and particle image velocimetry (PIV) to show that the entrainment at the turbulent/nonturbulent interface is dominated by a partially viscous process caused by irregular small-scale eddy motions. More recent PIV/PLIF measurements have been used to evaluate the roles of large scale engulfment versus small scale (local) entrainments at the interface have shown power-law scaling in the entrained velocity [77].

Path integrated techniques such as interferometry and schlieren deflectometry have also been used in conjunction with a deconvolution procedure to obtain the local scalar measurements in turbulent jets. Watt and coworkers [88, 117] applied interferometry coupled with computed tomography to obtain the 3-D density field in a turbulent helium jet. Davis [31–33] implemented a single beam laser schlieren system to measure fluctuation intensity along the shear layer in subsonic and supersonic turbulent jets. Kolhe and Agrawal [56] developed a spectral analysis algorithm to provide local scalar statistics in turbulent flows applicable to any deflectometric line of sight diagnostic, e.g., rainbow schlieren deflectometry (RSD).

In the past 25 years, RSD has been used extensively for measurements in laminar flows [4, 5, 7, 86, 122]. However, so far it has not been validated for quantitative mixing measurements in turbulent flows. Thus, the objective of this study is twofold: 1) validate quantitative RSD for scalar measurements in a turbulent helium jet, and 2) gain insight

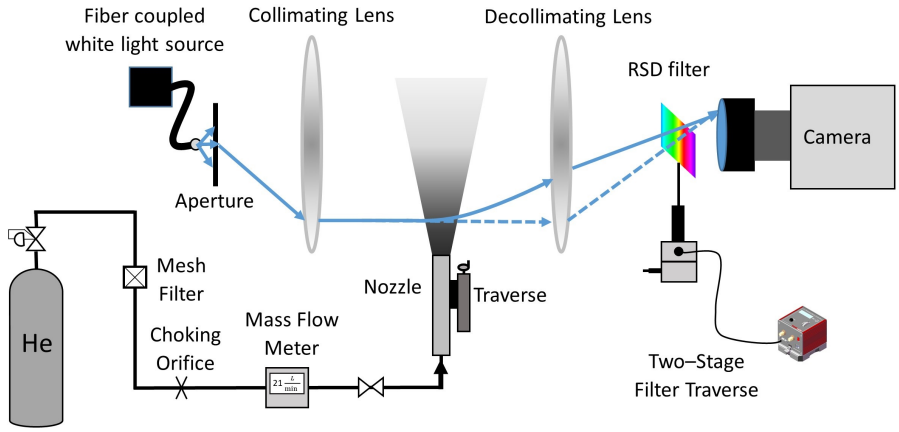

Figure 2.1: Schematic of the experimental configuration.

into the jet mixing behavior including the transition region. This study is an important step towards the use of the quantitative RSD to advanced applications such as fuel-air mixing in diesel sprays [113, 114]. This study is divided into five sections. First, the experimental details are provided. Next, the theory to apply RSD in a turbulent flow field is developed, followed by the data acquisition and post processing details. Then, RSD results are compared with Rayleigh scattering from Ref. [107], and other supplementary measurements are presented. Lastly, the key finding from this study are summarized.

2.3 Experimental Setup

Figure 2.1 illustrates schematic of the test setup and RSD optics used in this study. Pressure regulated bottled helium filtered with a 30 μm mesh filter passes through a 200 μm choking orifice to prevent the flow oscillations. A GM3 Dakota flow meter measures the mass flow rate to infer a bulk jet velocity at the tube exit. A ball valve downstream of the flow meter controls the supply of helium to the experiment. Once the valve is opened, helium issues vertically upward into quiescent ambient air through a stainless steel tube with an inner diameter (d), outer diameter (d_o), and length (l) of 4.6 mm, 6.35 mm, and 44d, respectively. The tube is translated by a traverse to vary the field of view (FOV) of jet flow with respect to the stationary imaging system. Note that the co-flow reported as negligible by Ref. [107] is not replicated in this work.

Figure 2.1 also shows the RSD system used in this study. The RSD system was

Table 2.1: **Helium jet flow conditions.**

$\dot{V}$ ($^{L}/_{min}$)	u_0 ($^{m}/_{s}$)	Re_0	$z_{Fr,max}$	z/d_{max}
21.7	21.7	800	1.31	32
66.5	66.5	2500	0.27	20

optimized following recommendations by Agrawal and Wanstall [5]. An Energetiq EQ-99X continuous laser driven light source emits high intensity broadband light through a 100 µm fiber optic that terminates at a 30 µm wide 3 mm high rectangular aperture. The emerging light is collimated by a 250 mm focal length 76 mm diameter achromatic doublet lens. Upon collimation, light rays propagate through the test media and refract according to the local density gradients. The refracted light rays are color encoded by a 0.6 mm wide asymmetric rainbow filter with a hue range of -120 to 200 degrees mounted on a two-stage traverse. The two stages consist of a motorized stage (ThorLabs KDC101) in the transverse direction to automate calibration and a manual stage in the axial direction to precisely locate the filter at the focal plane of the decollimating lens. A Photron SA5 color camera outfitted with a 50 mm focal length Nikon Nikkor lens (spatial resolution of 100 $^{\mu m}/_{px}$) acquires the color images. RSD images are acquired at sampling rate of 250 Hz for sample duration of 20s using the system's lowest reliable exposure time of - 14 µs.

Table 2.1 provides the flow conditions for the two test cases with both helium and ambient air at room temperature/pressure conditions. Chen and Rodi [22] introduced the non-dimensional axial coordinate, z_{Fr} in Eq. 2.1 to demarcate the flow regimes.

$$z_{Fr} = Fr^{-1/2}\left(\frac{\rho_\infty}{\rho_0}\right)^{\frac{1}{4}}\frac{z}{d}, \quad Fr = \frac{\rho_0 u_0^2}{gd(\rho_\infty - \rho_0)} \tag{2.1}$$

where Fr is the Froude number and $\frac{\rho_\infty}{\rho_0}$) is the density ratio. For $z_{Fr} < 1$, the flow is momentum dominated, buoyancy effects are negligible, and the resulting flow follows similarity scaling. For $1 < z_{Fr} < 5$, the flow is transitional with both buoyancy and momentum effects present [83]. For $z_{Fr} > 5$, plume-like, buoyant behavior pertains. As shown in Table 2.1, the $Re_0 = 800$ case includes both buoyant and momentum driven regimes, whereas the $Re_0 = 2500$ case is momentum dominated.

2.4 Mathematical Background

In this study, RSD is configured to measure the transverse deflection angle of light rays (θ_x) related to the normalized refractive index difference (η) according to Eq. 2.2 [5]

$$\theta_x(x,z,t) = \int_{-\infty}^{\infty} \frac{\partial \eta}{\partial x}\Big|_{x,y,z,t} dy, \quad \eta = \frac{n}{n_0} - 1 \tag{2.2}$$

where n is the local refractive index and n_0 is the refractive index surrounding the test media. In a turbulent flow, Eq. 2.2 can be replaced by Eq. 2.3 where the overbar and apostrophe represent the mean and fluctuating components, respectively.

$$\overline{\theta_x}(x,z,t) + \theta_x'(x,z,t) = \int_{-\infty}^{\infty} \frac{\partial \overline{\eta}}{\partial x}\Big|_{x,y,z,t} + \frac{\partial \eta'}{\partial x}\Big|_{x,y,z,t} dy \tag{2.3}$$

For statistically stationary processes, the averaging procedure simplifies to Eq. 2.4, where the limiting process converges to a well-defined value [64].

$$\lim_{T\to\infty} \frac{1}{T} \int_0^T \theta_x(x,z)dt = \overline{\theta}_x(x,z) \tag{2.4a}$$

$$\lim_{T\to\infty} \frac{1}{T} \int_0^T \int_{-\infty}^{\infty} \frac{\partial \eta}{\partial x}\Big|_{x,y,z} dydt = \int_{-\infty}^{\infty} \frac{\partial \overline{\eta}}{\partial x}\Big|_{x,y,z} dy \tag{2.4b}$$

$$\overline{\theta}_x(x,z) = \int_{-\infty}^{\infty} \frac{\partial \overline{\eta}}{\partial x}\Big|_{x,y,z} dy \tag{2.4c}$$

Note that the limits of integration remain the same when swapping the integration order in Eq. 2.4b.

For a circular jet, the time-averaged turbulent flow is axisymmetric, and thus, Abel transform [14] can be used to invert Eq. 2.4c to determine the refractive index difference. In this study, the discretized two-point formula to minimize inversion errors in deflectometric measurements given by Eq. 2.5 is used [54].

$$\overline{\eta}(r_i,t) = \sum_{j=i}^{N+1} D_{ij} \overline{\theta}_x(x_j,t) \tag{2.5}$$

Thus, the normalized refractive index difference simplifies to weighted linear combination

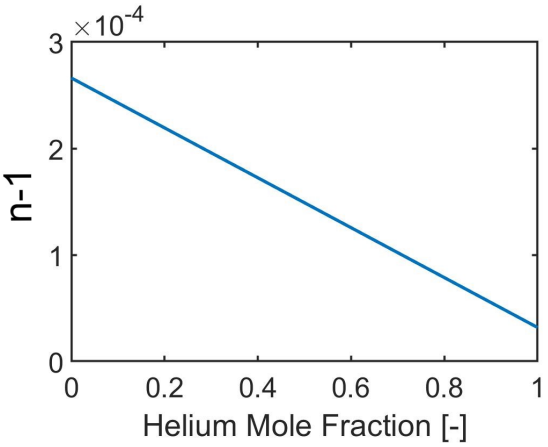

Figure 2.2: Refractive index of a helium-air mixture versus helium mole fraction.

of measured deflection angles.

For ideal gas mixtures, the refractive index difference is related to thermodynamic properties using Eq. 2.6.

$$n - 1 = \frac{P}{RT} \sum_i M_i \kappa_i x_i \tag{2.6}$$

Where P, R, T, M, κ, and x are the pressure, universal gas constant, temperature, molecular weight, Gladstone-Dale constant, and mole fraction, respectively, and the subscript 'i' refers to each species in the mixture. The Gladstone-Dale constants for helium and air are $\kappa_{he} = 1.96 * 10^{-4}$ and $\kappa_{air} = 2.27 * 10^{-4}$. Figure 2.2 shows the refractive index difference versus helium mole fraction given by Equation 2.6. Because of the linear relationship, Figure 2.2 can be used to determine the average helium mole fraction from the average reflective index difference. In summary, the average deflection angle in an axisymmetric turbulent jet can be converted to the average helium mole fraction as long as the process is statistically stationary.

2.5 Data Analysis

2.5.1 Rainbow Filter

RSD uses a rainbow filter to measure the ray deflection angle in the transverse direction (x) for the present setup. The rainbow filter, shown above the calibration curve in Fig. 2.3, is a transparent slide with digitally printed color gradations to color-code the deflected light rays depending upon the transverse distance (D) on the filter plane. For

small deflections, the deflection angle can be calculated from Eq. 2.7 [110].

$$\theta = \frac{D - D_0}{f} \tag{2.7}$$

where f is the focal length of the decollimating lens and (D_0) is the reference distance without ray deflection. Colors in the RSD image provide a quantitative measure of the numerator in Eq. 2.7, and hence, the ray deflection angle at every time and every pixel location in the FOV.

RSD uses a single parameter, hue (H), to quantify color from the three signals Red (R), Green (G) and Blue (B) or RGB acquired by a color camera [50]. However, filter calibration is required to establish the proper mapping between the hue in the RSD image and the transverse location on the filter plane. Filter calibration is achieved in the absence of the test media by recording image(s) at each filter location to correlate the background image hue and the transverse location of the filter. Two calibration procedures are possible: an average and a pixel-to-pixel calibration. The former computes one calibration curve representative of the average hue in a window of pixels in the FOV, while the latter provides a calibration curve for every pixel in the FOV. The average calibration is easy to implement, albeit at the expense of accuracy and greater uncertainty. In this study, high fidelity measurements are obtained by using a pixel-to-pixel calibration.

The calibration process begins with establishing the appropriate parameters (framing rate, exposure time, etc.) for the experiment. Then, the filter is traversed in small increments (UX) to acquire the background RSD images. For high accuracy, the step size should be approximately the print resolution of the filter to minimize the interpolation errors. In this study, the step size is $Ux = 6\mu m$ - slightly above the print resolution of 4 μm. The filter calibration process is automated to accommodate such small steps. In this experiment, 17 images were recorded at each location to achieve hue variation of less than 0.5° at nearly all pixel locations within the FOV (>99%).

The typical hue range in RSD studies is 0 to 2π with the filter centered at π (cyan). In this study, the hue varies from -$2\pi/3$ to $10\pi/9$ centered at $2\,\pi/9$ or 40°. This unorthodox approach is motivated by the high absorptivity of the filter in the dark blue region ($200° -$

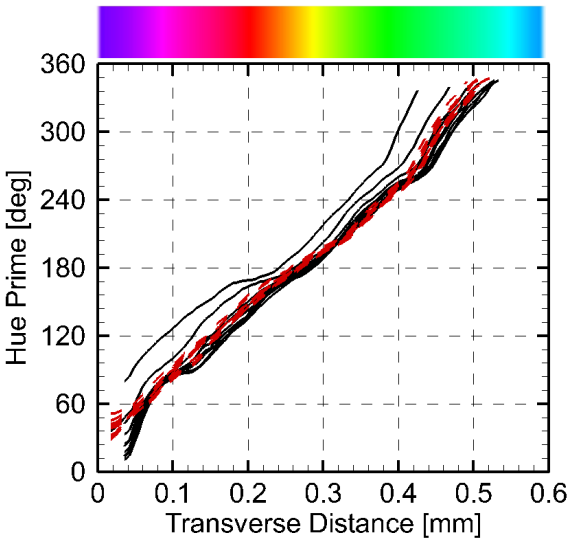

Figure 2.3: Profiles of several pixel-to-pixel calibration curves are shown. The solid-black, and red-dashed lines represent locations along the middle of the FOV image and along the centerline of the image, respectively. The hue prime filter is illustrated above the graph.

240°) that limited the exposure time. Thus, this region was excluded by transforming the hue into hue prime H' using Eq. 2.8

$$H' = \begin{cases} H + \frac{10\pi}{9}, & \text{if } H \leq \frac{8\pi}{9} \\ H + \frac{10\pi}{9} - 2\pi, & \text{otherwise} \end{cases} \tag{2.8}$$

This transformation ensures the continuity of H' at the $0/2\pi$ location. To the author's knowledge, this is the first time a rotated hue coordinate system, to overcome the filter linearity issues, has been used in an RSD study. Figure 2.3 shows an image of the hue prime filter and calibration curves at multiple pixel locations. The solid black curves represent pixels at various radial locations along the dashed region in Fig. 2.4, whereas the red-dashed curves represent different pixels along the centerline of the image. Both radial and axial variations in the calibration curves arise because of printing imperfections, minor optical aberrations, and pixel variations across the camera sensor. Figure 2.3 also shows that even though the filter is linearly prescribed slight non-linearities manifest from the aforementioned effects. Figure 2.3 shows that an average calibration curve would introduce unwarranted errors. Thus, a pixel-to-pixel calibration process is highly

recommended for turbulent flow applications.

2.5.2 Uncertainty Analysis

In RSD, hue is the primary measurement. Uncertainty propagation begins with uncertainty in hue prime ($U_{H'}$). Note that $U_{H'}$ only contains precision uncertainty caused from fluctuations in the light source, camera, etc. The pixel-to-pixel calibration process provides a new reference for each color effectively driving bias uncertainty from the camera to zero. If an average calibration procedure is implemented bias uncertainty is not zero and must be included. It is possible to have an uncertainty component from translation slide, however, the stepper motor used in this study has an uncertainty of $\pm 0.1\mu$m which corresponds to 0.05° - much smaller than the precision uncertainty in hue. Equations 2.9a-2.9f show all sources of uncertainty present in this study.

Precision uncertainty in Eq. 2.9a is determined from the standard deviation, σ_{cal}, at each pixel in the 25 images acquired at each transverse location. Therefore, σ_{cal} is a function of transverse filter location and pixel location in the image. The degrees of freedom for σ_{cal} is reduced by considering each pixels average transverse deflection distance during the experiment to provide a unique σ_{cal} for each pixel in the image. This procedure is performed for all uncertainty variables that are functions of both pixel location and transverse deflection distance, e.g., σ_Θ and $\frac{dD}{dH'}$. The uncertainty in hue prime ranges from $0.2° : 1.2°$.

$$U_{H'} = t\frac{\sigma_{cal}}{\sqrt{N_{I,cal} - 1}} \tag{2.9a}$$

$$U_D = \frac{dD}{dH'}U_{H'} \tag{2.9b}$$

$$B_\Theta = \sqrt{\left(\frac{U_D}{f}\right)^2 + \left(\frac{D}{f^2}U_f\right)^2} \tag{2.9c}$$

$$U_\Theta = \sqrt{B_\Theta^2 + P_\Theta^2}, \quad P_\Theta = t\frac{\sigma_\theta}{\sqrt{N_{I,exp}}} \tag{2.9d}$$

$$U_{\eta i} = \sqrt{\sum_{j=i}^{N}(D_{ij} \cdot U_{\Theta j})^2}, \quad U_\eta = \frac{U_n}{n_0} \tag{2.9e}$$

$$U_{Xhe} = \frac{U_n}{\frac{P}{RT}(M_{he}\kappa_{he} - M_{air}\kappa_{air})} \tag{2.9f}$$

Equation 2.9b propagates uncertainty from hue prime to transverse deflection distance, U_D. A central difference method is used to determine $\frac{dD}{dH'}$ for each pixel in the image. The local derivative corresponding to the pixels average deflection distance during the experiment is used for each pixel. Next, Eq. 2.9d calculates uncertainty in deflection angle by considering the bias uncertainty from the calibration curve and the lens focal length ($U_f = \pm 2.5\,\text{mm}$) and the precision uncertainty from the 5000 images acquired in the experiment. Propagation to refractive index is given by Eq. 2.9e. Note that the inversion causes uncertainty in the center to be the highest. Lastly, Eq. 2.9f gives the uncertainty in helium mole fraction. The results from the uncertainty analysis are shown later in Fig. 2.9.

2.6 Results

2.6.1 Raw RSD Image Analysis

Figure 2.4 shows instantaneous RSD images from multiple FOVs stitched together for the two test cases: Fig. 2.4a for $Re_0 = 800$ and Fig. 2.4b for $Re_0 = 2500$. The black dashed line in the images signifies the middle of each FOV. The yellow color (hue=π/3d) in the background, also observed in the center of the jet, corresponds to undeflected light rays, whereas deviations from the background hue indicate ray deflections by the test media. For example, red and green colors indicate large deflections caused by sharp density gradients in the shear layer of the jet flow. For both cases, the RSD images clearly show the laminar, transition, and fully turbulent regimes. Helium emerges as a laminar jet followed by an onset of turbulent structures in the shear layer leading to breakdown in both cases. The location of occurrence and associate structures are disparate. For $Re_0 = 800$, the jet flow is laminar for z = 0d to 10d and transitional for z = 10d to 13d. In contrast, for $Re_0 = 2500$, the laminar and transitions regions are much shorter, z = 0d to 1d and z = 1d to 2d, respectively. After transition, turbulence engulfs the jet at z = 13d for $Re_0 = 800$ and z = 2d for $Re_0 = 2500$. The RSD images also show stark differences in the sizes of the turbulent structures. The higher Reynolds number case contains much finer structures indicating a higher turbulent intensity. Another important

contrast illustrated in Fig. 2.4 is the diffusion of helium in the radial direction. At z=20d, the jet width is 6d for $Re_0 = 800$ and about 8d for $Re_0 = 2500$. In summary, the raw RSD images are a useful tool to identify many distinct features of the jet.

The transition region for $Re_0 = 800$ is further analyzed Fig. 2.5, showing three different snapshots during the experiment. Figure. 2.5 illustrates that the transition region moves approximately 3.5d during the 20 seconds of data acquisition although the pressure regulated helium supplies a nominally constant flow rate (velocity). Next, the flow regimes are analyzed using the fast Fourier transform (FFT) of hue fluctuations during the experiment. Figure 2.6 shows the results of the FFT analysis for both cases.

The contour plots in Fig. 2.6 show the number of frequencies at each pixel location during the experiment. In the laminar region, the hue at a pixel is constant (with time), and thus, no frequencies are observed in the contour plot (blue color). Increases in the range of frequencies indicates the instabilities in the shear layer (green/yellow color). Once coherent structures overtake the jet, a large continuous range of frequencies, indicated by the red color, is observed. Thus, Fig. 2.6 provides a quantitative spatial map of laminar, transition, and turbulent regimes in the jet. In both the mixing layer outlines a wedge shaped potential core - an unmixed region of jet fluid - commonly observed in turbulent plane jets [1]. The wedge begins at the location where the jet starts to diverge. For $Re_0 = 800$, this process begins around z=10.5d and by z=12.5d the potential core is completely consumed. For $Re_0 = 2500$, the wedge begins at z=1d and end around z=1.5d. Figure 2.6b shows a reduction in hue fluctuations downstream, suggesting a dissipation of turbulent intensity.

2.6.2 Quantitative RSD Image Analysis

Figure 2.7 shows the contour plots of instantaneous and average deflection angle data for $Re_0 = 2500$. The instantaneous contour shown in Fig. 2.7a displays larger deflection angles magnitudes than its average counterpart in Fig. 2.7b. Local eddies create large density gradients leading to local regions of large deflections. Very near the injector high density gradient eddies lead to very high deflections deflecting outside the filter range. Figure 2.7b reveals the small eddies of opposite magnitude occur in close proximity, e.g.,

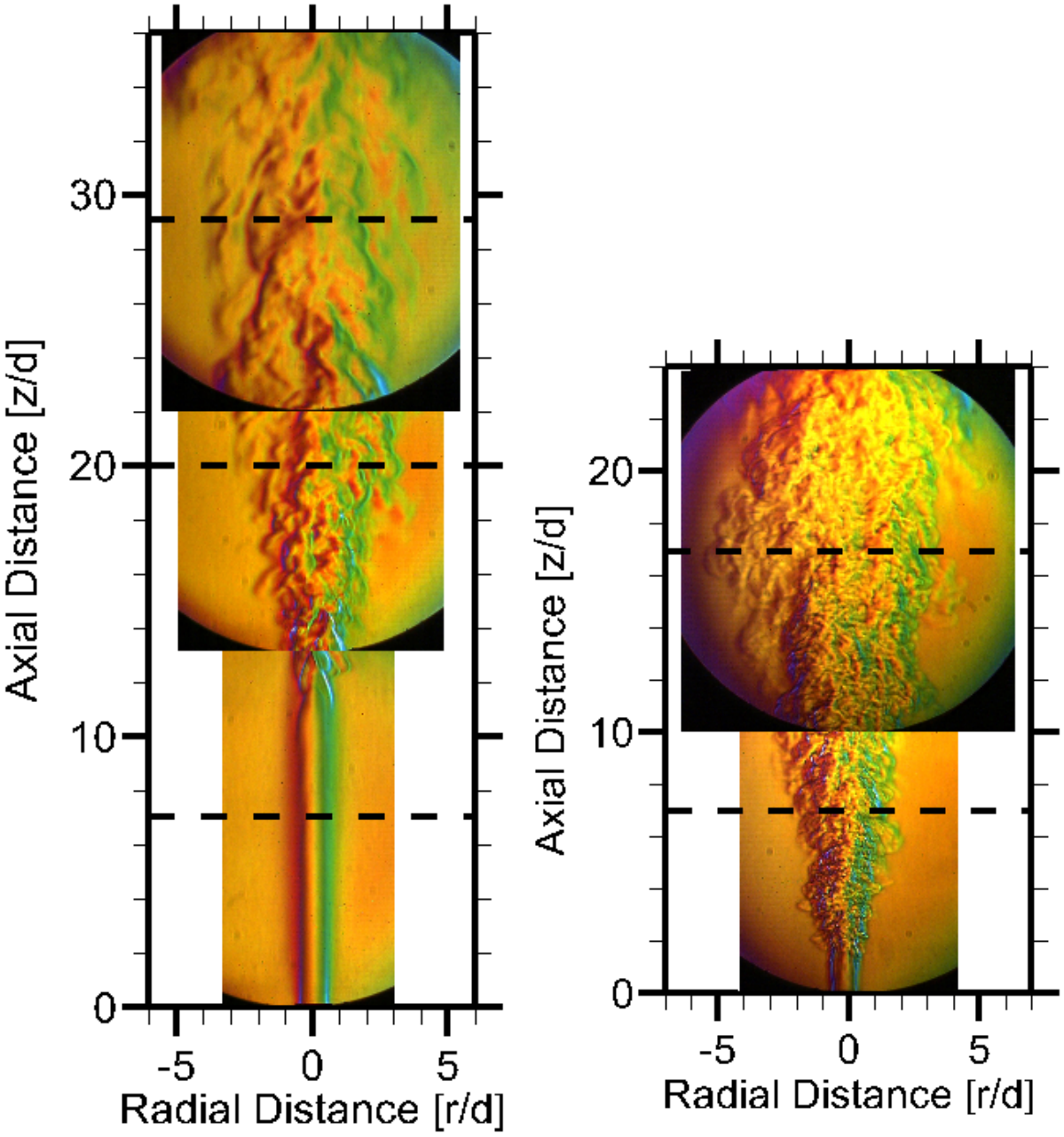

(a) (b)

Figure 2.4: Combined instantaneous RSD images are shown for (a) $Re_0 = 800$ and (b) $Re_0 = 2500$. The black dashed line represents the middle of each FOV.

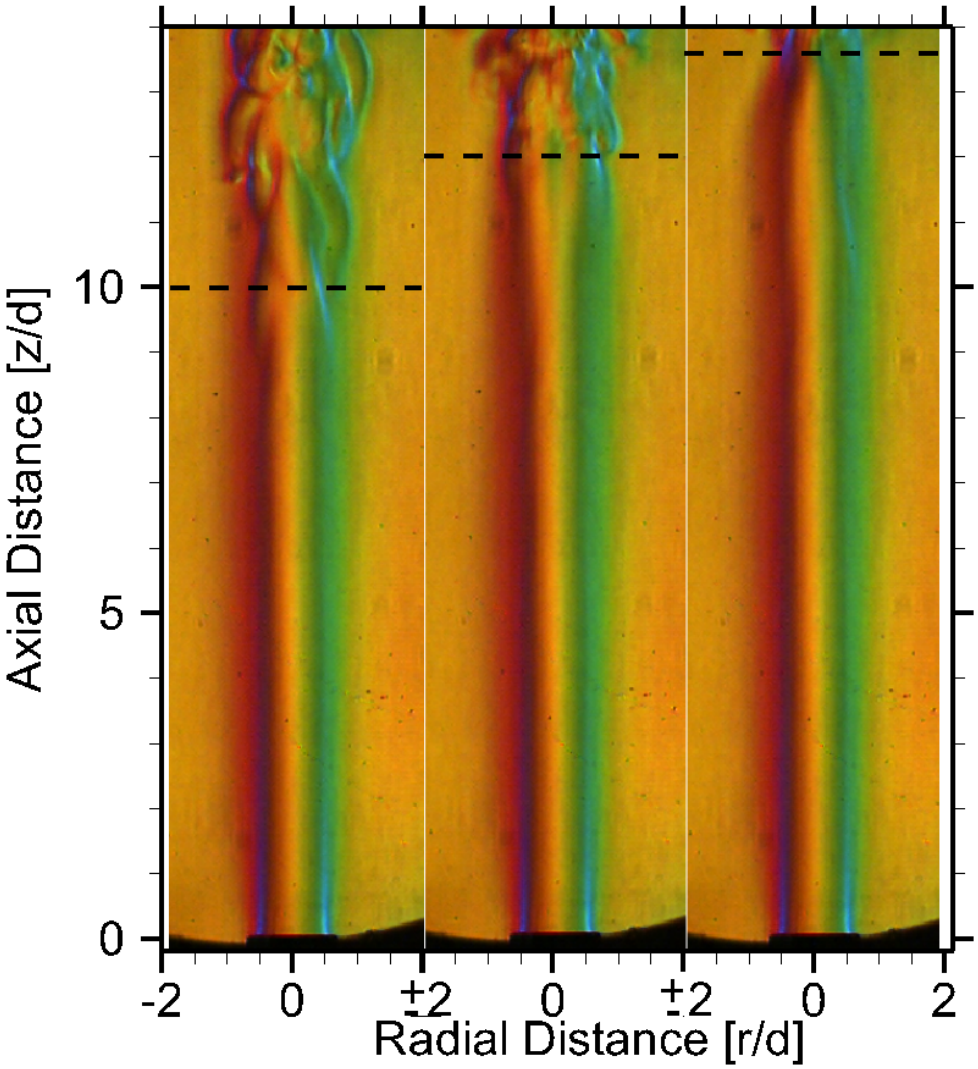

Figure 2.5: Transition region shown for three different snapshots for $Re_0 = 800$.

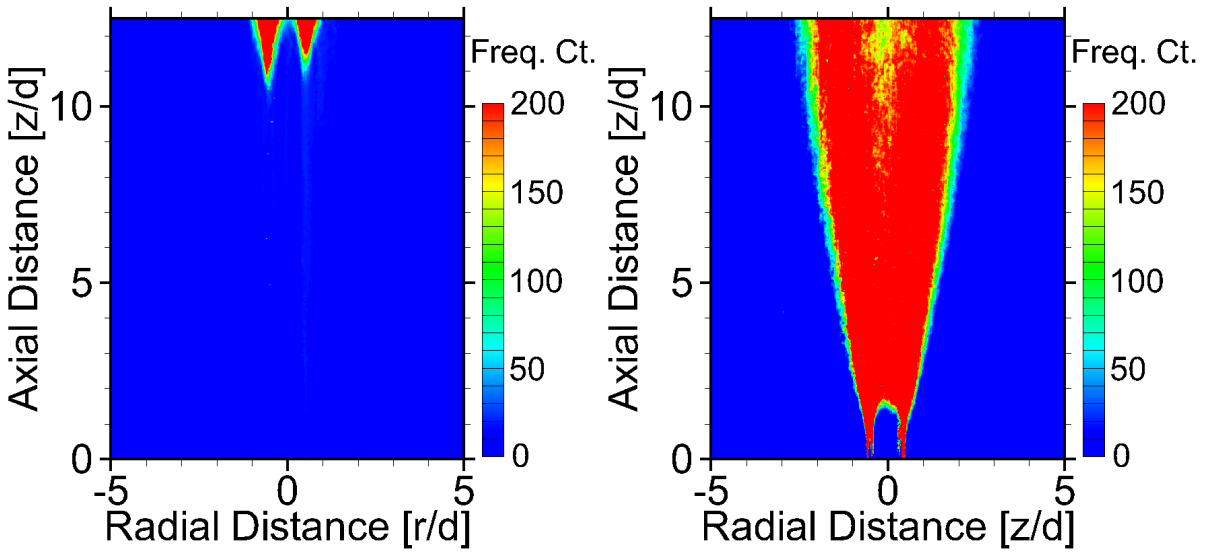

(a) (b)

Figure 2.6: The frequency count of hue fluctuation via FFT analysis is shown for (a) $Re = 800$ and (b) $Re = 2500$.

at Z=15 mm and R=-2.5 mm. Note that the smallest dissipative structures for this case are approximately 200 µm given by Eq. 2.10. [15].

$$\lambda_D = \Lambda \delta Re_\delta^{-3/4} Sc^{-1/2} \tag{2.10}$$

Here, Λ, $Re_\delta = u_c\delta/\nu_\infty$, and Sc are a mixing layer thickness constant, the outer-scale Reynolds number, and Schmidt number (0.2) respectively. The mean jet centerline velocity (u_c) and the full width of the mean axial velocity profile at 5% (δ) are estimated using the scalings given for pure jets in Chen and Rodi [22] and provided in Eq. 2.11.

$$u_c = 6.2u_0 \frac{\rho_0}{\rho_\infty}\frac{d}{x}, \qquad \delta = 0.36x \tag{2.11}$$

Buch and Dahm [15] found the mixing layer thickness constant to vary between 5.6 and 16.8 with a mean of 11.2 (used in this study). Thus, the Nyquist criterion is satisfied and the smallest dissipative eddies in the instantaneous images are spatially resolved. Figure 2.7b illustrates that symmetry develops after the averaging process.

Figure 2.8 plots the average deflection angle versus number of images for both cases

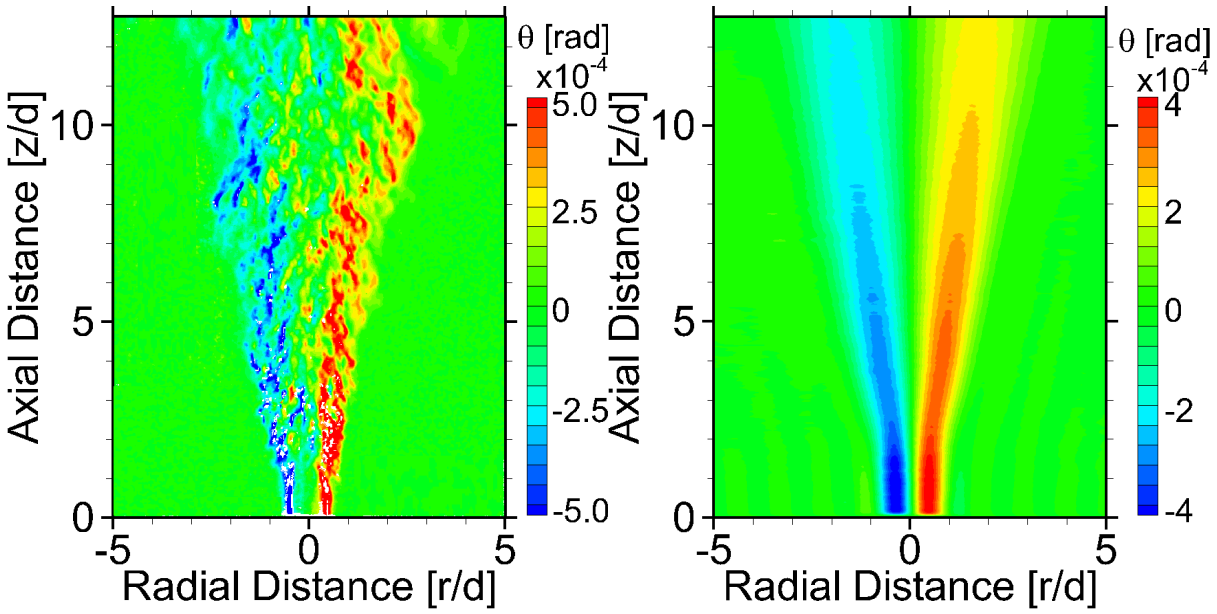

(a) (b)

Figure 2.7: An instantaneous (a) and average (b) deflection angle contours for $Re_0 = 2500$.

to establish statistically stationary flow, necessary to apply Eqs. 2.4. The $Re_0 = 800$ and $Re_0 = 2500$ cases show the negative (left side of the jet) and positive (right side of the jet) converged deflections, respectively. Plots are shown at multiple radial locations, center (green line), inner shear layer (blue line), middle of the shear layer (orange line), outer shear layer (red line), and the farfield (black line), at z=20d for $Re_0 = 800$ and z=5d for $Re_0 = 2500$. Figure 2.8 highlights that major fluctuations ($\pm 1 * 10^-5$) average out at about 1000 images for both cases, while the minor fluctuations ($\pm 4 * 10^-6$) exists until 3000 images for $Re_0 = 800$ and 4000 images for $Re_0 = 2500$.

Figure 2.9a shows the deflection angle profile and uncertainty at each location at z=20d for $Re_0 = 800$. The profile exhibits excellent symmetry, with minor asymmetries likely caused by slight jet tube misalignment and/or ambient flow field circulation. Minor asymmetries are reduced by a low pass FFT filter (green dashed line). The uncertainty is lowest at the edges where variation is minimal and highest in the shear layer around R=10 mm. Figure 2.9a shows the corresponding refractive index difference profile obtained using Eq. 2.5, independently for each side of the jet. Thus, any asymmetry will manifests itself by a discontinuity at the center. Figure 2.9a demonstrates symmetric

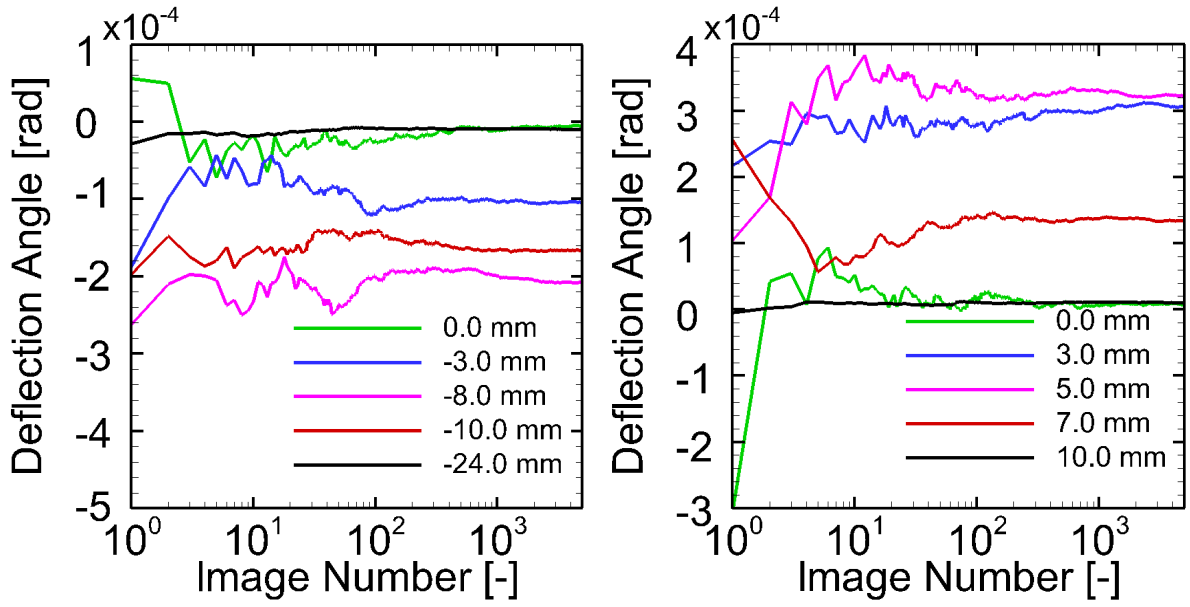

(a) (b)

Figure 2.8: Average deflection angle as a function of the number of images is shown for (a) $Re_0 = 800$ and (b) $Re_0 = 2500$. The five different radial locations are at z=20 d for $Re_0 = 800$ and z=5 d for $Re_0 = 2500$.

profile of refractive index difference on each side, and only a minor discontinuity at the center. The slight asymmetry can be mitigated by mirroring and averaging the two refractive index difference profiles.

Figure 2.9b shows the final result, i.e., the helium mole fraction obtained via Fig. 2.2. The helium mole fraction at the center is 0.54 and it reaches a value of zero at approximately r=20 mm. Figures 2.9a,2.9b show that the uncertainty in both normalized refractive difference and mole fraction is highest at the center. In this study, an uncertainty of less than 1% full scale of hue propagates to an uncertainty of about 3.5% full scale of helium mole fraction. Figure 2.9b also shows the helium mole fraction profiles for ±10% higher and lower helium flow rates than the nominal flow rate. Results show that the RSD uncertainties are far less than those resulting from ±10% change in the flow velocity at the inlet.

2.6.3 Validation with Published Data

Figure 2.10 compares the radial profiles of mean helium mole fraction at z=5d and 15d obtained by RSD and Rayleigh scattering measurements performed in Ref. [107] for $Re_0 = 2500$. In Fig. 2.10, the mole fraction is normalized by the mole fraction at the center (X_c)

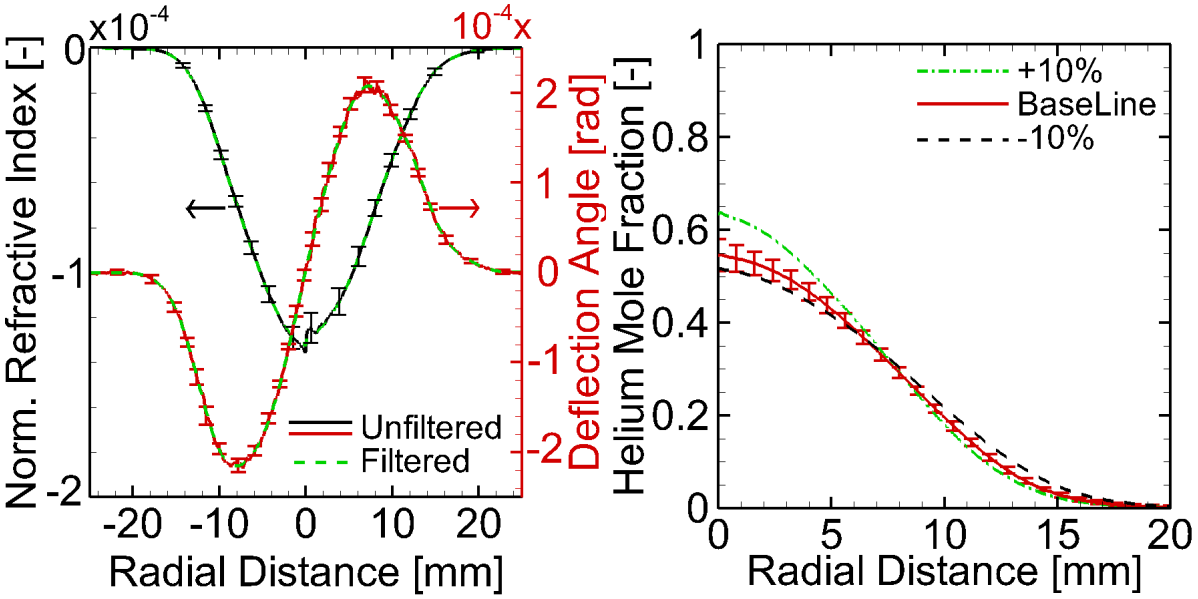

(a) (b)

Figure 2.9: (a) The deflection angle profile is shown along with the refractive index profile at z=20d for $Re = 800$. The unfiltered and filtered line are shown as the green-dashed and solid-red line, respectively. (b) The mole fraction profile is plotted along with the effect of velocity ($\pm 10\%$) on the mixing profiles at z=20d for $Re_0 = 800$. Uncertainty is shown as error bars for deflection angle, normalized refractive index, and mole fraction

and the radial distance is normalized by the jet full width at half maximum concentration ($\delta_{0.5}$). This normalization scheme provides self-similarity for the concentration field in momentum dominated ($z_{Fr} < 1$) turbulent free jets [97]. In the present case, $z_{Fr} < 0.27$ at both axial locations. Comparing jets that follow self-similarity using this normalization scheme flushes out experimental discrepancies in the inlet boundary conditions, e.g., slight different velocity, nozzle wall thickness, etc., to provide a valid comparison. Figure 2.10a shows excellent match within experimental uncertainty, demonstrating the validity of RSD to provide accurate concentration measurements in a turbulent flow field. The self-similarity observed in Fig. 2.10a shows that variations in the initial conditions, due to minor experimental differences, do not affect the results. Helium mole fraction profiles in Fig. 2.10b show a slightly higher value at the center at z=5d and only minor discrepancies at z=15d, likely caused by the minor differences in the initial jet velocity, tube thickness, minor co-flow, etc.

The normalizing parameters,$\delta_{0.5}$ and X_c, across the full-field provides further insight into the jet behavior. These parameters reveal if self-similarity is satisfied by checking the

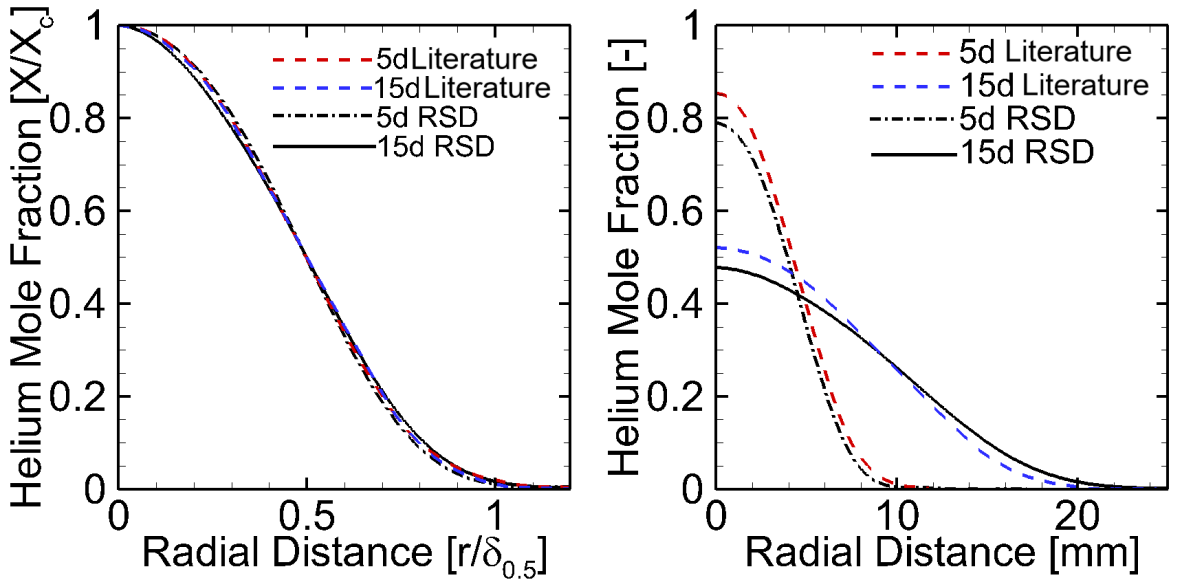

(a) (b)

Figure 2.10: (a) Non-dimensionalized and (b) absolute helium mole fraction helium mole fraction are presented (black lines) and compared with Ref. [107] (colored lines) for $Re_0 = 2500$.

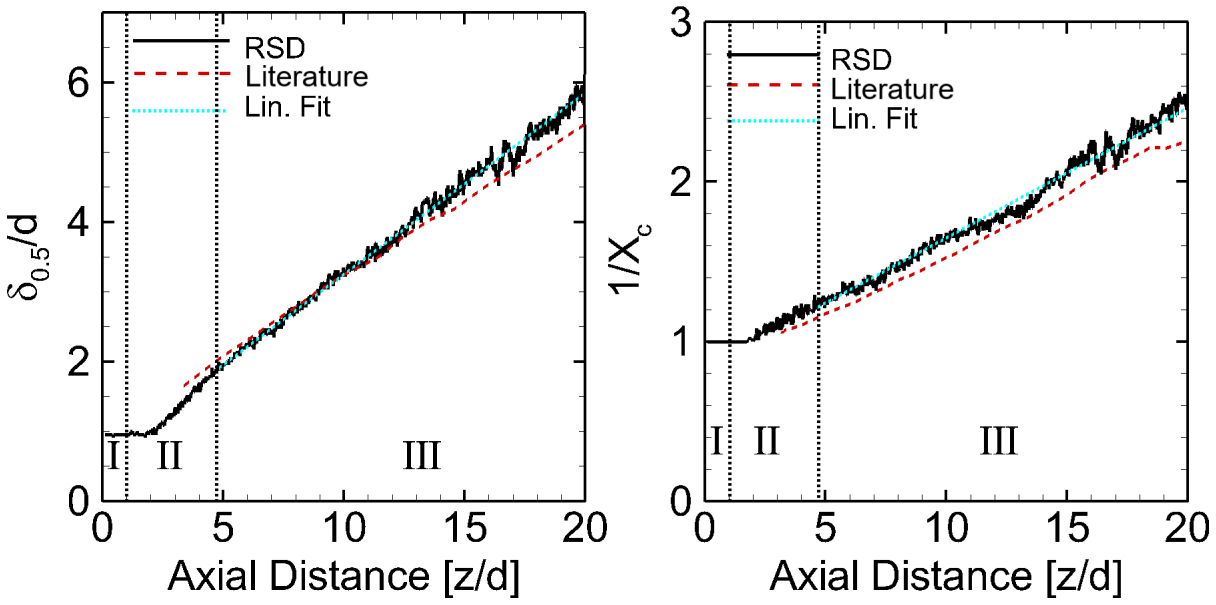

(a) (b)

Figure 2.11: The (a) full width at half maximum and (b) centerline mole fraction profiles are shown for $Re_0 = 2500$ and compared with Ref. [107].

two main assumptions: 1) the constant entrainment hypothesis and 2) centerline decay is inversely proportional to z [40]. Furthermore, the two parameters show the effect of experimental differences on the jet, e.g., occurrence of jet transition. Both $\delta_{0.5}$ and X_c give context to the radial comparison plots previously shown. Figure 2.11 illustrates the behavior for $\delta_{0.5}$ and X_c for $Re_0 = 2500$. Three different momentum dominated regions ($z_{Fr} < 1$) are outlines in both plots. Region I indicates the laminar portion of the jet. Although the jet growth rate and centerline decay are constant until about z=2d,the potential core start to diminish at z=1d - demonstrating that Fig. 2.11 is not sufficient by itself to identify the end of the laminar region. Region II is the developing turbulent region, where instabilities set in to initiate turbulent mixing. This region shows a slight non-linear behavior in both jet spreading and centerline decay. Beyond z=4.75d, Region III shows a constant entrainment and centerline decay given by a linear fit (blue-dashed line) with an R^2 value of 0.994 and 0.987 for $\delta_{0.5}/d$ and X_c, respectively. The high degree of linearity shows that self-similarity is achieved in Region III, which would also explain the excellent agreement reached between the profiles in Fig. 2.10a. A linear spreading rate is observed for data from both studies in Region III (Fig. 2.11a), where the slope from RSD is slightly greater than Ref. [107]. Kwon and Seo [57] showed that an increase in Reynolds number decreases the jet spreading rate for Reynolds number greater than 1300. Thus, it is likely that the jet inlet velocity in Ref. [107] was slightly higher, owning to the uncertainties in the flow measurements.

Next, the normalized and absolute profiles for $Re_0 = 800$ obtained by RSD and Rayleigh scattering [107] are compared in Fig. 2.12 at z=9d, 20d, and 30d. In this study, z=9d is within the laminar region, and hence, the RSD profile does not follow similarity in Fig. 2.12a. Conversely, in Ref. [107], the z=9d profile straddles in the transition region, and therefore, shows a centerline mole fraction of less than 1. In spite of these difference, caused by un-quantified minor variations in the inlet conditions, the two profiles agree with each other for R¿3 mm including at the edge of the jet ($R \approx 5$) with sharp gradients. At z=20d, the jet approaches self-similar behavior in Fig. 2.12a and mostly agrees except at the outer radial positions indicating that the 20d location is

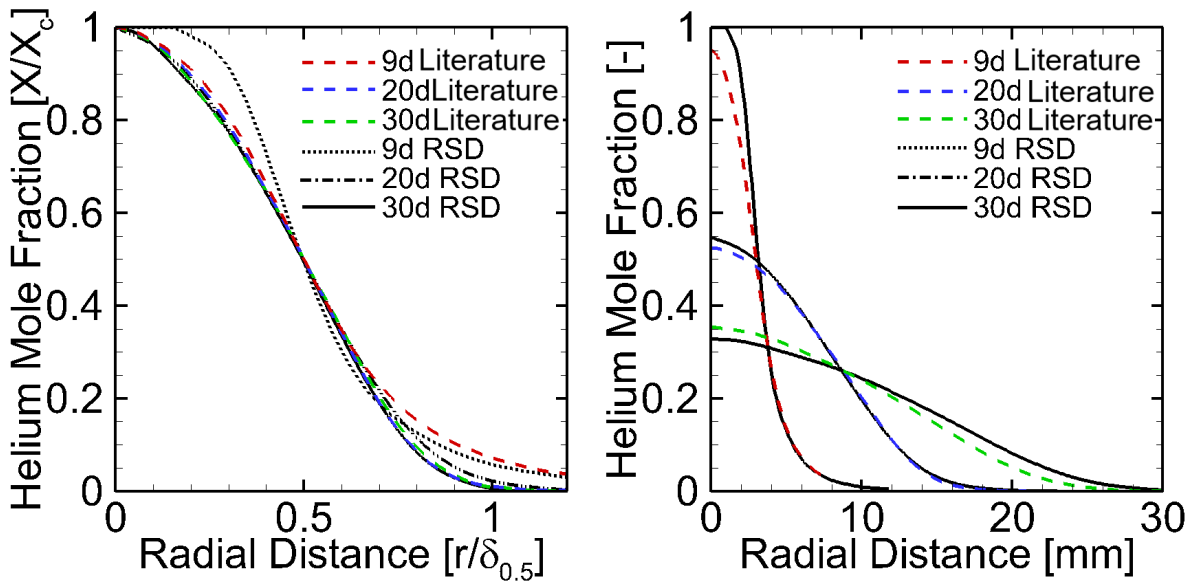

(a) (b)

Figure 2.12: Mole fraction results are presented for Rayleigh scattering in Ref. [107] (colored lines) and RSD (black lines) for $Re_0 = 800$. Both (a) non-dimensionalized and (b) absolute helium mole fraction are shown.

still slightly influenced by initial conditions either because the jet is not fully turbulent or because of the minor buoyancy effects ($z_{Fr} = 0.82$). The agreement at z=30d is much better indicating negligible influence of experimental discrepancies at this downstream location.

Figure 2.13 compares $\delta_{0.5}$ and X_c from RSD and Ref. [107] for $Re_0 = 800$. Region I is the laminar region until z=10.25d (also found in Fig. 2.6a). Region II is the developing turbulent regime until approximately z=16.2d. Region III is momentum-dominated regime given by a linear fit with an R^2 of 0.990 and 0.983 for $\delta_{0.5}$ and X_c, respectively, from z=16.2d to z=25d. Lastly, Region IV is governed by combined buoyancy-momentum effects starting at z=25d, where $z_{Fr} = 1$. Profiles in 2.13 agree in Region I although Ref. [107] shows an earlier transition. Region III shows similar centerline values but slightly different jet spreading rates. Region IV shows similar slopes in both spreading rate and centerline decay indicating negligible effects of initial experimental conditions at these downstream locations. In both cases, RSD shows full-field spatially resolved data beginning near the tube exit (z¿0.1d) to either z=20d ($Re_0 = 2500$) pr z=32d ($Re_0 = 800$)

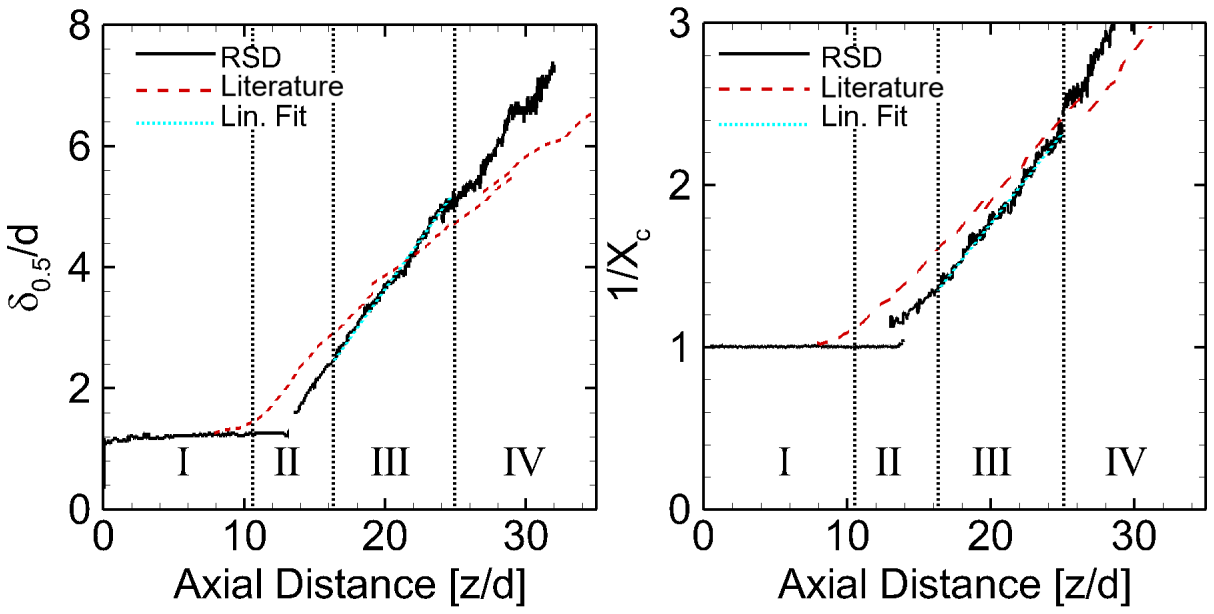

(a) (b)

Figure 2.13: The (a) full width at half maximum and (b) centerline mole fraction profiles are shown for $Re_0 = 800$ and compared with Ref. [107].

2.6.4 Full Field Measurements

The RSD technique is extended to quantify the mean mole fraction across the whole field by stitching together multiple FOVs for both test cases. For $Re_0 = 800$, the jet undergoes slight spreading near the exit, but the concentration remains nominally constant until about z=12.5d where the jet width increases suddenly in the transition region. For $Re_0 = 2500$, Fig. 2.14b shows that the jet spreads at z=1.5d, and further downstream the two FOVs match seamlessly.

Next, radial profiles of helium mole fraction are presented at various flow regimes as useful validation data for computation models. Also, the profiles help gain insight into the physical mechanisms of the jet. Five locations for each test case are shown in Fig. 2.15: tube exit, the transition region with an intact potential core, post transition region without potential core, a downstream turbulent location, and at the end of the FOV. In the near field and around the transition region, self-similarity does not hold. Both cases show broadening in the width and diminishing mole fraction at the center. In the transition region, large changes occur in the overall shape of the profile in a relatively small axial distance. Higher Reynolds number amplifies this effect whereby

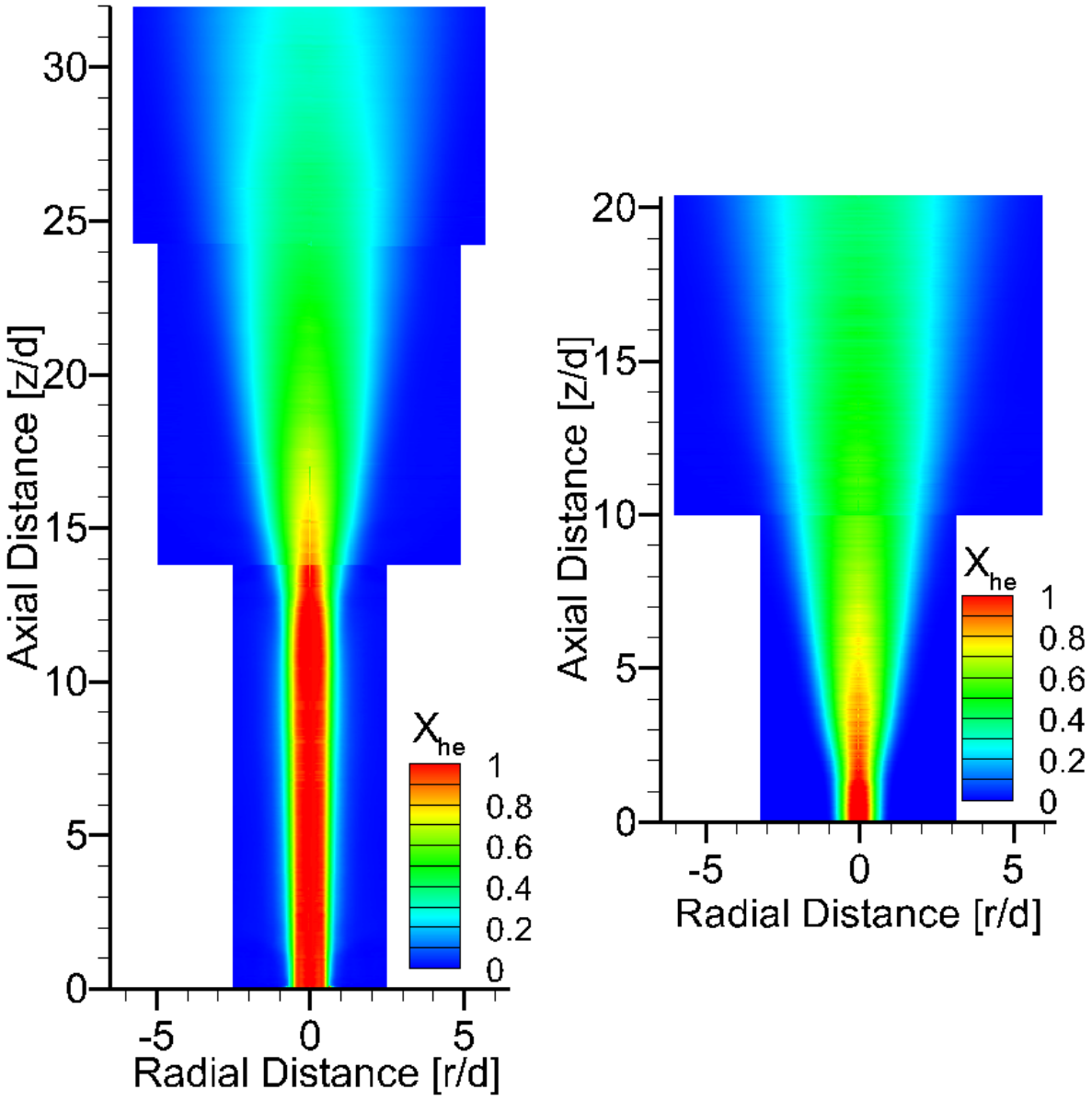

(a) $Re_0 = 800$ (b) $Re_0 = 2500$

Figure 2.14: Full field helium mole fraction for the case of $Re_0 = 800$ (left) and $Re_0 = 2500$ (right)

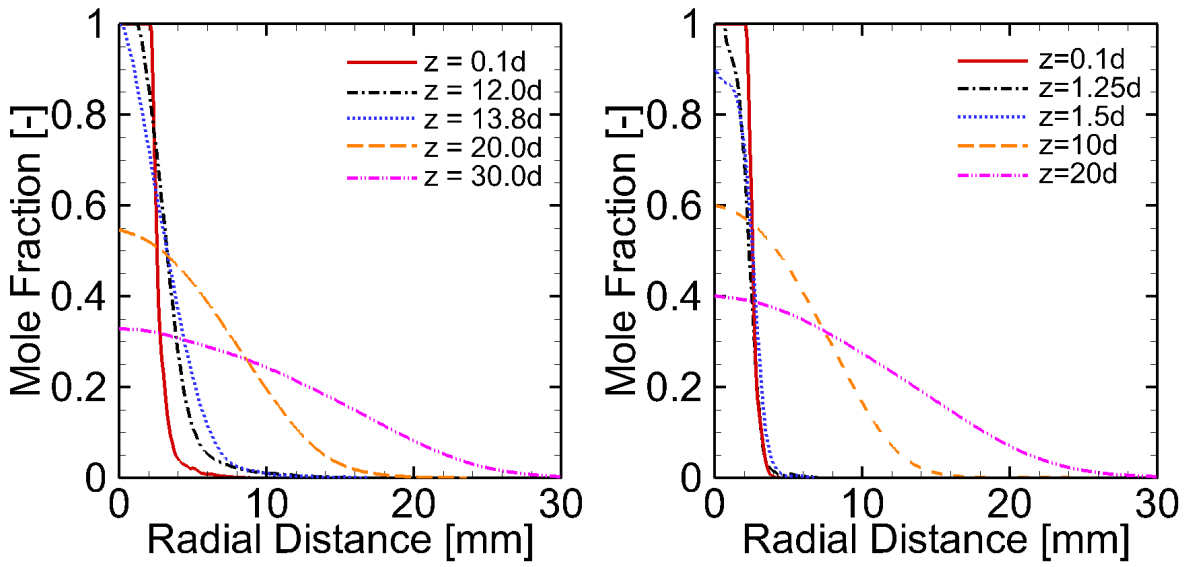

(a) $Re = 800$ (b) $Re = 2500$

Figure 2.15: (Left) Radial profiles for $Re = 800$. (Right) Radial profiles for $Re = 2500$.

the jet evolves from a potential core with a radius about 0.75 mm to the centerline mole fraction value of 0.9 in just 0.5d. One effect present in the $Re_0 = 2500$ that is not present in $Re_0 = 800$ is the inflection at the two transitional profiles. This peculiar behavior is postulated to be occurring from a Strouhal effect enhancing the mixing. It has been observed in Mastorakos *et al.* that forcing at Strouhal numbers around 0.6 enhances the mixing in the developing region of a momentum driven jet and this enhancement increased with increasing amplitude of excitation [69]. Figure 2.6b clearly shows self excitation frequencies present in the near field prior to turbulent mixing. Further investigation of the Strouhal effect on transitional mixing will be the focus of future work. Post transition ,i.e.,20d and 30d for $Re_0 = 800$ and 10d and 20d for $Re_0 = 2500$, the behavior shows the same qualitative shape as observed previously.

2.6.5 Hardware Averaging

The deflection angle required for the analysis can be averaged either in software or in hardware. The former converts the instantaneous hue to the instantaneous deflection angle, and then, the average is obtained in post-processing, as in the methodology described above. However, in hardware averaging, the camera sensor itself averages the RGB signal to obtain the average hue, and thus, the average deflection angle. If all the intermediate

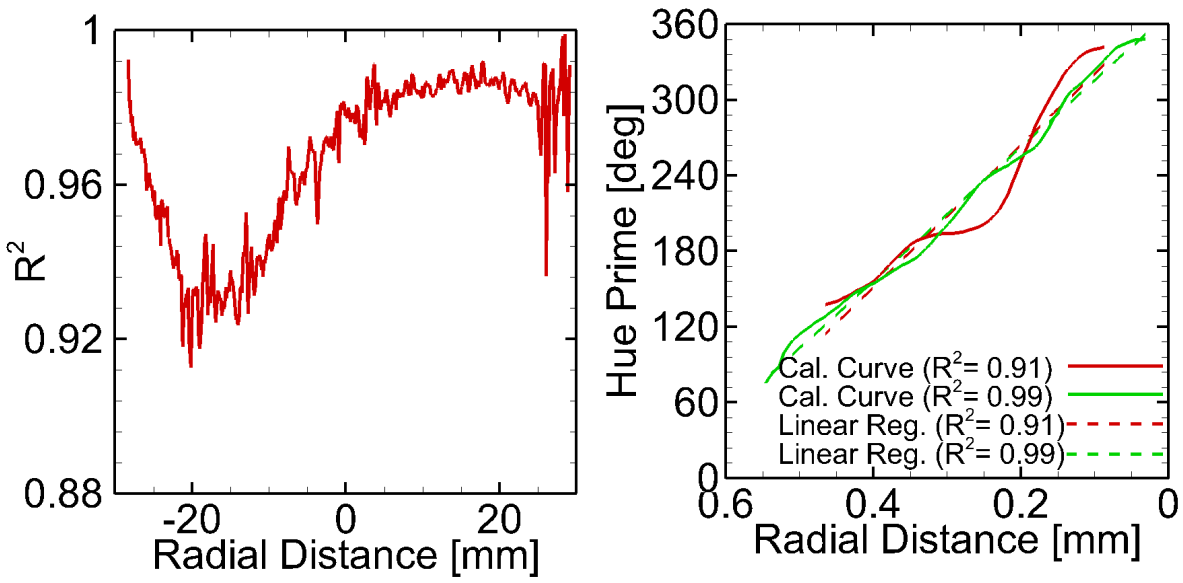

(a) R^2 (b) Calibration

Figure 2.16: (Left) R^2 plotted versus axial distance for the location of 20d downstream. (Right) Two calibration curves are shown: a linear (solid green) and a non-linear (solid red) and their respective linear regression lines (dashed).

steps are linear relations then hardware averaging is no different than software averaging. Since RGB to HSV conversion, and H to H' conversion are linear relations, the filter calibration process is the only potential source of non-linearity. To further explore this concept, a filter with non-linear calibration on one side and a linear calibration on the other side was designed and used with long exposure experiments. Figure 2.16b shows filter calibration curves at R=-20 mm (red line) and R=2.5 mm (green line) and their respective least squared fits (dashed). Figure 2.16a shows non-linear behavior dipping to an R^2 of about 0.91 between R=-14:-22 mm and reaching a R^2 value around 0.98 for the positive side ($R > 0$) of the image. Thus, left side of the filter is non-linear and the right-side of the filter is linear. The optical setup is slightly modified for the long exposure experiments. A neutral density filter is attached to the aperture to reduce the light throughput. The camera's exposure time is changed to 250 ms for hardware averaging. Longer exposure time causes ambient light to affect the signal.

The RSD image in Fig. 2.17a, acquired between z=13d-26d shows that the turbulent features are smoothed out. One hundred images were acquired and averaged to obtain a converged symmetric image used to obtain average deflection angle, average refractive

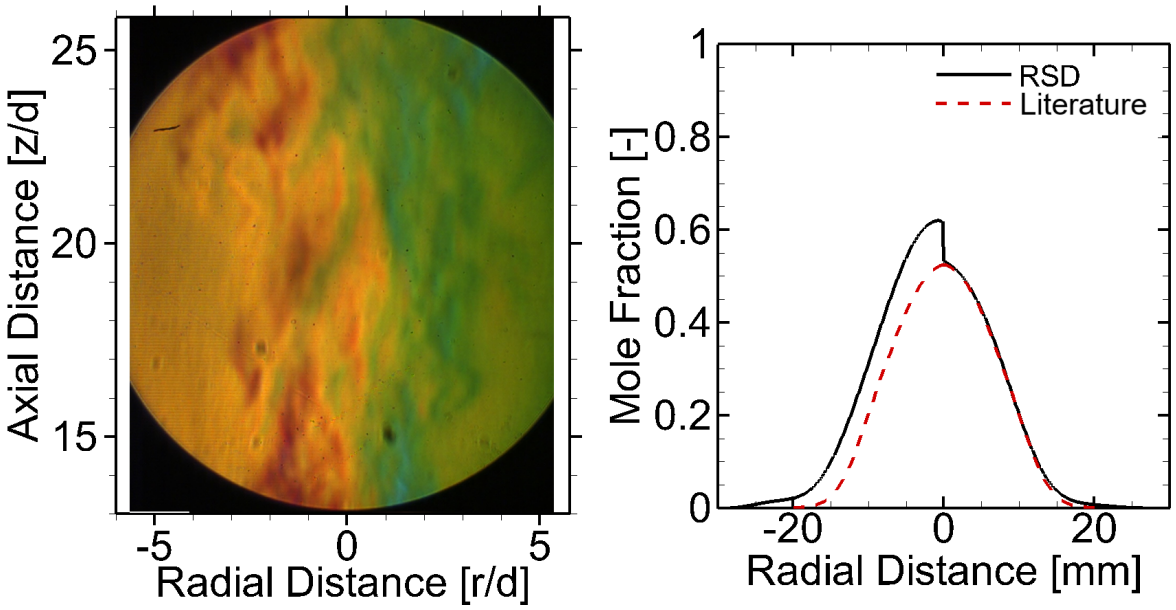

(a) (b)

Figure 2.17: (a) Long exposure raw image for the case of $Re_0 = 800$ with (b) the results for mole fraction compared with Ref. [107].

index difference, and finally, average helium mole fraction. Figure 2.17b shows that the linear side of the filter (right side) provides accurate results, but the results obtained with the non-linear side are highly erroneous. The results in Fig. 2.17b demonstrate that hardware averaging can be used only if the filter is linear, i.e., $R^2 \approx 0.98$. Hardware averaging can be valuable in applications where either the light source or the data size is limited.

2.7 Conclusions

In this study, RSD was implemented and validated for the first time in a turbulent environment to provide quantitative mixing measurements. Several important considerations are necessary for accurate RSD turbulent measurements. First, a pixel-to-pixel calibration process with multiple images acquired at each calibration step is strongly recommended. If these steps are not incorporated uncertainty is significantly increased. Second, eliminating regions of the filter with high absorptivity by utilizing an alternative hue spaces can improve the ability to acquire data at lower exposure times. Thirdly, providing average normalized refractive index requires the fluctuating components in de-

flection angle to approach zero. A large enough dataset (>1000 images) drives the process to a statistically stationary state. Lastly, the instantaneous optical-to-thermodynamic relationships can be used to compute average parameters as long as the process between refractive index and the thermodynamic property is linear. The effect of exposure time on the quantitative measurements was also investigated. It was determined that long exposure hardware averaging provides the same results as short exposure experiments with the caveat the the filter is linear. A linearity of $R^2 \approx 0.98$ is required for accurate results. Otherwise, the non-linearity of the filter skews the hue data and results in spurious measurements.

RSD was also used to provide measurements in other regimes of the jet such as the laminar and transitional region. Analysis of the transitional region revealed that transition on average spans a range of axial distances that decreases with increasing Reynolds number. A higher momentum provides a stabilising effect which narrows the band of transitional distances. Also, radial profiles reveal that significant changes occur in the mixing profiles, both in shape and magnitude, over a relatively small distance. Using RSD to provide full field measurements at the nozzle exit to far downstream in a transitioning turbulent jet gives insight to how mixing develops and propagates and provides useful validation data for computational models in regions where self-similarity may not be satisfied. The present study demonstrates the capability to provide full-field mixing measurements in a transitioning turbulent jet.

CHAPTER 3
PHASE BOUNDARY DETECTION IN TRANSIENT, EVAPORATING HIGH-PRESSURE FUEL SPRAYS BY RAINBOW SCHLIEREN DEFLECTOMETRY

3.1 Abstract

Rainbow Schlieren Deflectometry (RSD) technique is used to simultaneously identify the liquid and vapor boundaries during transient evolution of evaporating high-pressure fuel sprays. Traditionally, liquid and vapor phases require separate diagnostics, whereas this work relies upon a single technique to identify each phase, in addition to the previously demonstrated capability of RSD to measure local fuel-air mixing in the vapor zone. The proposed RSD methodology is a significant improvement over a previously published technique, i.e., it is applicable to the transient period and much less data and hence, computational effort, is required. Experiments are conducted in a constant pressure flow rig (CPFR) for multiple fuels and test conditions to demonstrate the capability of the proposed RSD diagnostic. For each test condition, multiple injections are performed in quick succession to obtain statistically significant data sets to depict the spray evolution at a spatial resolution of 100 μm, camera framing rate up to 40 kHz, and exposure time down to 1 μs. The method and results are compared and discussed within the context of prior work using RSD, Mie-scattering, and Siebers' liquid length scaling law. The objective of this study will bring to fruition the possibility of RSD to simultaneous quantify liquid existence and provide vapor zone mixing measurements.

3.2 Introduction

Non-intrusive optical diagnostics techniques for point or planar measurements are attractive because they do not disturb the flow. Often, such techniques are the only viable option to obtain experimental data for applications such as fuel-air mixing in diesel engines involving high pressures, high temperatures, reacting substances, fast time scales, complex flow fields, etc. Several optical diagnostic techniques utilized in diesel environments are outlined and summarized in the Engine Combustion Network database [89]. This well-documented internet library includes experimental techniques to measure diesel spray combustion properties such as liquid/vapor jet penetration, flame lift off length, ignition delay, soot, and quantifying fuel-air mixing and the ambient flow field.

In diesel fuel sprays, liquid length and vapor zone are important parameters affecting autoignition, combustion, emissions, etc. Mie scattering has historically been used to measure the liquid length or liquid portion of the fuel jet [3,104]. This method elastically scatters light from particles larger than the wavelength of incident light, which makes it ideal to detect the liquid droplets. Rayleigh scattering is another elastic scattering technique used to quantify fuel-air mixing in the vapor zone of the spray downstream of the liquid zone [41, 52, 91]. Rayleigh scattering is susceptible to interference from strong elastic scattering by liquid droplets, and it can only be used when the droplets are completely vaporized to avoid signal saturation. Traditional schlieren and shadowgraphy techniques have been utilized to locate the vapor boundary in vaporizing fuel jets [79, 84]. All of the above techniques apply exclusively to a specific region, and therefore multiple, and separate, diagnostics are required to probe the liquid and vapor portions of the spray. Such methods can either result in bulky and costly experimental setups, or require multiple experiments dedicated to each diagnostics. A diagnostics technique that can simultaneously resolve multi-phase regions of the fuel spray will therefore be highly desirable.

There are a few techniques in the literature for simultaneous phase diagnostics. Laser absorption scattering (LAS) has been proposed to simultaneously measure liquid droplet distributions and vapor mass fraction in the spray [23, 109, 123]. However, LAS requires

liquids (replacing the fuel) with specific optical properties that include strong absorption of ultraviolet light and negligible absorption of visible light at the chosen wavelengths. Laser-induced excited-state complex fluorescence has been used for qualitative liquid and vapor zone visualizations in fuel sprays [74]. Melton obtained spectrally separated fluorescence emissions from the liquid and vapor phases by adding exciplex-forming dopants to the fuel [73]. Bardsley *et al.* [11] applied this technique for spray diagnostics in an engine and demonstrated that accurate fuel concentration measurements above 500 K are possible only if the local gas temperature is known a priori [44].

Another more recent work by Westlye *et al.* applied diffuse back-illumination extinction imaging (DBIEI) for simultaneous liquid length and soot concentration measurements in diesel-like sprays. [120]. Westlye *et al.* developed the DBIEI technique to overcome light attenuation, caused by beam steering, in conventional schlieren and Mie scattering systems. They investigated several DBIEI setups along with a theoretical study to minimize the beam steering effects, and developed sizing requirements that can be applied to arbitrary experimental systems.

Previously, rainbow schlieren deflectometry (RSD) has been applied to measure the equivalence ratio in the vapor zone of diesel-like sprays [76]. Agrawal and Wanstall [5] provide a detailed review of the RSD technique and its applications to acquire quantitative measurements in jets and flames. Recently, Wanstall *et al.* [113] applied the RSD to simultaneously measure the liquid length as well as equivalence ratio distributions in the vapor zone. They demonstrated that the RSD signal contains two separate signals: (1) light intensity attenuated by light absorption, scattering, etc., to identify the liquid zone, and (2) light deflected by refractive index (or density) gradients in the media to quantify the vapor zone. The partitioned nature of the two signals (hue and intensity) distinguishes RSD from other diagnostics; eliminating the need for two different diagnostics to separate the liquid zone and quantify thermodynamic properties in the vapor zone. Note that the conventional schlieren systems do not offer this capability to acquire two signals to simultaneously analyze liquid and vapor zones. For this reason, RSD shows great potential for advanced spray diagnostics.

This study utilizes the ideas presented in Ref. [113] to develop a more robust technique to differentiate the liquid zone (single phase) from the spray boundary (two-phase), and to quantify liquid and vapor regions in the evolving transient jet. The algorithm presented in this study relies upon the statistically relevant data of the evolving spray from multiple injection experiments. The technique is then demonstrated by applying it to study sprays of two fuels at multiple test conditions.

3.3 Experimental Setup

3.3.1 Constant Pressure Flow Rig (CPFR)

Table 3.1: **Operating conditions and camera specifications for different test cases.**

Case	Fuel	Amb. Temp. (K)	Amb. Pres. (bar)	Fuel Pres. (bar)	Fuel Temp. (K)	Injection Dur. (ms)	Cam. FR (kHz)	Cam. Exp. Time (μs)
1	n-heptane	520	30	1000	333	4.5	40	1
2	n-heptane	800	30	1000	363	2.5	40	4
3	Propane	305	30	500	333	4.5	20	4

The experiments listed in Table 3.1 were conducted in a constant pressure flow rig (CPFR), shown in Fig. 3.1, with two parallel 100 mm diameter quartz windows to provide the optical access. The desired test conditions are obtained by a continuous supply of preheated, high-pressure air at 30 bar. Multiple fuel injection experiments can be performed in quick succession to acquire a statistically significant data set. Approximately five seconds is required between tests to confirm that the contents of the previous injection have been flushed out. The CPFR is vertically oriented with a counterflow arrangement between fuel and air. The pressure inside the rig is controlled by an upstream dome regulator in the air supply line, and the air flow rate is regulated by a control valve downstream of the CPFR. Electrically heated air enters the bottom of the rig through a stack of 5-micron metal mesh used to breakdown the large vortical structures. The air flow velocity (<0.5m/s) is at least three orders of magnitude smaller than the fuel jet velocity (>100 m/s). Hence, the airflow is effectively stagnant during fuel injection and does not influence the spray behavior. This has been verified for a similar system in a

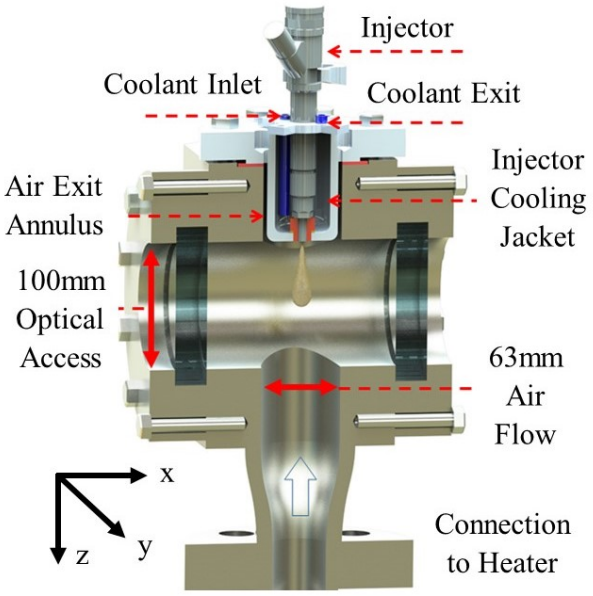

Figure 3.1: Constant pressure flow rig (CFPR) illustration.

previous work [111]. The air exits at the top of the rig through four, 3 mm diameter, circular holes placed symmetrically around the injector tip and cooling jacket.

The fuel is injected by a Bosch CRIN3-18 fuel injector modified to have a single 100 μm axial hole at the tip, directing fuel down the central axis of the rig as shown in Fig. 3.1. A pressure multiplying pump, capable of pressurizing fuel to 2000 bar, supplies the fuel to the injector. The injection pressure at the fuel inlet line is monitored by a pressure transducer to ensure that injection occurs within $\pm$ 5 bar of the desired injection pressure. Fuel is stored in a reservoir located upstream of the fuel pump. The fuel reservoir has been designed to include a pressurized line to maintain the liquid phase of fuels that would be gaseous at normal ambient conditions. Thus, unconventional fuels such as propane can be injected as liquid. The fuel injector is enclosed by a cooling jacket to indirectly control the fuel temperature by circulating coolant from an external reservoir. The injector body, and presumably the fuel, temperature is monitored by two thermocouples on either side of the coolant inlet and return line to the cooling jacket. These two temperature measurements are also used to control heat dissipation from the coolant through a heat exchanger with variable cooling fans. A thermocouple near the injector tip (visible in the instantaneous images shown in Fig. 3.5) is one of many monitoring the chamber temperature. Steady-state temperature conditions are reached in about three hours when the air temperature

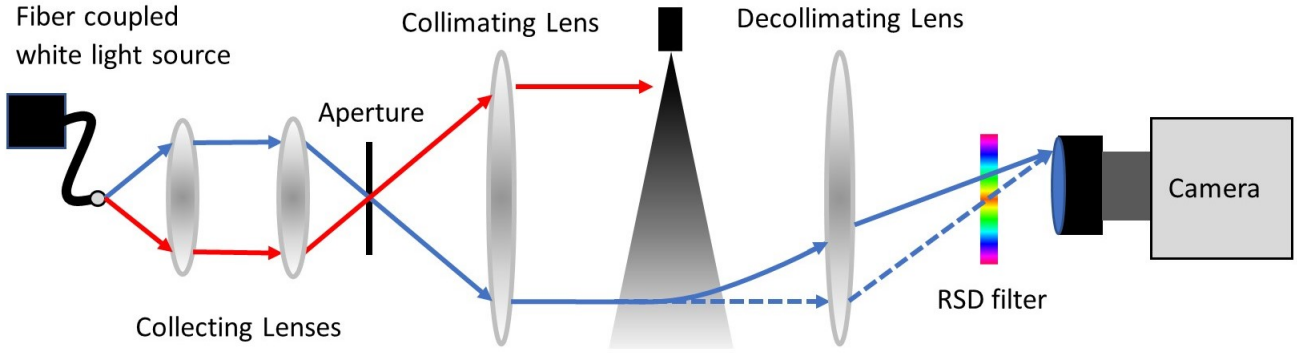

Figure 3.2: Schematic of the RSD system.

at the center of the rig and wall temperature are reasonably constant with time. As the chamber temperature stabilizes, the temperature gradient between the wall and the center of the chamber decreases. A maximum difference of 50 K is observed at a radius of approximately 30 mm when the chamber reaches the maximum operating temperature of 825 K.

Heptane and propane fuels are tested in this study. The chamber pressure for all tests is 30 bar; the maximum achievable pressure with the compressor system. Experiments for heptane and propane are performed at respective injection pressures of 1000 bar and 500 bar. The common fuel injection temperature for diesel-like fuels such as heptane is 90° C [89], but because 90°C is near the critical temperature for propane, the injector temperature set-point is reduced to 60°C. This set-point temperature is also used for one of the heptane cases to increase the liquid length and demonstrate greater contrast between the liquid and vapor zones. Table 3.1 lists conditions for all of the test cases. Case 1 is used as the baseline case to explain the data analysis procedures.

3.3.2 Rainbow Schlieren Deflecometry (RSD)

Figure 3.2 illustrates the RSD optical setup utilized in this study. A fiber coupled light source (Energetiq, EQ-99X) provides continuous broadband light through a 100 μm diameter fiber optic cable. A 50 mm diameter, 80 mm focal length collimating/decollimating achromatic lens pair is used to collect the diverging light from the fiber and refocus it onto a 100 μm rectangular source aperture. The aperture height is oriented parallel to the spray axis to enable the measurement of transverse density gradients. An-

other achromatic lens pair (75 mm diameter, 250 mm focal length) is employed for the schlieren optics. A 5 mm wide digitally printed symmetric rainbow filter - a transparent rectangular strip with fine color (hue) gradations - is placed at the focal point of the decollimating lens. This filter encodes the deflection at the filter plane as color (hue) in the camera image which can be related geometrically to the deflection angle of a ray by the test media. The print resolution of the color filter at 4.2 μm per color strip yields a continuous hue variation of the rays deflected by the test media. Filtered images are acquired by a Phantom v611 digital color camera at varied acquisition rates to meet the field of view requirements of each experiment.

Figure 3.2 illustrates a deflected light ray (solid blue line) focusing onto a different color strip on the filter plane compared to an undisturbed light ray path (dashed blue line). A light ray (red) fully attenuated by scattering, absorption, etc. from the liquid core or droplets in the spray is also shown. Light intensity of such rays reaching the image plane is reduced, resulting in dark regions in the image. Prior work focused on quantitative analysis of the vapor region and is not discussed in this study. As mentioned before, Ref. [113] provides a detailed overview of the theory, implementation, and applications of the RSD technique.

3.4 Data Analysis

The theory and analysis developed is this section stems from our previous work published in Ref. [113], where RSD was applied to determine the average liquid boundary during the quasi-steady period of the spray over 50 injections. The quasi-steady period is defined as the time period during injection in which the liquid has reached a quasi-steady maximum penetration length – although smaller fluctuations still exist [104]. The injection duration was such that approximately 40 image frames in each injection were considered quasi-steady and thus the results were an average of 2000 images; 50 injections with 40 quasi-steady frames each. Figure 3.3 shows the RSD liquid boundary determined in the manner described in Ref. [113] in red together with black dashed-dotted line representing liquid boundary determined by Mie scattering [113]. These boundary lines

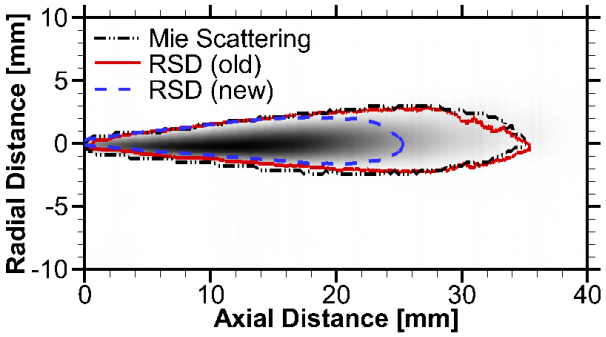

Figure 3.3: The average liquid boundary of 2000 images during the quasi-steady period of a fuel spray is calculated using the RSD algorithm from Ref. [113] (red) and Mie scattering (black dashed-dotted). The results are compared to the liquid zone (blue-dashed line) determined from current RSD methodology. The boundaries are overlaid on the time-averaged Mie-scattering image.

are overlaid on a color-inverted average Mie scattering image (gray shaded area). The ambient pressure and temperature in this study was P =13 bar and T =180° C, respectively, which was limited by the test chamber utilized. The new RSD methodology in the present study resulted in the liquid boundary shown by the blue dashed line. The difference between the two RSD methodologies and what they detect will be discussed later. Briefly, the significantly smaller liquid boundary by the new RSD method represents the boundary with liquid present 95% of the time. In contrast, the old RSD method (and Mie scattering) seems to detect the boundary where liquid in the form of a spray is present. The new RSD method qualitatively aligns with recent developments in the literature using DBIEI [120] as will be discussed later.

The present study generalizes the RSD liquid boundary detection method to include the transient fuel injection period. A two-dimensional color-coded histogram/contour map is provided to show statistical variations of the liquid boundary over numerous injections. Simultaneous transient measurements of liquid and vapor penetration zones are obtained while dramatically improving the computational speed by an order of magnitude compared to that of the previous work.

Color images acquired by a camera are typically digitized in terms of red, green, and blue (RGB) intensity values. The RGB color space is based on Cartesian coordinate system, where each axis is either red, green, or blue. Two complications arise when representing color in the RGB space. First, three independent values are needed to

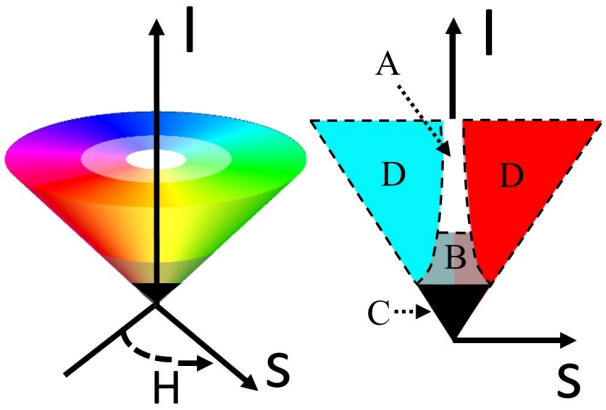

Figure 3.4: (Left) The HSI color space represented as a cone. (Right) A center plane slice from the HSI cone along the hue angle of 0° and 180 ° is shown. Regions A and B represent very low saturation with little and moderate attenuation occurring, respectively. Region C corresponds to significant attenuation, while D represents the area of reliable hue measurements.

quantify color which has encoded the transverse displacement of a ray at the filter plane. Secondly, the RGB coordinates are not unique for a given color (or hue). Thus, the RGB space is mapped to the hue, saturation, and intensity (HSI) space [50]. The HSI color space is embodied in the polar coordinate system; the polar angle describes the color or hue as demonstrated in Fig. 3.4. The radius indicates saturation or the relative "grayness" in the image, e.g., saturation is 0.0 for gray-scale image and 1.0 for full color image. For saturation of 1.0, one of the RGB values must be zero, and saturation is 0.0 if the three RGB values are the same. Intensity is the normalized axial coordinate, with 0.0 and 1.0 signifying complete and no attenuation respectively. Light intensity can be attenuated by scattering, absorption, etc. by the test media. In RSD, the intensity measurement is nearly equivalent to that of shadowgraphy. Further details about the conversion from the RGB space to the HSI space are found in Ref. [50].

Figure 3.5 shows an instantaneous RSD image in (a) RGB, and corresponding (b) hue, (c) saturation, and (d) intensity images for liquid n-heptane injected into ambient air at 518 K and 30 bar and at 3.05 ms after start of injection (aSOI). The fuel injector tip and thermocouple are visible on the left edge and top left quadrant, respectively. The RGB image has been enhanced by increasing saturation and gain to make it more visually appealing. However, the hue, saturation, and intensity images are unaltered.

Intensity in the HSI color space is the average of the intensities at red, blue, and green

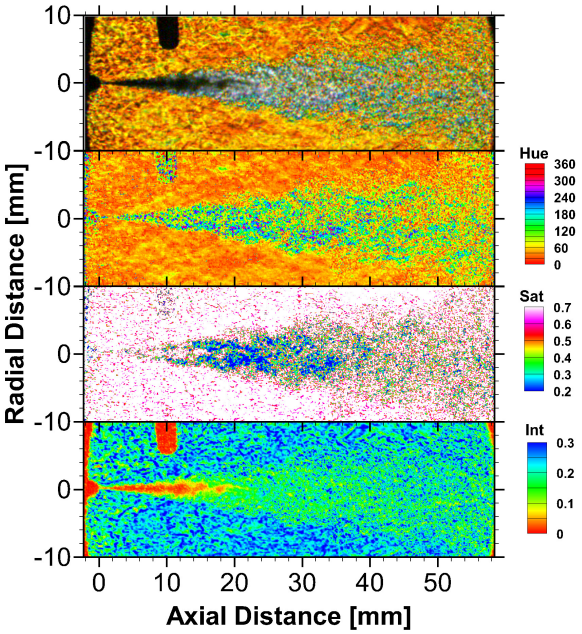

Figure 3.5: (Top) An RGB snapshot of n-heptane at 245 C and 30 bar at 3.05ms aSOI. The corresponding hue (middle-top), saturation (middle-bottom) and intensity (bottom) images after converting from RGB to HSI.

channels. Thus, RGB values below the noise threshold of the camera can result in low intensity values in the HSI color space. In this case, camera noise can cause dramatic hue variations (or poor signal to noise ratio) thereby affecting hue quantification. Experience has demonstrated that hue measurements are imprecise for intensity values below <10% as illustrated in Fig. 3.4. For example, the dark regions in the RGB image such as the thermocouple, injector tip, and even the dense parts of the spray result in meaningless hue values. These dark regions in the RGB image are represented as red regions in the intensity image. As discussed earlier, the red regions in the intensity image are attributed to light scattering and absorption from the liquid region. The intensity image reveals contrast between the liquid and vapor regions in the jet; note that the camera must be focused at the center of the spray to correctly map these zones.

The algorithm developed in Ref. [113] is modified and greatly simplified here, however, the underlying principle remains the same - regions of the spray with liquid are much darker than the rest of the spray. The methodology in this work is composed of two main steps: 1) compile intensity values for all injections at each time step and pixel location based on the RGB to HSI conversion, and 2) determine a threshold (reference)

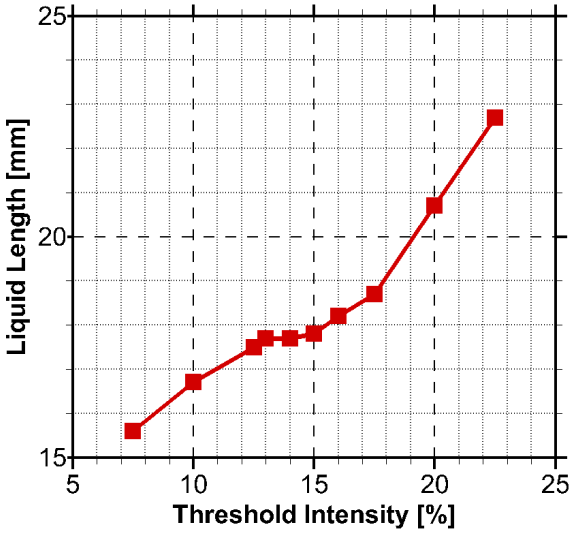

Figure 3.6: Sensitivity analysis applied to Case 1 at 3.05 ms aSOI to determine the correct intensity threshold value.

intensity value to compare each intensity value obtained in the first step. Step one accumulates as many data points for each time step and each pixel location as the number of injections performed, e.g., if 50 injections are performed, each pixel location will have 50 intensity values for each time step. For step two, the reference value is calculated via a sensitivity analysis of intensity. The objective is to determine a threshold value at an inflection point, some percentage of the maximum intensity value ($I = 1$), which does not produce a meaningful change in the desired result (say liquid length as discussed below) for a small variation in the input (intensity threshold value). Figure 3.6 plots the analysis for Case 1 and shows an inflection point for intensity value of about 13 percent or $I = 0.13$. Figure 3.6 reveals an overall "s-curve" shape with three different regions: a near linear response in liquid length with threshold from 7.5-12.5%, the transition region from 12.5-17.5%, and second linear region 17.5-22.5% indicating vapor zone. The non-linear transition region with an inflection point, indicating relative insensitivity to the threshold in determining liquid length, is the most reasonable choice for threshold selection. Thus, the purpose of the sensitivity analysis in Fig. 3.6 is to determine the inflection point, making the methodology much more robust than defining an arbitrary threshold. In this case, the computed liquid length is constant at 17.7 mm at 3.05 ms aSOI for threshold intensity values between 12.5 and 15 percent. Mie scattering employs a similar approach

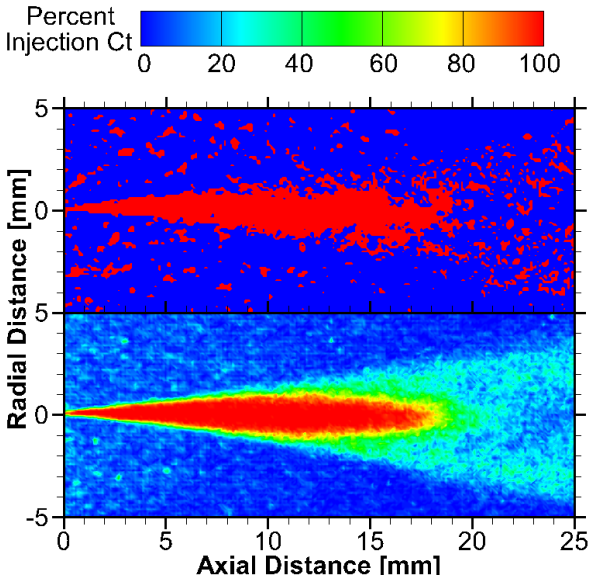

Figure 3.7: (Top) The threshold comparison for a single injection. (Bottom) The 50 injection pixel count for Case 1 at 3.05 ms aSOI for all pixels above the threshold value.

to determine the threshold intensity [53].

The intensity at each time and pixel location is compared with the threshold intensity to create a binary image, i.e., 1 if less and 0 if greater than the threshold value. The top of Figure 3.7 shows an instantaneous binary image for Case 1 at 3.05 ms aSOI. The liquid zone is easily identified as the lumped red region although the liquid boundaries and tip also reveal irregular structures perhaps suggesting ligaments and small-scale structures at the liquid boundary, which is expected in an unstable turbulent jet. Red spots in the background and downstream locations are attributed to the camera noise and minor extinction in the vapor region depending upon the intensity threshold used to create the binary image. The background noise can be mitigated by applying a mask at the edges of the instantaneous image in Fig. 3.7 and will be the focus of future improvements. Next, the binary values are summed for all injections to obtain an injection counter representing the total number of injections for which liquid is present at each time and each pixel location in the spray. The bottom of Fig. 3.7 shows a contour plot of the injection counter at an instant of 3.05 ms aSOI to demonstrate the procedure based on 50 injection experiments. Thus, a 100% injection count at a pixel location signifies that liquid is detected at that pixel location for all 50 injections. Thus, Fig. 3.7 can be

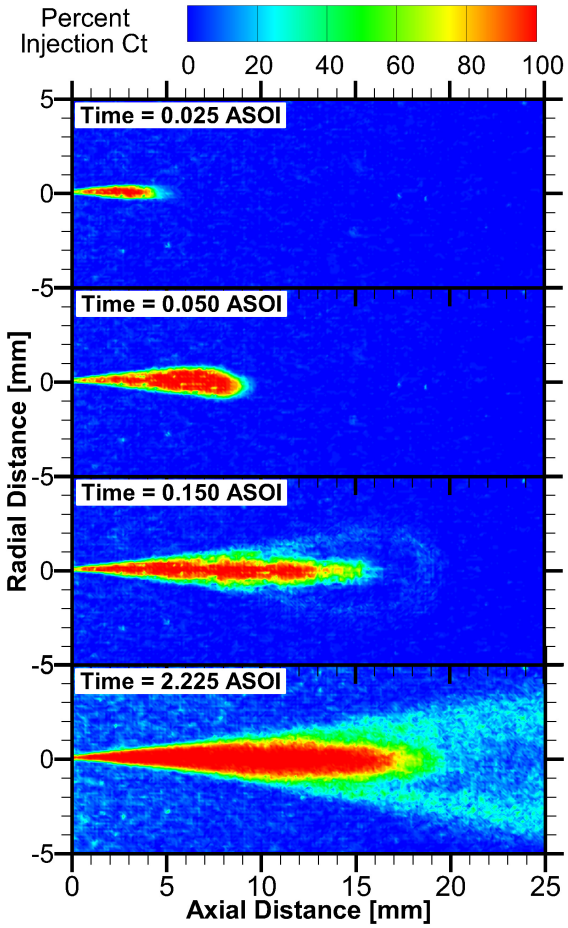

Figure 3.8: Time evolution of injection count color-coded histogram for Case 1.

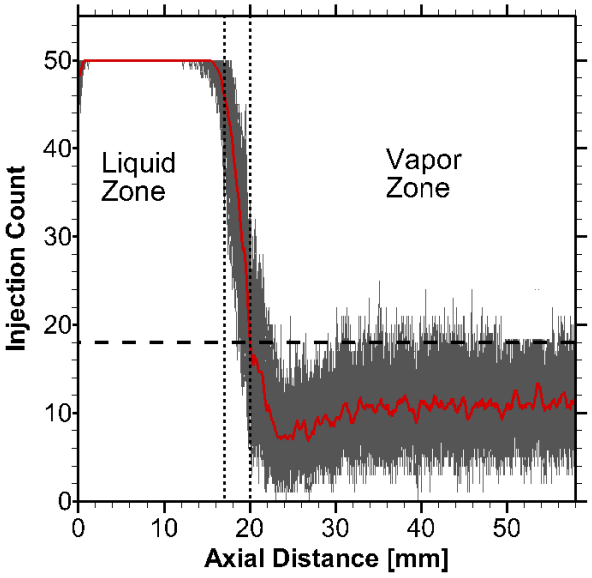

Figure 3.9: All 90 centerline axial profiles of pixel count are plotted in gray during the quasi-steady period of the spray when the vapor has fully penetrated the field of view for Case 1. The mean of all 90 centerline profiles is shown as the red solid line.

interpreted as a kind of color-coded contour plot of phase probability; a higher count (red color) represents higher probability of liquid and lower count (blue color) signifies likelihood of no liquid or high probability of vapor. As mentioned, even in the regions clearly expected to be vapor, pixels occasionally have low intensity, thus a count of below approximately 20 could likely be considered as always being vapor phase - this will further be discussed below. Further, note that the injection count has an averaging effect to filter out the noise in a single binary image to more clearly distinguish the phase boundaries.

The above procedure was used to investigate the phase boundaries of the transient fuel jet. Figure 3.8 shows contour plots of injection count at multiple times aSOI to depict the temporal evolution of the phase boundaries. For early times, 0.025 ms and 0.050 ms aSOI, the fuel jet is mostly liquid. However, for times $>$ 0.150 ms aSOI, the liquid zone is likely surrounded by a vapor zone; a quantitative procedure to demarcate the two zones will be discussed later. The last image corresponding to time 2.225 ms aSOI shows a longer liquid zone (red color) compared to earlier times, and the likely vapor zone (cyan color) extending farther downstream. Note that the injection count image in Fig. 3.8 at 2.225 ms aSOI and that in Fig. 3.7 at 3.05 ms aSOI are nearly the same, which indicates that these times are during the quasi-steady period for Case 1 beginning at about 2.2 ms aSOI. At this time, no significant change in the liquid boundary is observed as will be shown in Fig. 3.11. For Case 1, about 90 images were acquired during the quasi-steady period for each of the 50 injection experiments.

The procedure to demarcate the phase boundaries will be discussed next with reference to Fig. 3.9 showing the axial profiles of injection count along the centerline of the jet during the quasi-steady period (2.2 ms - 4.2 ms). Ninety profiles corresponding to 90 images acquired during the quasi-steady period are plotted. The red line represents the average of all 90 injection count profiles. The liquid zone is easily identified - in this zone the injection count is nearly 50, i.e., the probability of liquid is 100 % or liquid is detected in all of 50 injection experiments. Ideally, an injection count of 50 would be used to demarcate the liquid boundary. However, it was found that using an injection count value of 47 ($<$95%) helped mitigate algorithmic issues and provided

more consistent behavior. Based on this procedure, the liquid length for Case 1 was found to be 17.3 mm. A sensitivity analysis was performed to investigate the effect of changing the injection count by ±1. This change shifted the liquid boundary only by 1-3 pixels or 100-300μm indicating robustness of the present approach. Besides the liquid zone, Figure 3.9 illustrates two other regions: (1) the downstream vapor zone where the injection count is low; the injection count varies from shot to shot but the average value is constant (about 10 on average) in the axial distance, and (2) an in-between transition zone where the injection count decreases quickly from a high to a low value; the high value means high probability of liquid and the low value signifies low probability of liquid. The transition region represents a stochastic behavior of the liquid zone between consecutive injections perhaps caused by the break-off of ligaments and droplets at the edges of the liquid jet [102]. The downstream edge of the transition region, also referred to as the outer liquid boundary in this study, is difficult to define precisely. Thus, the highest injection count in the downstream vapor region based on two standard deviations, i.e., a value of 18, is used to determine the end of the transition region or the outer liquid boundary located at an axial distance of 20 mm. The change in the injection count by ± 1 shifted the outer liquid boundary only by 100-300μm indicating that the results are minimally affected by the injection count. Thus, the transition region extends between 17.3 mm and 20 mm corresponding to the injection count of 47 and 18, respectively. Lumping the transition region with the liquid zone, the liquid length is bounded by the minimum and maximum value of 17.3 mm and 20 mm, respectively. The outer liquid boundary is also the inner vapor boundary beyond which the RSD can be applied to quantify the density and/or equivalence ratio measurements. The method outlined in this section illustrates a stark difference between the (inner) liquid boundary and outer liquid boundary. Moreover, both of these boundaries can be reliably found from just 50 images as opposed to 2,000 images in the method described in Ref. [113].

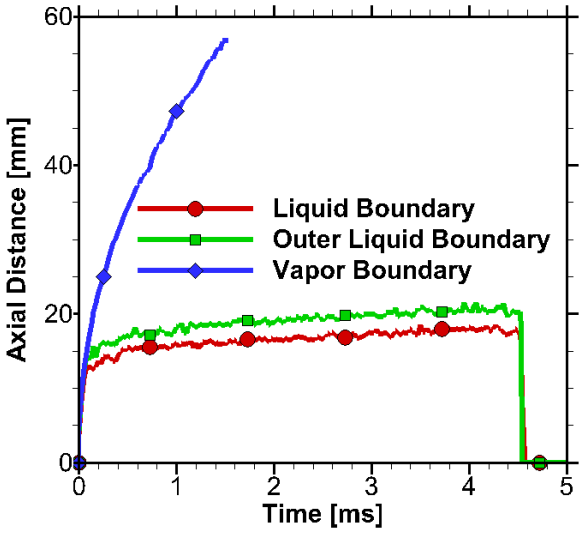

Figure 3.10: Transient penetration of liquid, outer liquid and vapor penetration of Case 1.

3.5 Results

In addition to detecting the liquid and outer liquid boundary, the hue signal from RSD measurement can be used to identify the outer edge of vapor boundary. At the vapor boundary, the hue is within a few degrees of the background hue. In this work it was further determined that injection count discussed above provides the same results as hue signal to detect the outer vapor boundary. The vapor zone also decreases the intensity and thus, the injection count will be greater than that of the background as shown in Figure 3.7. Thus, either hue or injection count can be used to determine the vapor boundary, thereby, enabling RSD to track all of the phase boundaries as a function of time; the results are shown in Fig. 3.10.

Figure 3.10 shows the time evolution of the liquid boundary, outer liquid boundary, and vapor boundary acquired over 50 injections. The vapor boundary reaches the downstream edge of the field of view at around 1.4 ms aSOI, hence the data is truncated at this point. Figure 3.10 illustrates the growth of the liquid boundary and outer liquid boundary as a function of time. After initial development, the liquid length continues to increase slightly with time, which is consistent with data in the ECN database [89]. Cooling of the surrounding ambient gas by the injected fuel will decrease the heat transfer rate between fuel and ambient at later times, thereby causing an increase in the liquid

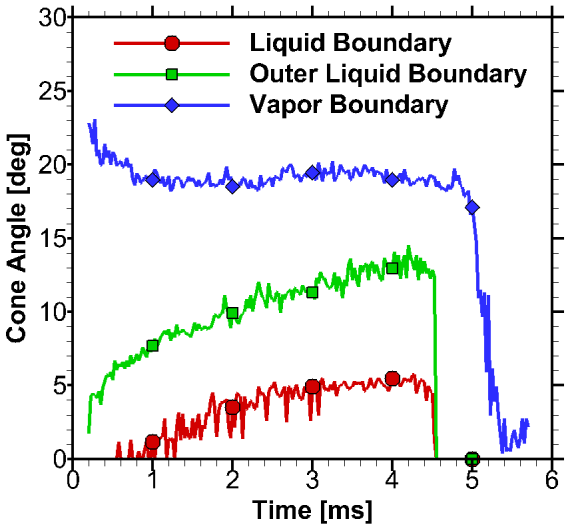

Figure 3.11: Full liquid, outer liquid, and vapor cone angle versus time at an axial location of 15 mm for Case 1. The angles in this plot were calculated from the boundary from each color-coded histogram (Fig. 3.8) at each time step.

length. Further, colder liquid fuel (heptane and dodecane) results in an increase in the kinematic viscosity which prolongs the initial jet breakup [20]. Additionally, over the course of a long injection, the fuel temperature at the nozzle exit may change as the injected fuel might originate from the cooler part of the upstream injector body [90]. These effects combine to produce the results observed in Fig. 3.10. Liquid and outer liquid boundaries in Fig. 3.10 show undulations attributed to injection-to-injection variations and the turbulent nature of the spray. These results further demonstrate the stochastic nature of the liquid zone as shown in Fig. 3.7.

In the same manner as the penetration length, the radial boundary for each portion of the jet is determined by implementing a radial search algorithm from the centerline to find the first pixel count equal to the given threshold value. Once boundaries for the liquid zone, outer liquid region, and vapor zone are determined for each time step, the cone angle is calculated to illustrate the time evolution at an axial location of 15 mm in Fig. 3.11 and the axial evolution during the quasi-steady period in Fig. 3.12. Figure 3.12 utilizes the boundaries of the ninety quasi-steady frames to compute a quasi-steady average cone angle. The cone angle is defined as $\tan[\frac{W}{D}]$, where W is the full width of the liquid zone, outer liquid, or vapor region, and D is the corresponding axial distance. Figure 3.11 illustrates that at an axial location of 15 mm, both outer liquid and the vapor boundaries

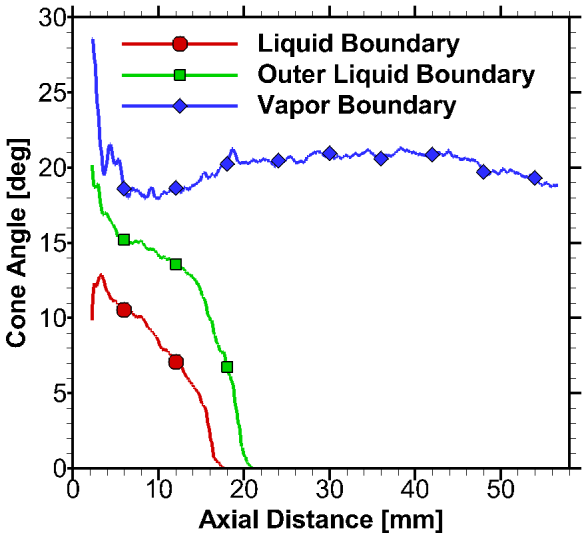

Figure 3.12: Full liquid, outer liquid, and vapor cone angle versus axial distance for the quasi-steady portion of the spray during Case 1. The cone angles in this plot were determined from an average of ninety boundaries of quasi-steady color-coded histograms in Fig. 3.8.

are present at 0.25 ms while the liquid becomes apparent at approximately 0.75 ms. It is possible that the arrival of the outer liquid and vapor boundaries could be distinguished by increasing the temporal resolution. Figure 3.11 shows that the vapor cone angle initially decrease and then, remains constant from 1 ms to 5 ms aSOI. However, the cone angle for the liquid boundary and outer liquid boundary increases gradually with time, which is consistent with the gradual lengthening of the liquid jet as explained earlier. The cone angle is proportional to the ambient density [87] and hence, the observed increase in the cone angle can be explained by the cooling, and thus, increase in the density at the jet periphery by the cold liquid fuel. Results clearly show that even during the so-called quasi-steady portion of the injection, the liquid and outer liquid boundaries continue to slightly evolve, which is consistent with liquid length data from the ECN data base. The sudden decrease in cone angle for all three boundaries corresponds to the end of injection. As expected, the vapor zone is present till about 5.4 ms even though the liquid zone is absent after about 4.5 ms.

Figure 3.12 shows the axial development of the full cone angle during the quasi-steady portion of the injection. The cone angle for the liquid boundary and outer liquid boundary decreases in the axial direction, while that for the vapor boundary decreases initially and

then increases to reach a nearly constant value of approximately 20 degrees. Full cone angle of zero signifies the termination of the liquid zone or outer liquid boundary, which occur at around 17.3 mm and 20.0 mm, respectively as discussed previously. Very near the injector, an error of just a few pixels can make a large difference in calculating the cone angle, and thus, the nearly 30 degree initial vapor angle is numerical rather than a physical effect.

The technique can be further improved by increasing the number of injections. This is demonstrated for Case 3 using liquid propane to also confirm the validity of the present methodology for a different fuel. For propane, 93 injection experiments were performed, limited by the on-board camera memory. Increasing the number of injections improves the statistical analysis and reduces the background noise; providing more clear distinction among the liquid zone, outer liquid boundary, and vapor boundary. Figure 3.13 shows the contour plots of the percent of injection count to indicate the liquid, outer liquid, and vapor boundaries during the transient evolution of the fuel jet. The colormap for this Figure has been changed to increase contrast between the vapor region and background. All three boundary nearly overlap at the start of the injection, i.e., time = 0.05 ms aSOI. Once the liquid boundary approaches its maximum penetration at time = 0.10 ms aSOI, the outer liquid boundary and vapor boundary separate. Thereafter, the outer liquid boundary reaches quasi-steady length, but the vapor boundary continues to penetrate farther downstream, eventually escaping the field of view at time = 2.7 ms aSOI. Recall that Figure 3.13 is a color-coded plot related to the probability of different zones during the transient evolution of the fuel jet, providing a robust statistical approach to delineate the phase boundaries in the fuel spray.

3.6 Discussion

Measurements obtained by the methodology outlined above are compared against Siebers' liquid length scaling law [105] shown in Eq. 3.1 for Cases 1 and 2.

$$L = \frac{b}{a}\sqrt{\frac{\rho_f}{\rho_a}}\frac{\sqrt{C_a}d}{\tan(\theta/2)}\sqrt{\left[\frac{2}{B(T_a, P_a, T_f)} + 1\right]^2 - 1} \tag{3.1}$$

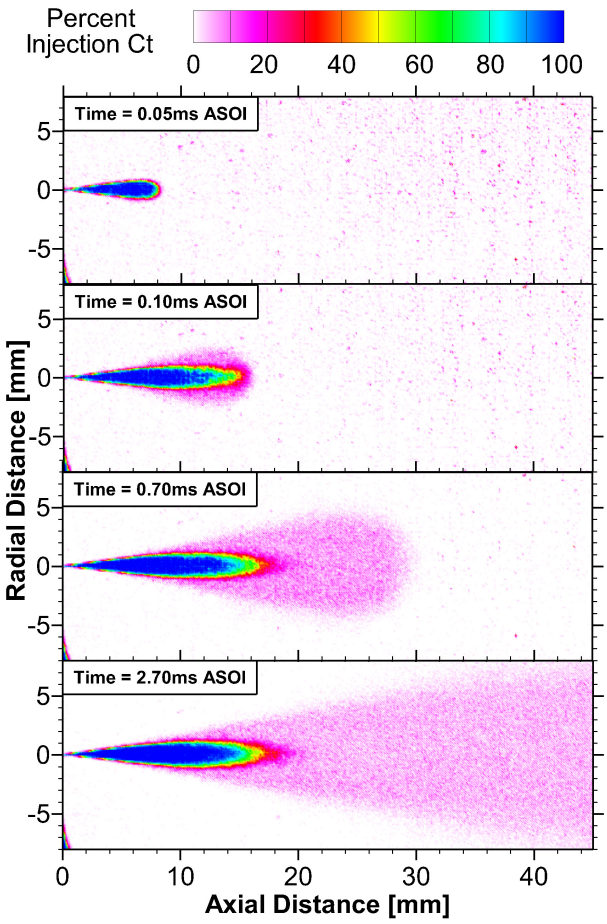

Figure 3.13: Transient evolution of injection count color-coded histogram for Case 3 consisting of 93 injections.

Table 3.2: **Comparison of liquid boundary, outer liquid boundary and Siebers' model for the two n-heptane cases.**

Case	Liquid Length (mm)	Outer Liquid Length (mm)	Siebers' Model (mm)
1	17.3±1.1	20.0 ±1.2	20.2
2	9.0±0.7	10.3 ±1.0	10.8

Equation 3.1 is a simple solution for equilibrium mixing of air and fuel assuming the fuel has vaporized. For more information regarding the terms in Eq. 3.1 see Ref. [105]. Table 3.2 lists the measured liquid length and outer liquid length and the values predicted by the Siebers' scaling law. Experimental results are obtained by time averaging the measurements during the quasi-steady period, i.e., from 2.2 ms - 4.2 ms and 1.725 ms 2.5 ms aSOI for Case 1 and 2, respectively. Statistical variation in the measured penetration length is defined as 2 standard deviations from the mean value. Siebers' scaling law has two empirical tuning constants adjusted to match Mie scatter data [105]. Results in Table 3.2 show that the measured outer liquid length and predicted liquid length agree with each other, while the measured liquid length is shorter.

The present results can be used to compute the probability of liquid existence. This is obtained by considering the upper limit of pixel count in the vapor zone i.e. two standard deviations above the mean in Fig. 3.9 as the zero percent probability indicator. A probability is then computed using Eq. 3.2.

$$P = \frac{\text{Injection count} - (\mu + 2 * \sigma)}{\text{N} - (\mu + 2 * \sigma)} \tag{3.2}$$

Where μ and σ are the mean and standard deviation of the vapor zone pixel count value, and N is the total number of injections. For this work, $\mu + 2 * \sigma$ corresponds to the horizontal dashed line in Fig. 3.9 at an injection count of 18 and N= 50. Thus, a probability map is computed for Case 1 in Fig. 3.14. The liquid boundary refers to 95 percent probability of liquid and is identified as the thin black curve in the red region. The 0% probability line is the outer liquid boundary shown as the black dashed line. For in-between region, the injection-to-injection probability of liquid varies between 100 % and 0%, and represent the edges of the liquid boundary where ligaments are being shed

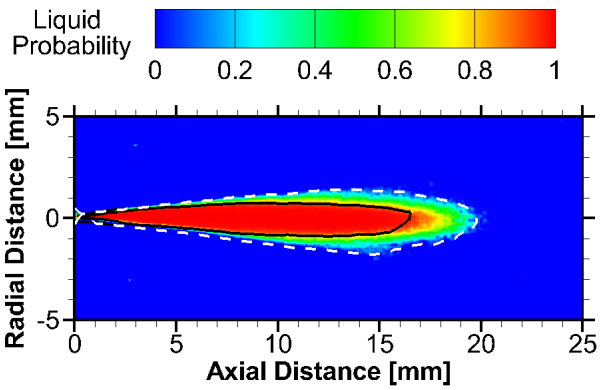

Figure 3.14: A liquid existence probability contour map is shown for the quasi-steady period of the spray. The inner and outer liquid boundary are as the solid black and dashed white lines, and represent the region of 95% and 0% probability, respectively.

and droplets are being formed as shown by the instantaneous binary plot in Fig. 3.7. Thus, this region represents the two-phase zone where phase liquid and vapor phases exist simultaneously, albeit with varying probability.

A detailed comparison of the old RSD method in Ref. [113] and the present RSD method is made in Fig. 3.15 for Case 1 using the average saturation image. The old RSD method could detect only the liquid boundary for the quasi-steady period. In Fig. 3.15, the liquid boundary based on the old RSD method is shown as the dashed black line, and results from the new RSD method, liquid and outer liquid boundaries, are shown as thin black profiles. Note that the old RSD method uses the background intensity as the threshold to identify the liquid boundary. The background intensity is lower than that of the vapor zone, and hence, a portion of the dense vapor zone(s) can also be interpreted as the liquid zone, thereby, overly extending the liquid boundary or the liquid length. The new RSD method determines the intensity threshold based on a sensitivity analysis of the liquid zone, yielding a value much lower than that of the background. The methodology employed in this work seems to predict liquid length trends similar to those in Ref. [120].

The study in Ref. [120] has shown that beam steering can artificially increase the measured liquid length. Beam steering is the deflection of light rays by refractive index gradients in the test media, and it is in fact the signal represented and quantified by hue in the RSD image. RSD relies upon independent measurements of hue, saturation, and intensity as discussed before and illustrated by the cone in Fig. 3.4. We hypothesize

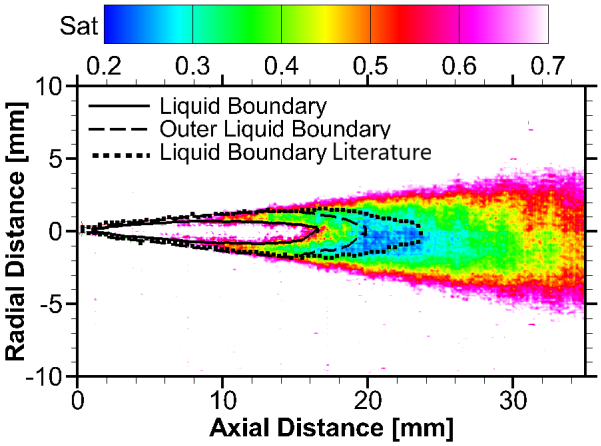

Figure 3.15: Average saturation is determined for the quasi-steady period of the spray for Case 1. The liquid boundary (solid black curve) and outer liquid boundary (black long-dashed curve) are shown and compared to the liquid boundary using the methodology in Ref. [113] (black short-dashed line)

.

that beam steering can negatively affect the hue signal in RSD for two situations: (1) large beam steering will cause light rays to displace outside the colored portion of the filter. This effect can occur for rays passing through large density gradients existing in regions immediately downstream of the liquid boundary. In the RSD image, pixel locations mapping such rays will appear white, i.e., high intensity and no color or zero saturation, and (2) multiple rays passing through different color portion of the filter but mapping on the same pixel location in the RSD image affecting both hue and intensity values. In both of these situations, the hue (color) will be difficult to distinguish, i.e., low saturation.

These two scenarios can occur with little or moderate light attenuation. The former is represented by Region A in Fig. 3.4 while the latter is represented by region B in the saturation-intensity coordinates of the HSI color space. In either case, beam steering would make it difficult to detect hue at pixel locations with sufficiently high intensity but low saturation, although a detailed analysis of the cut-off values is beyond the scope of this study. In the liquid region, the light rays are scattered or absorbed and do not reach the camera sensor. In these low intensity regions, hue measurements are greatly affected by the camera noise and thus, they cannot be relied upon for the quantitative analysis. The corresponding color space can be represented by Region C in Fig. 3.4, i.e., low intensity

regardless of the saturation. In summary, the RSD density measurements would be valid only in Region D which is outside regions A, B and C in Fig. 3.4. Compound threshold values of $I > 0.1$ and $S > 0.1$ seems to suffice for cases considered so far. The vapor zone outside the outer liquid boundary satisfies these criteria (more than 95 percent of the pixels in the vapor zone are in region D of Fig. 3.4) although regions below a saturation threshold could be subject to greater uncertainties.

Figure 3.15 shows the average saturation contour during the quasi-steady period to assess the above hypothesis. The Figure shows that the average saturation within the liquid boundary is quite high (>0.8) and it remains high (> 0.5) within the outer liquid zone. Thus, it is unlikely that beam steering affects the present RSD method to detect liquid and outer liquid boundaries. However, Fig. 3.15 illustrates that liquid boundary obtained by the old RSD technique encompasses the low saturation region at axial locations between 20 mm and 24 mm attributed to beam steering. Thus, the old RSD technique validated with Mie scattering was likely affected by beam steering. However, the new RSD technique is not affected by beam steering, while it can also provide insight between inner liquid and outer liquid boundaries based on a statistical approach.

3.7 Conclusions

In this study, rainbow schlieren deflectometry (RSD) is used to detect the phase boundaries during transient evolution of an evaporating high-pressure fuel spray in heated ambient environment. The methodology relies on repeated injection experiments ($\geq$50) and leverages the intensity signal of the RSD images to determine the phase boundaries on a statistical basis. The method is used to find the liquid boundary within which liquid is always present (95 percent probability of liquid) and the outer liquid boundary outside of which liquid is unlikely to be present (zero probability of liquid). Both phases are potentially present in the intervening region between liquid and outer liquid boundaries, which is consistent with the instantaneous images showing ligaments and small-scale structures in this region.

Results for liquid n-heptane fuel revealed that predictions from the Siebers' scaling

law agree with the outer liquid boundary length measured by the present RSD technique. Thus, predictions provided a conservative estimate of the liquid length, which can be explained by recognizing that the scaling law is tuned to the Mie scattering technique, now established to yield an exaggerated liquid length because of beam steering effects. It is shown that beam steering is unlikely to affect the liquid boundary detection determined by the new RSD methodology. The shorter liquid length measured by the new RSD method is consistent with the recent findings of Ref. [120] although a direct comparison of the two techniques is planned for future work.

The transient analysis capability of the method is used to compute the temporal evolution of various boundary lengths and cone angles throughout the injection period. Results show that after an initial ramp-up, the liquid boundary length continues to increase, albeit slowly, indicating that a true "steady-state" might not exist in diesel combustion.

This work demonstrates a computationally efficient algorithm requiring much less data than the RSD technique presented previously and extends the method for the transient analysis. In summary, it proves RSD as an all-encompassing diagnostic technique to not only obtain quantitative fuel-air mixing measurements in the vapor phase but also to accurately identify single and two-phase regimes in harsh operating conditions.

3.8 Funding Information

This material was supported by the Department of Energy, Office of Energy Efficiency and Renewable Energy (EERE) and the Department of Defense, Tank and Automotive Research, Development, and Engineering Center (TARDEC), under Award Number DE-EE0007301.

CHAPTER 4
IMPLICATIONS OF REAL-GAS BEHAVIOR ON REFRACTIVE INDEX CALCULATIONS FOR OPTICAL DIAGNOSTICS OF FUEL-AIR MIXING AT HIGH PRESSURES

4.1 Abstract

Three models to compute the refractive index of gaseous mixtures at real gas conditions are presented with the purpose to improve the accuracy of state relationships between refractive index and thermodynamic properties. Models are compared with experimental data to determine one that is applicable to high pressure mixtures with non-ideal thermodynamic behavior near or above a fluids' critical point. The optimal model is applied to analyze adiabatic thermal mixing of fuel and air at typical diesel engine conditions. Results show that the ideal gas mixture law is appropriate in the vapor region, assuming it is known, for example, from experimental measurements. Finally, the model is applied for binary fuel-air mixing at supercritical conditions to demonstrate its full potential. The theoretical analysis in this work provides the necessary tools to extend RSD to non-ideal gas regions of fuel sprays.

4.2 Introduction

For combustion applications such as diesel engines and gas turbines, fuel is injected into a hot, high pressure oxidizer environment. Ambient air entrainment and turbulent mixing with fuel results in a gaseous phase fuel-air mixing region containing the combustible mixture. Rayleigh scattering can be used to acquire vapor-phase fuel concentration and temperature measurements [41, 52]. In two-phase systems, the Rayleigh scattering signal of the vapor phase must be separated from the Mie scattering signal of

the liquid phase. Thus, Mie and Rayleigh scattering diagnostics are often used together, though not simultaneously, to distinguish each phase [3]. Rayleigh scattering is the elastic scattering of light quanta from particles smaller than the wavelength of light, and the measured intensity of the Rayleigh signal (I_R) can be related to the local gaseous mixture properties using Eq. 4.1 [41].

$$I_R = C I_l N \sum_i X_i \sigma_i \tag{4.1}$$

Where C, I_l, N, X, and σ are respectively the calibration constant, intensity of the incident light, total number density (molecules per m^3), mole fraction, and Rayleigh scattering cross section. The subscript i represents a species in the gaseous mixture. The Rayleigh scattering cross section is related to the incident light wavelength (λ) and the species refractive index (n) according to Eq. 4.2 [75].

$$\sigma_i = \frac{24\pi^3}{\lambda^4}\left[\frac{n^2-1}{(n^2+2)N_0}\right]^2 = \frac{24\pi^3}{\lambda^4}\left[\frac{r_e}{N_0}\right]^2 \tag{4.2}$$

Where N_o is the total molecular number density at standard pressure and temperature (STP), and the refractivity (r_e) is substituted for the refractive index terms. In the engine community for n $\approx$ 1 , the refractivity (r_e) in Eq. 4.2 is approximated by Eq. 4.3:

$$r_e = \frac{n^2-1}{(n^2+2)} \approx \frac{2}{3}(n-1) \tag{4.3}$$

thereby approximating the Rayleigh cross-section as Eq. 4.4 [41].

$$\sigma_i = \frac{24\pi^3}{\lambda^4}\left[\frac{2(n_i-1)}{3N_0}\right]^2 \tag{4.4}$$

For an ideal gas, the number density, N, is determined from the total inlet enthalpy by assuming adiabatic fuel-air mixing [41, 124] as outlined in the ECN [89]. Relating Rayleigh signal to species mole fraction using Eq. 4.1 and Eq. 4.4 requires relationships between the refractive index and the thermodynamic properties (i.e., state relationships) for each species as inputs.

In recent years, the line-of-sight rainbow schlieren deflectometry (RSD) technique

has been used to obtain the thermodynamic properties in laminar gaseous systems, as outlined in Ref. [5]. However, Wanstall *et al.* have shown the potential of RSD for quantitative measurements in the fuel-air mixing region of diesel sprays [113]. They developed the RSD methodology to simultaneously detect the liquid phase boundary and estimate thermodynamic properties in the surrounding vapor zone to overcome the need for requiring two separate diagnostics for such measurements [113, 115]. RSD directly measures the refractive index which can be related to the thermodynamic properties using the state relationships discussed previously. For an ideal gas with $n \approx 1$, refractive index is related to density using the Dale-Gladstone equation:

$$n - 1 = k\rho = k\frac{PM}{\overline{R}T} \tag{4.5}$$

Where k is the Dale-Gladstone constant, P is the pressure, M is the molecular weight, $\overline{R}$ is the universal gas constant, and T is the temperature. For an ideal gas mixture,

$$n - 1 = k_{mix}\rho_{mix} = \frac{P}{\overline{R}T}\sum k_i M_i X_i \tag{4.6}$$

where , X is the species mole fraction, and subscript i refers to species i. The Dale-Gladstone relation uses the same linearized approximation for refractive index ($n \approx 1$) shown in Eq. 4.3. Thus, both Rayleigh scattering and RSD rely upon the state relationships between refractive index (only the real-part is considered here) and thermodynamic properties, e.g., Eq. 4.5 for an ideal gas and Eq. 4.6 for ideal gas mixtures.

Both Rayleigh scattering and RSD have been used to obtain accurate measurements in combustion environments at atmospheric pressures [8, 72]. However, state-of-the-art combustion engines operate at high pressures (e.g., cylinder pressures exceeding 100 bar in diesel engines) and thus ideal gas law and/or ideal mixing laws (e.g., Amagat's Law) may not be applicable. Recent experimental and theoretical findings have challenged the conventional paradigm by suggesting that the pressure and temperature in modern diesel engines can exceed the thermodynamic supercritical conditions for liquid/gas mixtures in regions of the fuel jet [25–30, 42, 43]. Thus, the mixing processes and mixture laws

in fuel spray could be different than conventionally described. [59, 103]. Oefelein *et al.* have described the evolution of a purely supercritical spray without liquid droplets and surface tension forces where mixing between the fuel jet and the surrounding ambient is dominated by turbulent diffusion [81]. These non-ideal gas conditions require real fluid thermodynamic mixture models. Large eddy simulations (LES) studies based on real fluid equation of state (EOS) have determined that the fuel-air mixing is profoundly modified by the non-ideal gas thermodynamic properties [58,82,112]. Recently, Crua *et al.* showed that the fuel-air mixing at diesel conditions can occur by the classical evaporation of fuel droplets, purely diffusive mixing between supercritical fuel and ambient air, or a combination of both, i.e., transcritical mixing, depending on the pressure and temperature of the ambient environment [25].

The above review raises the following important question, "Are current ideal gas mixture laws relating refractive index to thermodynamic properties valid for applications such as modern diesel environments where the gaseous mixtures can be non-ideal?". Thus, the objective of this study is to develop a robust model to relate optical (e.g, refractive index) and thermodynamic (e.g., density) properties of real-gas mixtures at high pressures. This paper is divided into six more sections. First, the Lorentz-Lorenz equation providing the link between a microscopic quantity (polarizability) and a macroscopic quantity (refractive index) is presented. The next two sections discuss polarizability and thermodynamic models for pure substances and gaseous mixtures. Then, three different models are presented to compute the refractive index of a real gas mixture, and compare them against experimental data available in the literature. Next, the refractive index models are investigated for an extensive range of diesel engine conditions including Spray A, as defined by the ECN community [89]. Then the best model is applied to the problem of fluid mixing at supercritical conditions to demonstrate its full potential. Finally, the conclusions of the paper are summarized.

4.3 Lorentz-Lorenz Equation

The theoretical basis for relating refractive index to density is embedded in the state equation of electromagnetic polarization established in the late 19^{th} and early 20^{th} century [9,67]. As the electromagnetic wave travels through a medium, the wave's phase velocity changes proportionally to the refractive index of the substance. At the atomic level, this is caused from disturbances created by the electromagnetic field in the charge of each atom (mostly electrons), and how closely the charges are packed (density). The susceptibility of the substance to these disturbances is called the molecular polarizability, α. The end result is the so called Lorentz-Lorenz equation relating refractive index to molecular polarizability (α) and molar density ($\overline{\rho}$) shown in Eq. 4.7 from which the Dale-Gladstone equation (Eq. 4.5) is derived. The Lorentz-Lorenz equation applies to an isotropic system containing non-polar substances with no molecular interactions, e.g., each molecule is treated as an isolated system.

$$r_e = \frac{n^2 - 1}{(n^2 + 2)} = \frac{N_A \alpha}{3} \overline{\rho} = \frac{N_A \alpha}{3M} \rho \tag{4.7}$$

Where N_A, α, and M are Avogadro's number (constant), mean molecular polarizability, and molecular weight, respectively. Note that Eq. 4.7 can be written either using molar or mass density (ρ). For $n \approx 1$, the Lorentz-Lorenz equation (Eq. 4.7) can be simplified to the Dale-Gladstone formulation (Eq. 4.5) in which the Dale-Gladstone constant is:

$$\kappa = \frac{3}{2} \frac{N_A \alpha}{3M} \tag{4.8}$$

Figure 4.1 plots the error in refractivity r_e introduced by the Dale-Gladstone approximation for various hydrocarbons, and highlights regions with errors greater than 5 and 10 percent. The exponential of r_e is shown on the vertical axis to highlight the difference between Lorentz-Lorenz and Dale-Gladstone equations. Considering the error introduced by the Dale-Gladstone approximation, especially at high refractive index values, it is not recommended for the analysis. The Lorentz-Lorenz Eq. 4.7 requires virtually no additional

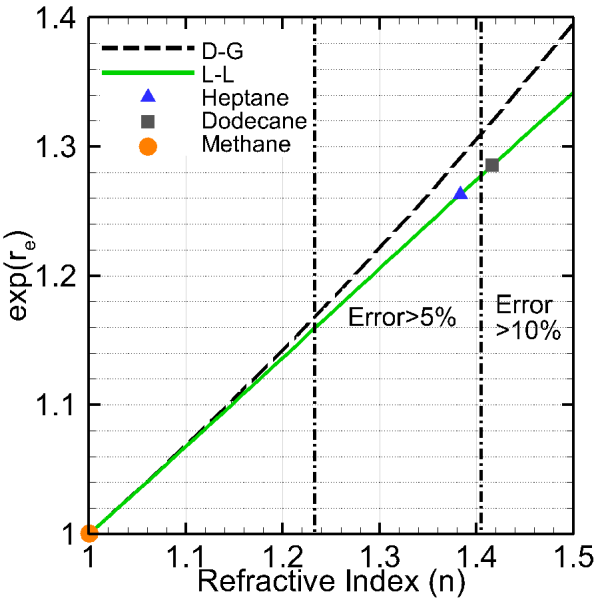

Figure 4.1: A plot showing the exponential of refractivity (r_e) based on the Lorentz-Lorenz (L-L) equation and the Dale-Gladstone (D-G) approximation for three different fuels.

effort with today's modern computing power. Thus, moving forward, the Lorentz-Lorenz Eq. 4.7 will be used and the Dale-Gladstone Eq. 4.5 will not be considered.

The primary focus of the present study is to extend Eq. 4.7 for gaseous mixtures at high pressures. This requires accurate models to relate the mixture refractivity (or mixture refractive index) to polarizability and density of the mixture and/or its components. In the next two sections, polarizability and density calculations for pure substances and mixtures are discussed, and then, different refractivity mixture models analyzed in this work will be introduced.

4.4 Polarizability Models

4.4.1 Single Component

Polarizability is often reported in the literature at standard temperature and pressure (STP), T = 273 K and P = 1 bar. Gardiner *et al.* provide a detailed data set for polarizability of numerous combustion related substances in [46], and Bosque *et al.* provide one of the largest experimental data sets for polarizability with over 400 compounds including many diesel surrogate fuels [13] such as *n*-heptane and *n*-dodecane. However, the validity

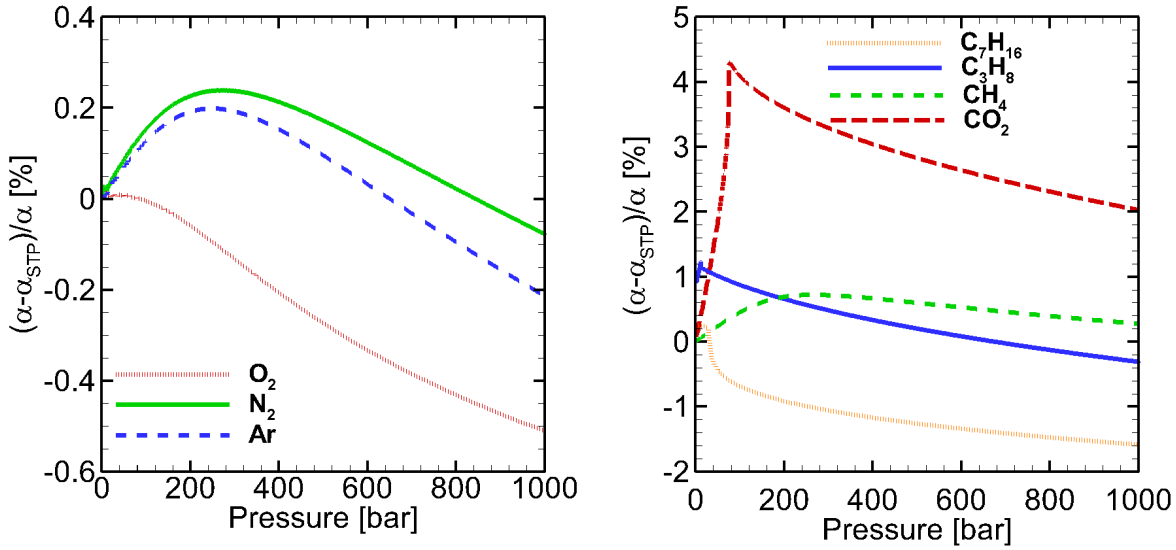

Figure 4.2: Effect of pressure on polarizability of constituents of air (top) and hydrocarbons and carbon dioxide (bottom). The vertical axis shows the percent change in polarizability with respect to the value at STP (273 K and 1 bar) except 550 K and 1 bar for n-heptane.

of using polarizability data at STP for applications at high pressures or temperatures is not immediately clear. Thus, existing literature was searched to identify experimental studies that report polarizability of several gases as functions of pressure and temperature [2, 51, 100]. Figure 4.2 shows the percent change in polarizability with pressure for seven species relevant to this study at a constant temperature of 305 K except for heptane at 550 K, i.e., close to its critical temperature.

Figure 4.2 shows a slight increase and then decrease in polarizability with increasing pressure for all seven species. However, the change in polarizability with pressure is small, less than 1 percent, except for CO_2 at around its critical point of 304 K and 73.9 bar where the difference from the STP value is about 4.5%. Polarizability also has a slight linear temperature dependence [51], especially for propane among the seven species considered in this study. However, at some pressures/temperatures the temperature effect counteracts the pressure effect, e.g., the temperature effect can cause a decrease in polarizability while the pressure can cause an increase [51]. Still, the effect of pressure and temperature on polarizability is quite small for combustion relevant species, less than 5% of the value at the reference conditions. Thus, following the Lorentz-Lorenz formulation of Eq. 4.7,

polarizability at STP is used to rewrite Eq. 4.7 as Eq. 4.9

$$r_e = \frac{n^2 - 1}{n^2 + 2} = \overline{A}\overline{\rho} = A\rho \tag{4.9}$$

where $\overline{A} = \frac{N_A \alpha}{3}$ and $A = \frac{N_A \alpha}{3M}$ are, respectively, mole and mass based constants. More advanced forms of the Lorentz-Lorenz Eq. 4.7 have been developed by Buckingham [16–18] where the refractivity (or refractive index) is calculated from a higher order virial expansion as shown in Eq. 4.10. Equation 4.10 accounts for pressure and temperature effects on polarizability as shown in Fig. 4.2.

$$r_e = \frac{n^2 - 1}{n^2 + 2} = [\overline{A} + \overline{B}\overline{\rho} + \overline{C}\overline{\rho}^2 + ...]\overline{\rho} \tag{4.10}$$

4.4.2 Mixtures

For mixtures, Buckingham *et al.* [19] derived a theoretical basis for Eq. 4.10 as shown in Eq. 4.11.

$$\overline{A}_{mix} = \sum_i \overline{A}_i X_i \tag{4.11a}$$

$$\overline{B}_{mix} = \sum_{i,j} \overline{B}_{i,j} X_i X_j \tag{4.11b}$$

The constant $\overline{A}$ is the same as in Eq. 4.9. However, the coefficient $\overline{B}$ requires an interaction term (B_{ij}) which is generally unknown. Since the higher order virial coefficients are negligible (as shown in the last section), the first term alone (i.e., $\overline{A}$) is a good approximation to compute the mixture polarizability, and will be used in this study. Nearly linear behavior of mixture polarizability ($\overline{A}_{mix} = \sum_i \overline{A}_i X_i$) has been observed in supercritical environments for methanol-carbon dioxide and ethanol-carbon dioxide mixtures [49, 108].

4.5 Thermodynamic Models

4.5.1 Single Component

Real fluid EOS are well-developed for determining thermodynamic properties at non-ideal gas conditions. The most useful EOS are semi-empirical or empirical in nature.

Once reasonable computing power became available in 1960s, empirical multiparameter EOS became the new standard [106].

The most recent and accurate multiparameter EOS are formulated in terms of reduced Helmholtz energy, a. Equation 4.12 shows the form of the reduced Helmholtz EOS [96]

$$\begin{aligned} \frac{a(T,\rho)}{RT} &= \frac{a^{IG}(T,\rho) + a^{R}(T,\rho)}{RT} \\ &= f^{IG}(\tau,\delta) + f^{R}(\tau,\delta). \end{aligned} \tag{4.12}$$

where T is temperature, R is the ideal gas constant, the parameters δ and τ are the reduced density and temperature based on the critical values (ρ/ρ_c and T_c/T). The superscripts IG and R stand for the ideal gas and residual, respectively. The ideal gas Helmholtz energy is generally obtained from the isobaric ideal gas heat capacity correlation shown in Eq. 4.13

$$\begin{aligned} a^{IG} = a_o + \int_{T_o}^{T} (c_P^{IG} - R)dT - \\ T\int_{T_o}^{T} \frac{c_P^{IG} - R}{T} dT + RT\ln(\frac{\rho}{\rho_o}). \end{aligned} \tag{4.13}$$

where c_p is the specific heat and the subscript o refers to a chosen reference state. Often empirical calorimetric data (c_p) are correlated with polynomial functions [96].

The residual part, loosely supported by theoretical considerations, is given by a general empirical function:

$$f^{R}(\tau,\delta) = \sum_{k=1}^{k=n} N_k \delta^{d_k} \tau^{t_k} + N_k \delta^{d_k} \tau^{t_k} \exp(-\delta^{l_k}). \tag{4.14}$$

Where N, d, t, and l are substance specific coefficients determined by a complex multivariable fitting procedure; in which the summation contains between 4-20 terms [60]. Often vapor-liquid equilibrium of a substance is utilized to optimize these EOS parameters. Once the EOS is determined, consistency can be checked by ensuring that pressure (P), temperature (T), and Gibbs function ($\overline{g}$) values follow vapor-liquid (V and L) equilibrium

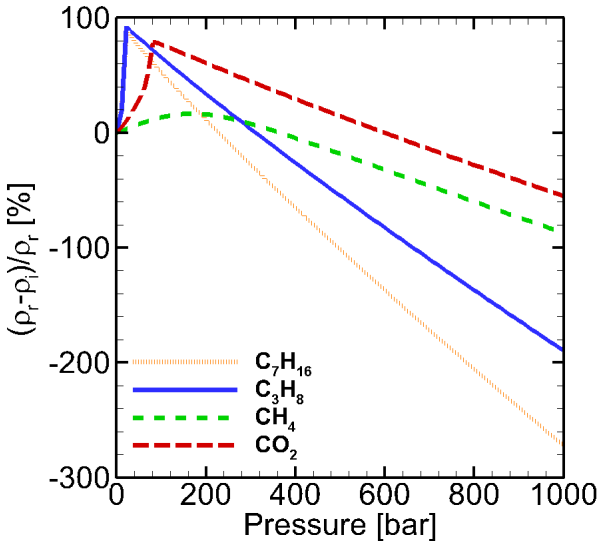

Figure 4.3: Effect of pressure on density for hydrocarbons and carbon dioxide. The vertical axis shows the percent difference in density computed by real-gas and ideal gas models. Reference conditions are STP (273 K and 1 bar) except 550 K and 1 bar for n-heptane.

conditions, respectively.

$$\begin{aligned} P^L &= P^V \\ T^L &= T^V \\ \overline{g}^L &= \overline{g}^V . \end{aligned} \tag{4.15}$$

Figure 4.3 shows the effect of pressure on density in terms of percent difference between real gas and ideal gas models. Figure 4.3 shows that computing density from ideal gas law leads to large errors at high pressures, as expected. The sharp peaks for methane, heptane, and carbon dioxide in Fig. 4.3 are a consequence of phase change not accounted for by the ideal gas law. At temperatures farther away (higher) from the critical point, the errors would decrease because the density decreases at high temperatures (for a given pressure), and hence, the substance approaches towards the ideal gas conditions, i.e., compressibility factor closer to unity. Comparing Fig. 4.2 and Fig. 4.3, one can observe that the pressure has a negligible effect on polarizability but a much greater effect on the density of the pure substance. Thus, accurate density calculations will require a real gas equation of state at high pressures.

4.5.2 Mixtures

The Helmholtz energy equation can be extended to fluid mixtures. Each component of the mixture is linearly combined and weighted by mole fraction to obtain the mixture EOS. For fluid mixtures with negligible inter-molecular interactions between the species, mole weighted additive principle is sufficient. However, a comprehensive treatment of fluid mixtures requires a departure function to account for the intermolecular mixture dynamics. The departure function is determined through regression analysis of available experimental data [61, 62] and is shown in Eq. 4.16 where $\vec{X}$ represents the mole fraction of all species as a vector.

$$f(\tau, \delta, \vec{X}) = \sum_i X_i f_i^{IG}(\tau, \delta) + X_i f_i^R(\tau, \delta) + \Delta f(\tau, \delta, \vec{X}) \tag{4.16}$$

This approach was further improved for binary mixtures in Ref. [12] where the reducing functions, $\tau(x)$ and $\delta(x)$, are determined for the mixture to produce a reduced mixture Helmholtz EOS. The mixture's reduced temperature and density are determined by applying weighting functions to each component's reduced temperature and density and the general functional form is shown in Eq. 4.17

$$Y_r(\boldsymbol{X}) = \sum_{i=1}^{N} x_i^2 Y_{c,i} + \sum_{i=1}^{N-1} \sum_{j=i+1}^{N} 2 x_i x_j \frac{x_i + x_j}{\beta_{Y,ij} x_i + x_j} Y_{ij}. \tag{4.17}$$

Where Y is a function of either density or temperature, β is one of the fitting parameters, and the subscripts r and c refer to the reduced and critical property parameters, respectively. The fitting parameters e.g. β in Eq. 4.17 are obtained by matching the numerical thermodynamic surface to experimental data points for the mixture, namely the bubble and dew points. The binary interaction parameters, and thus, the mixture EOS obtained are only as good as the experimental data upon which they are based [12]. In this study, the software package REFPROP by NIST incorporating the above methodology with features such as a python library for thermodynamic mixture property calculations [63] for a limited number of substances and even a smaller set of binary mixtures has been

used.

4.6 Refractive Index Models

4.6.1 Model Development

The Lorentz-Lorenz Eq. 4.7 was formulated for pure substances, and unfortunately, little research exits to extend it to real gas mixture at high pressures. Nevertheless, Liu et al.provide a detailed summary of different first order mixture laws for refractivity (r_e) neglecting the higher order terms in Eq. 4.10 and the subtleties associated with each one [65]. Mixture laws can be divided into two categories - additive refractivity and additive polarizability. Both are an extension of the Amagat's law whereby the mixture property is calculated as the mole-weighted summation of the component property, i.e., refractivity or polarizability. The general form of the additive refractivity formulation is given in Eq. 4.18.

$$r_{e,mix} = \sum_i r_{e,i} X_i = \sum_i \overline{A}_i \overline{\rho}_i X_i \tag{4.18}$$

In the additive polarizability formulation, the mixture polarizability, $\overline{A}_{mix}$, is calculated from Eq. 4.11a to obtain the mixture refractivity, $r_{e,mix}$, from Eq. 4.19.

$$r_{e,mix} = \overline{\rho}_{mix} \overline{A}_{mix} = \overline{\rho}_{mix} \sum_i \overline{A}_i X_i \tag{4.19}$$

Here, $\overline{\rho}_{mix}$ is the mixture density. These formulations have been used for mixtures of gases and liquids, though with no particular attention to real gas mixtures. In this study, three different models are formulated to calculate the refractivity of gaseous mixture. The first is an ideal gas model while the last two are real-gas models. For the ideal gas model, the two formulations in Eq. 4.18 and Eq. 4.19 are identical.

Ideal Gas (IG) Model

$$\frac{n^2 - 1}{n^2 + 2} = \sum_i \overline{A}_i \overline{\rho}_{i,IG} X_i = \overline{\rho}_{IG,mix} \sum_i \overline{A}_i X_i \tag{4.20a}$$

Real Gas Model 1 - Additive Refractivity (AR)

$$\frac{n^2-1}{n^2+2} = \sum_i \overline{A}_i \overline{\rho}_{i,RG} X_i \tag{4.20b}$$

Real Gas Model 2 - Additive Polarizability (AP)

$$\frac{n^2-1}{n^2+2} = \overline{\rho}_{mix,RG} \sum_i \overline{A}_i X_i \tag{4.20c}$$

In this work, Eqs. 4.20a-c are referred to as the IG, AR, and AP models, respectively. Note that additive refractivity and additive polarizability formulations are different for real gas mixtures. The AR model uses species polarizability at STP and the density of each species is computed from real-fluid EOS as discussed in Section 4.5.1. For AP model, the mixture polarizability is mole-weighted sum of species polarizability at STP, and the mixture density is obtained from real-fluid mixture EOS as discussed in Section 4.5.2.

4.6.2 Model Validation

The above mixture models are compared against experimental refractive index data at high pressures relevant to compression ignition engines. Unfortunately, very limited experimental data exist [10, 24, 48, 49, 108] of which [48] provides the most extensive measurements of refractive index of mixtures for a large range of high pressures. Thus, Ref. [48] will be used to compare the three refractive index mixture models presented above.

In Ref. [48], the refractive index was measured by a Michelson interferometer with a maximum relative uncertainty of 0.03%. The refractive index was measured for binary mixtures of methane and carbon dioxide at pressures ranging from 0.5 to 20 MPa, and a fixed temperature of 303 K. Six different mole fractions of CO_2 were studied: 0%, 50%, 78.2%, 80.2%, 82.2%, and 100%. In our study, the molar polarizability for methane and carbon dioxide is taken from [46]. For each test condition in Ref. [48], the density is calculated by the ideal gas law for the IG model, reduced Helmholtz EOS for each component for the AR model, and reduced Helmholtz EOS for the mixture for the AP model.

Figure 4.4 shows the computed refractive index difference (n-1) for each model compared with experimental data for a binary mixture of 78.2% CO_2 and 21.8% CH_4 at pressures of 1 to 200 bar. For pressures below about 30 bar, all models predict nearly the same linear increase in the refractive index difference with an increase in the pressure. In this regime, the mixture behaves as an ideal gas, thus, the IG model is a valid approximation. Additionally, the AR and AP models are equivalent, and same as the IG model, indicating that each species also behaves as an ideal gas. However, at pressures above 30 bar, the refractive index difference is increasingly under-predicted by the IG model.

The two real gas models provide very different results at pressures above 50 bar: AR model grossly overpredicts while AP model shows excellent agreement with experimental data for the entire pressure range. At high pressures, the compressibility (or real-gas behavior) affects the density significantly but polarizability is nearly constant as shown in Figs. 4.2 and Fig. 4.3. However, the AR model combines both density and polarizability as one "lumped" parameter weighted linearly with the mole fraction. The net effect is a higher (and erroneous) weighting for components with higher density. The non-linear behavior of density is most significant near the critical point and phase boundaries. The experimental data in Fig. 4.4 were obtained at 300 K. The density of carbon dioxide will exhibit highly non-linear behavior near its critical point of 304.4 K and 73.8 bar, which explains the large errors introduced by the AR model at around 70 bar. The error decreases at higher pressures as conditions depart away from the critical point. Note that the test conditions are far above the critical point of methane (190 K and 46.5 bar), i.e., methane would behave close to an ideal gas, and thus, would contribute little to the errors in the AR model. The molecular interactions between species also change the phase transition space of mixtures compared to that of the component species. Thus, the AR model will introduce large errors if any of the component species are near the two-phase region. However, if all of the mixture species are sufficiently far away from the phase boundary and critical point, e.g., in the compressed liquid region or ideal gas region, then the AR model and AP model will give equivalent results. For example, AR type models have been successfully used in liquid mixtures of biodiesel-diesel fuels

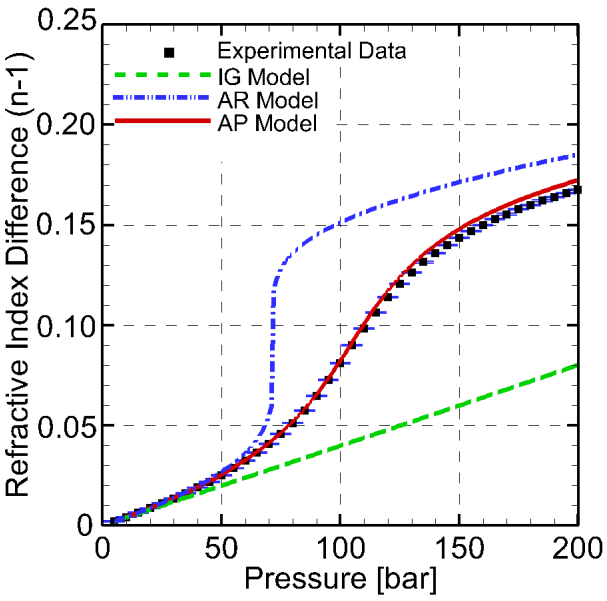

Figure 4.4: Refractive index difference versus pressure for a binary mixture of 78.2% CO_2 21.8% CH_4 at a temperature of 303 K compared with data from Ref. [48].

blends [47].

Based on the above results and discussion, it is clear that if the pressures and/or temperatures of the experiment are near one or more of the constituent fluids phase transition point or critical point, the AP model is the only reliable option among the three models. The AP model uses mixture EOS to compute the mixture density but retains the so-called ideal gas behavior to compute the mixture polarizability to yield accurate results. Figure 4.4 illustrates that (1) computing mixture refractivity as the summation of mole-weighted refractivity of its components or AR model is grossly inaccurate at high pressures, regardless of the method used to compute the density (ideal gas or real gas), and (2) AP model can accurately predict the refractive index for non-polar binary real gas mixtures. Thus, the higher order terms in Eq. 4.11b (B_1, B_2, and B_{12}) are indeed negligible, especially for the CO_2-CH_4 mixture. Considering that CO_2 exhibited the strongest pressure dependence on pure component polarizability in Fig. 4.2 (though still <5% error), the fact that the AP model accurately captures its mixture behavior with CH_4, it is expected that the AP model will work for the other combinations of these non-polar substances. The error could be much smaller if the temperature/pressure are farther away from the critical point of one of the components.

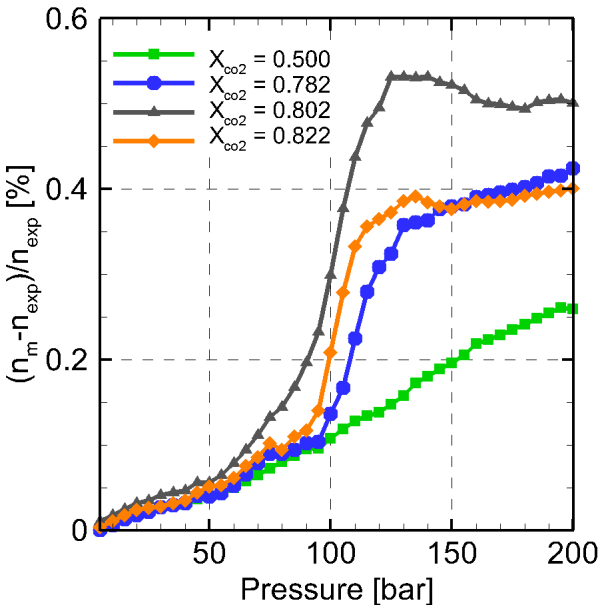

Figure 4.5: Percent difference in predicted (by the AP model) and experimental refractive index data of Ref. [48] at a temperature of 303 [K].

Next, Fig. 4.5 shows comparison of refractive index data for all of the mixtures in Ref [48] with predictions from the AP model. The maximum error is less than 0.6% indicating robustness of the model. The corresponding maximum error in the computed mole fraction is less than 3.5%. In summary, the AP model has been demonstrated to accurately predict the refractive index at high pressures with non-ideal gas behavior. A detailed investigation of the possible sources of errors is beyond the scope of this work. However, minor errors observed in Fig. 4.5 are likely caused by the small effect of pressure on polarizability (see Fig. 4.2) which are ignored in this study.

4.7 Application Examples

In this section, the models developed above will be applied to investigate fuel-air mixing at compression ignition engine conditions assuming adiabatic mixing. First, models will be compared against each other for Spray A condition. Next, AP model will be applied for a wide range of engine conditions.

4.7.1 Adiabatic mixing and phase space

Spray A condition is designed to represent low temperature combustion with moderate exhaust gas recirculation. The fuel for Spray A is n-dodecane - a diesel fuel surrogate -

injected at a pressure of 1500 bar. The fuel (pre-injection) temperature is 363 K, and the ambient pressure and temperature at the test point are 60 bar and 900 K, respectively. Nitrogen is used as the ambient fluid to limit the discussion to binary mixtures. The fuel temperature changes across the injector, and isenthalpic and isothermal conditions across the injector provide the two limiting bounds for the fuel injection temperature. In this study, the fuel injection temperature is obtained by assuming constant enthalpy across the injector, though this choice only affects specific numbers and not any of the trends or conclusions.

Thermodynamic properties of the mixture are determined by assuming adiabatic fuel-air mixing supported by Siebers and others [37, 45, 104, 105]. Adiabatic mixing assumes: (1) local thermodynamic equilibrium with heat transfer occurring only via mass transfer, i.e., no radiation or exothermic reactions, and (2) non-differential transport of all mass, momentum, and energy, i.e., all Schmidt numbers and Lewis numbers are unity. In turbulent flows, the mixing is dominated by turbulent viscosity transport, which is the basis for most CFD simulations. For example, Ref [37] investigated the effect of a realizable Schmidt number in the near nozzle region and found the results were independent of the Schmidt number. CFD studies have found good agreement with experimental centerline mixing measurements using adiabatic mixing assumption [45]. Adiabatic mixing assumption will not work in the sooty flame region or even in cool-flame and ignition regimes associated with exothermic reactions.

The time scale for thermodynamic equilibrium are typically much shorter than heat transfer time scales, and mixing assumption is applied locally (each pixel or grid in CFD) to determine the non-uniform mixing behavior. For adiabatic mixing at a constant chamber pressure, fuel enters as liquid at the fuel injection temperature, the ambient gas is at the chamber temperature, and the exiting fluid can be gaseous, liquid, or two-phase mixture. For a given chamber pressure and temperature, the mixture enthalpy and hence, the thermodynamic state of the mixture including its temperature, quality (if two-phase), mixture fraction, and equivalence ratio can be calculated as a function of the fuel mole fraction.

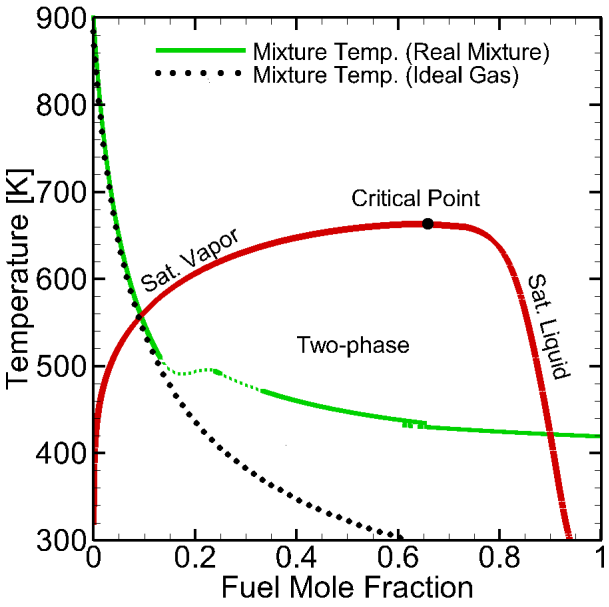

Figure 4.6: Temperature vs fuel mole fraction binary mixture of n-dodecane and nitrogen at Spray A conditions. The phase boundaries and vapor-liquid equilibrium region are also shown.

Figure 4.6 shows mixture temperature versus fuel mole fraction for real gas and ideal gas mixtures. The saturated liquid/vapor lines, two-phase region, and the critical point determined from real-gas EOS for the mixture are also shown. For Spray A fuel injection and ambient conditions, the two-phase mixture occurs at fuel mole fraction of 0.1 (saturated vapor) to 0.9 (saturated liquid). Figure 4.6 shows that the mixture temperature for ideal and real gas assumptions agree with each other for fuel mole fraction of up to 0.15, but depart significantly at higher fuel mole fractions, i.e., for mixtures in the two-phase region. This result is expected since the ideal gas model assumes a vapor phase for the entire fuel mole fraction (or mixture fraction) space. In the two-phase region, the ideal gas model severely underpredicts the mixture temperature as the fuel mole fraction is increased. The dashed green line in the two phase region is a spline fit where REFPROP fails to return a valid solution. Note that the two-phase region cannot be quantified by Rayleigh scattering or RSD diagnostics. Thus, reliable measurements can only be obtained in the vapor region, i.e., for fuel mole fraction of up to 0.10 for this test case. Fortunately, this is not a serious drawback for compression ignition engine applications since fuel mole fraction (or equivalence ratio) measurements are needed mainly in the combustible vapor region.

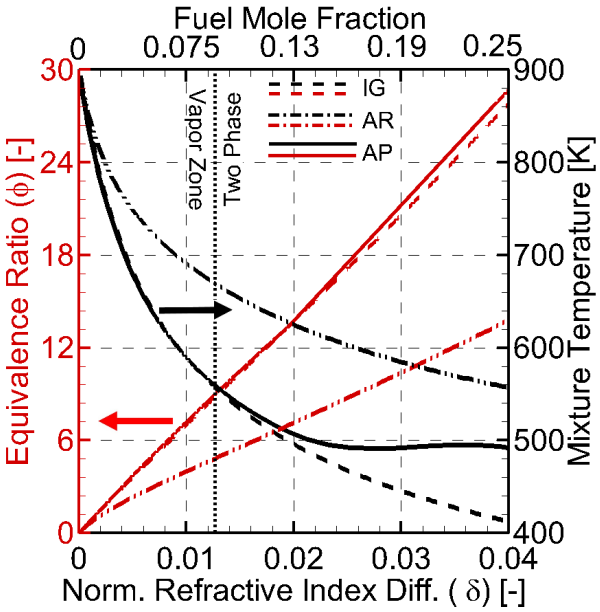

Figure 4.7: Equivalence ratio and mixture temperature as function of normalized refractive index difference for the IG, AR, and AP models.

4.7.2 Model Comparison

In this section, the three models (IG, AR, and AP) will be compared at Spray A condition. Model Eqs. 4.20 will be used to compute the refractive index as a function of fuel mole fraction, which can be related to density, temperature, equivalence ratio, etc. of the mixture. In practice, a look-up table is generated with refractive index as input to determine thermodynamic properties outputs. Figure 4.7 shows the equivalence ratio and mixture temperature for different models as function of the normalized refractive index difference defined as $\delta{=}n/n_0-1$ where n_0 is the refractive index of the surrounding ambient - pure nitrogen in this case. The vapor zone (left side, $\delta < 0.012$) and two-phase zone (right side, $\delta > 0.012$) are identified in the figure.

Figure 4.7 shows that the AR model performs poorly in both vapor and two-phase zones in comparison to the validated AP model. The AR model overpredicts the mixture temperature and slightly underpredicts equivalence ratio even though it uses real-gas properties, again indicating that the additive principle incorporated in the model is grossly inaccurate. This is explained by the chamber conditions being close to the critical point of n-dodecane. The IG model performs well in the vapor zone, but it increasingly deviates from the AP model in the two-phase zone. The large deviation in the two-phase region

is easy to explain since the IG model treats the two-phase zone as ideal gas as discussed previously. Results show that the IG and AP models are equivalent in the vapor zone, indicating that Spray A can be approximated by the ideal gas assumption. However, one should be aware that the phase boundary must be determined either experimentally or from the real-gas analysis. While a detailed uncertainty analysis is outside the scope of this work, uncertainty in δ will propagate to uncertainty in calculated thermodynamic quantities. For example, at Spray A conditions a 1% error in δ corresponds to a maximum of a 1% error in ϕ in the vapor region; where the percent error in ϕ decreases as ϕ increases.

4.7.3 Parametric Study

Next, the IG and AR models are compared with the AP model for a wide range of compression ignition engine conditions: Ambient conditions are varied from an assumed engine intake at P_{intake} =2 bar and T_{intake} =360 K to top dead center (TDC) at P_{TDC} =200 bar and T_{TDC} =1250 K, and the inlet fuel temperature in the chamber is 419 K (after isenthalpically expanding from T_{inj}=363 K and P_{inj}=1500 bar). These conditions represent a typical engine with 2 bar boost at the intake and isentropic compression at compression ratio of 6 to 29 to span the range in compression ignition engines. Figures 4.8 and 4.9 show, respectively, the absolute error in mixture temperature and equivalence ratio introduced by the IG model when compared to the validated AP model.

The y-axes in Figs. 4.8,4.9 represent pairs of chamber (cylinder) pressure and temperature reached via isentropic compression from the initial state. In Fig. 4.8, the right edge of the colored region represents $\phi = 0$ and the left edge is terminated at $\phi = 50$. The dashed white line denotes the phase boundary with vapor on the right and two-phase region on the left side. Figure 4.8 shows that the IG model does quite well in the vapor zone (<5% error). i.e., the IG model is adequate in the vapor zone for most diesel applications. However, one could inadvertently apply the IG model in the two-phase region causing large errors (≈20% error). If the IG model is used, the two-phase boundary must be identified from either real-gas analysis or diagnostics for liquid boundary detection. Such errors can be avoided by applying the AP model throughout the operational regime.

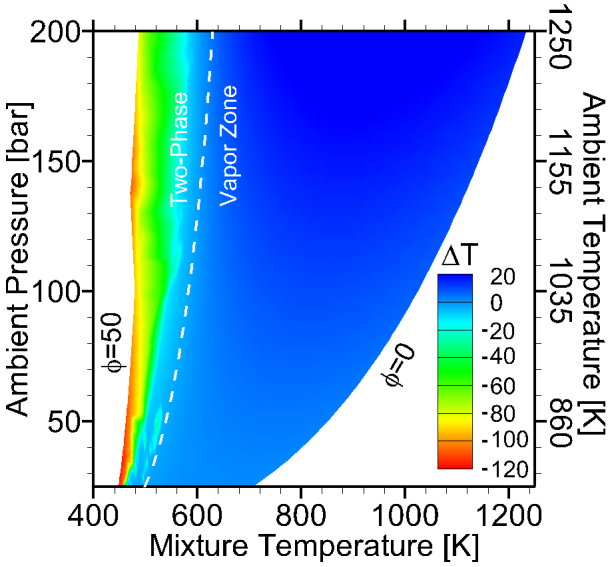

Figure 4.8: Absolute error in the mixture temperature calculated using the IG model (ΔT=T$_{IG}$-T$_{AP}$) for n-dodecane and nitrogen as a function of ambient conditions (pairs for pressure and temperature assuming isentropic compression from P_i=2 bar T_i=360 K). The dashed white line represents the two-phase boundary.

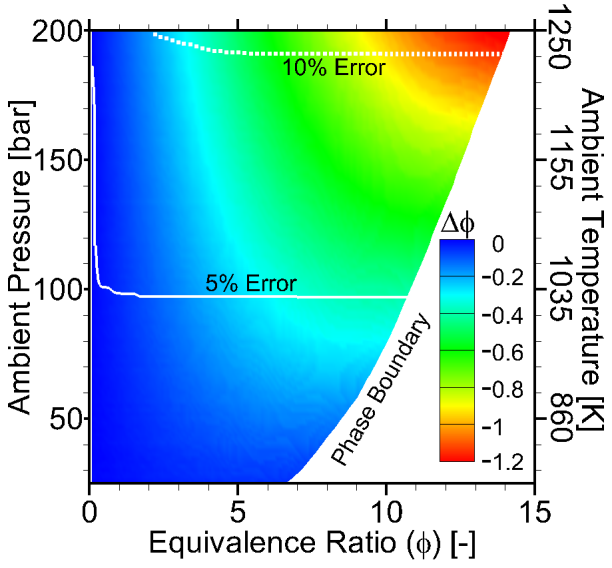

Figure 4.9: Absolute error in the equivalence ratio calculated using the IG model ($\Delta\phi$=ϕ_{IG}-ϕ_{AP}) for n-dodecane and nitrogen as a function of ambient conditions (pairs for pressure and temperature assuming isentropic compression from P_i=2 bar T_i=360K) for gas phase mixtures. The solid and dashed white lines are error isolines of 5% and 10%, respectively.

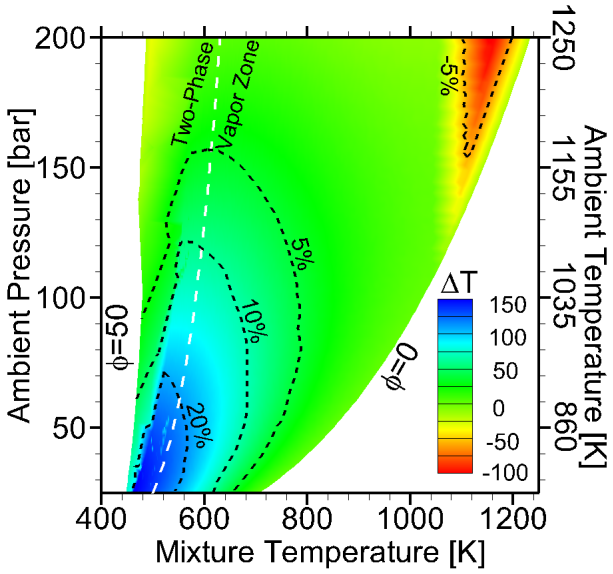

Figure 4.10: Absolute error in the mixture temperature calculated using the AR model (ΔT=T$_{AR}$-T$_{AP}$) for *n*-dodecane and nitrogen as a function of ambient conditions (pairs for pressure and temperature assuming isentropic compression from P_i=2 bar T_i=360K). The dashed white line represents the two-phase boundary and the black dashed lines represent percent error isolines.

Figure 4.9 shows the error in the equivalence ratio introduced by the IG model. The right side of the colored region represents the phase boundary. Figure 4.9 shows that the IG model introduces larger errors at higher compression ratios (or high chamber temperatures and pressures). Figure 4.9 identifies region with errors above 5% (solid white line) and 10 % (dashed white line). However, for pressures below 100 bar, the error in equivalence ratio is small indicating that the IG model is adequate.

Next, Fig. 4.10 shows the error in mixture temperature and equivalence ratio introduced by the AR model as compared to the validated AP model. Even in the vapor zone, the temperature is overpredicted or underpredicted by as much as 150 C. At low chamber pressures (or temperatures), the error is greater near the phase boundary, but at high pressures, it is confined to fuel-lean conditions with significant compressibility effects. Figure 4.11 further supports the poor performance of the AR model. Even in the vapor zone, the errors in equivalence ratio could be up to 80%. As such, the AR model should not be used in optical diagnostics of gas mixtures at high pressures.

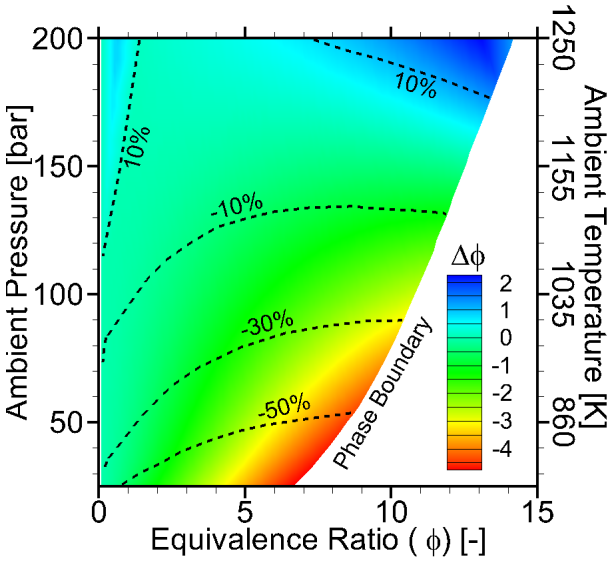

Figure 4.11: Absolute error in equivalence ratio is calculated using the AP and AR model ($\Delta\phi$=ϕ_{AR}-ϕ_{AP}) for n-dodecane and nitrogen as a function of ambient conditions (pairs for pressure and temperature assuming isentropic compression from P_i=2 bar T_i=360K) for gas phase mixtures. The right edge of the contour represents the phase boundary. Percent error isolines are overlaid as black dashed lines.

4.7.4 Supercritical Fuel-Oxidizer Mixing

The AP model will reach its full potential at conditions departing from the ideal gas behavior, e.g., transcritical and supercritical mixing regimes. Recent experimental and theoretical findings have stimulated interest in supercritical fuel-oxidizer mixing at diesel conditions. [25–28, 30, 42, 43]. Thus, the ability to acquire quantitative thermodynamic measurements in the supercritical regime is of great interest. However, purely supercritical mixing in diesel engines requires either much higher ambient pressures (and thus, temperatures) or fuel modifications, e.g., high injection temperature or fuels with low critical temperature. In this study, propane at Spray A conditions is used to simulate supercritical mixing. Figure 4.12 shows that the mixture temperature for propane at supply temperature of 395 K (after isenthalpically expanding from T_{inj} =363 K and P_{inj} =1500 bar), i.e., slightly above its critical temperature of 370 K, injected into an ambient at Spray A conditions (60 bar and 900 K) never enters the two-phase regime and thus completely diffusive mixing without surface tension (or no droplets) is likely to occur. Absence of droplets could potentially allow RSD or Rayleigh scattering measurements

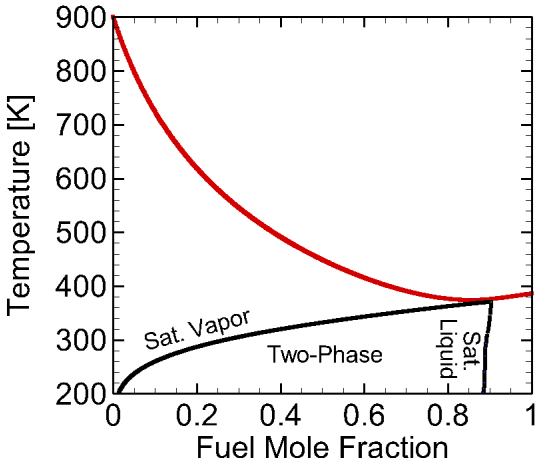

Figure 4.12: Calculated temperature versus fuel mole fraction for binary propane-nitrogen mixture at Spray A conditions using the IG, AR, and AP models.

across the entire mixture fraction space.

Figure 4.13 shows equivalence ratio and mixture temperature versus refractive index difference (or fuel mole fraction) for the three models presented in this study. For refractive index difference, δ, less than 0.01, all three models provide similar results indicating that the mixture is close to an ideal gas. For refractive index difference of 0.02 or fuel mole fraction of 0.5, the mixture temperature is underpredicted by about 25°C by the IG model and overpredicted by about 25°C by the AR model. For fuel mole fraction greater than 0.5 ($\delta > 0.02$), the IG model is no longer useful since it deviates exponentially from the accurate AP model. The AR model is also inaccurate for fuel mole fractions between 0.5 and 0.96. The poor performance of the IG model can be attributed to the significant compressibility effects in this fully supercritical mixing regime. The AR model approaches the AP model at fuel mole fraction close to unity when the mixture approaches a pure substance. However, the AP model would be the method of choice to accurately calculate both mixture temperature and equivalence ratio across the entirety of the mixture fraction space for mixing at purely supercritical conditions.

4.8 Conclusions

This study investigated the effect of pressure on polarizability and density to extend the Lorentz-Lorenz equation to real-gas mixtures at high pressure. Three different for-

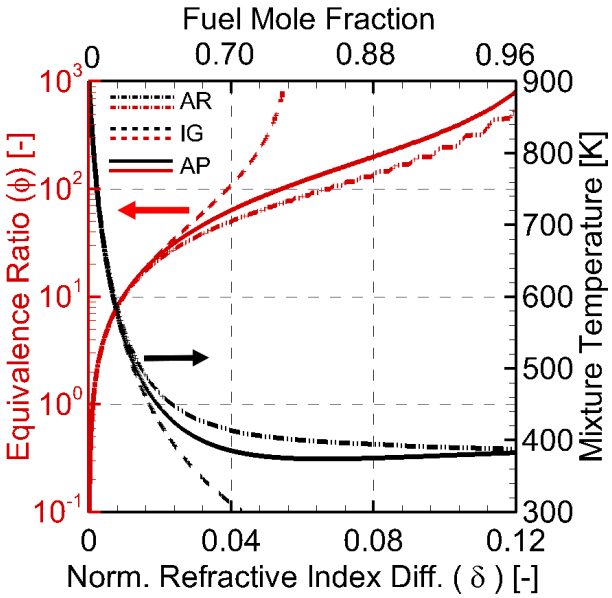

Figure 4.13: Equivalence ratio and mixture temperature as function of normalized refractive index difference for binary propane-nitrogen mixture at Spray A conditions calculated using the IG, AR, and AP models.

mulations of the Lorentz-Lorenz equation for gaseous mixtures were compared against experimental data in the literature. The Additive Polarizability (AP) model was identified as the robust model for applications at the harshest conditions. The AP model was validated using published experimental data on refractive index and then used to estimate errors in the other two models (IG and AR models) for a wide range of compression ignition engine operating conditions. Finally, the AP model was applied to study supercritical mixing of propane and nitrogen. Following is a summary of the conclusions from this study:

- The original Lorentz-Lorenz equation should be used instead of the simplified Dale-Gladstone equation to eliminate unwarranted errors that can affect the thermophysical property calculations.

- For liquids, both polarizability and density are nearly constant. However, for non-polar gases, the polarizability is nearly constant while density varies significantly with pressure. In contrast, density variation with pressure is linear in the ideal-gas regime, but highly non-linear near the critical point and phase change boundaries of component species and mixture.

- Following the additive principle (e.g., Amagat law), the mixture laws for Lorentz-Loretz equation can be expressed as mole weighted sum of component refractivity (product of polarizability and density) or polarizability. For incompressible liquids (constant density) or ideal gases (linear variation in density with pressure), both formulations yield the same result. However, they are different when density varies non-linearly with pressure, for example, near the critical point and/or phase boundaries of components or mixture.

- In the ideal-gas regime, the IG, AR, and AP models are equivalent. In the compressed liquid region where density is linear with mixture fraction, the AR and AP models are equivalent.

- In the non-linear density regime, the IG and AR models can be highly inaccurate. The AR model performs poorly across the entire range of compression ignition conditions, yielding errors in equivalence ratio of up to 80%.

- The AP model works well across the entire compression ignition engine regimes including conditions near the critical point and phase boundaries. The IG model is valid in the vapor region (assuming it is known) at the typical compression ignition engine operating conditions. However, IG model could introduce large errors if inadvertently applied to the two-phase region, for example, in CFD analysis.

4.9 Acknowledgements

This work was performed with support by the Department of Energy, Office of Energy Efficiency and Renewable Energy (EERE) and the Department of Defense, Tank and Automotive Research, Development, and Engineering Center (TARDEC), under Award Number DE-EE0007301.

CHAPTER 5
CONSEQUENCES OF SUPERCRITICAL MIXING AT ENGINE RELEVANT CONDITIONS

5.1 Abstract

This study investigates the prerequisites required to obtain fully supercritical in a diesel-like environment by delving into the thermodynamics of binary mixtures. The theoretical development is then experimentally applied to an optically accessible spray chamber. The experiments conducted in this work consist of injecting 100 injections of supercritical propane into a supercritical and subcritical environment of nitrogen to evaluate the differences between fully supercritical mixing and transcritical mixing. Rainbow schlieren deflectometry is used to quantify global parameters in the jet evolution as well as liquid existence. The results show differences in jet penetration, spreading rate, and jet velocity. The differences are attributed to observed condensation and low density expansion occurring at a microscopic level near the injector.

5.2 Introduction

Diesel engines, gas turbines, and rockets work off the principle of injecting liquid fuel into high pressure, high temperature oxidizer in the combustion chamber. Thermodynamic analysis reveals that increasing the chamber pressure increases the power output and efficiency in diesel engines, and similarly, the specific impulse in rocket engines. Therefore, operating at higher chamber pressures is desirable. One potential result of increased chamber pressure is changing the thermodynamic phase of the injected fuel to a supercritical state. Fuel-oxidizer mixing under supercritical conditions results in different mixing mechanisms (more typical of rockets) than mixing of an evaporating liquid fuel.

These fundamentally different mechanisms result in different mixture conditions that influence the combustion process. Thus, a fundamental understanding of fuel injection in a supercritical environment is needed to optimize and implement high pressure combustion systems.

The emergence of supercritical mixing was first motivated by liquid rocket engines. Mayer *et al.* [70, 71] were one of the first to show experimental evidence in the difference between subcritical and supercritcal mixing in liquid-oxygen hydrogen coaxial jets, where supercritical mixing shows an absence of droplets. A systematic study was performed by Chehroudi *et al.* [21] to determine the jet's visual appearance as a function of reduced pressure,$P_r = P/P_c$, where P_c is the critical pressure. At low P_r, the jet showed surface instabilities which amplified downstream and eventually broke up. As P_r increased, the jet transitioned into secondary breakup where many droplets were formed. At P_r near but below critical pressure, full atomization was inhibited by the large increase in Ohnesorge number (low surface tension) which has a stabilizing effect. At $P_r > 1$ the jet resembled a turbulent gas jet with no visual drops, and the jet growth rate measurements agreed quantitatively with the theory for incompressible but variable density fluids. Segal and others [99,101] performed PLIF experiments to observe changes in the liquid core of FK-5-1-12 injected into nitrogen as chamber pressure was varied and determine that ligaments and liquid parcels tended to decrease and the liquid core shortened as P_r increased.

More recently, supercritical mixing behavior has sparked interest in the diesel engine community. Several experimental and theoretical findings have suggested that the pressure and temperature in modern diesel engines can exceed the thermodynamic supercritical conditions for liquid/gas mixtures in regions of the fuel jet [25–28, 30, 42, 43]. These studies suggest that the existence of such supercritical or transcritical states would challenge the idea of conventional mixture formation in diesel engines. The experimental and theoretical evidence from these works have indicated that conventional diesel sprays exhibit transcritical mixing where the two-phase interface gradually disappears; the interfacial forces do not vanish simply because the critical pressure of the liquid phase is exceeded. Dechoz and Rosé [36] acquired surface tension measurements of diesel, hep-

tane, and gasoline fuel at different temperatures, pressures, and ambient gases. For all the cases surface tension was only slightly reduced as the critical pressure of the pure fluid was exceeded. These well-accepted and frequently cited articles offered much insight as well as prompted additional questions and discussion about the complicated nature of supercritical/transcritical mixing.

While fully supercritical mixing has not been achieved in diesel engines, Boer *et al.* [34] demonstrated supercritical mixing with gasoline in a spark ignition engine by substantially preheating the fuel far above its critical temperature. Detailed combustion measurements showed particulate mass reduction in excess of 50% and particle count reduction of more than 90% in the fully supercritical case. The significant reduction in particulate emissions illustrates the benefits of supercritical mixing in internal combustion (IC) engines. However, the specific mechanism that cause such dramatic improvements in combustion performance are still in question. Also, the necessary steps to achieve supercritical mixing in practical IC engines, namely, diesel engines is unclear from the literature . Providing answers to these questions serves as the motivation of this work.

The objective of this work is twofold: 1) determine the prerequisites to obtain supercritical mixing in a diesel-like environment and 2) investigate the differences in mixing when supercritical fuel is injected into subcritical and supercritical environments at the same density. The injected fuel is supplied at nominally the same conditions for both cases and the ambient density is kept the same. Because the momentum of the injected fuel is the same for both cases, the differences in the global parameters, e.g., jet penetration, cone angle, etc., can be attributed phase change effects. This work is divided into four sections. The first section develops the theoretical tools to realize fully supercritical mixing. Next, the details of the experimental setup are provided followed by the experimental findings. Lastly, conclusions of the study are summarized.

5.3 Theoretical Background

Equations of state (EOS) are used to calculate fluid properties based on easily measured properties such as temperature, pressure, and volume. The most commonly known

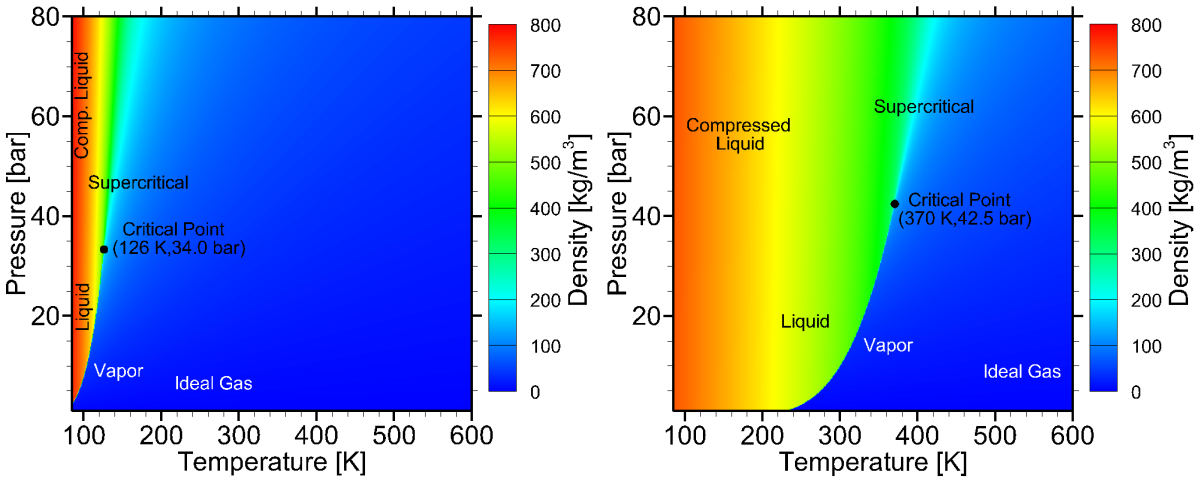

(a) (b)

Figure 5.1: Density contours versus pressure and temperature are shown for (a) nitrogen and (b) propane along the various thermodynamic regimes.

EOS is the ideal gas equation relating pressure, density (or volume and mass/moles) and temperature of a gas, as $P = \overline{\rho}\overline{R}T$. The most useful EOS are semi-empirical or empirical in nature. For reasons of homogeneity, nearly all modern EOS are in the form of Helmholtz energy expressed as a function of temperature and density. A detailed review of the current Helmholtz EOS for pure fluids and mixtures is provided in Chapter 4; the results are utilized in this section for all thermodynamic property calculations.

The data available for mixture EOS is mostly limited to binary mixtures. Thus, to investigate fuel mixing in a diesel environment, nitrogen is recommended in lieu of air, and similarly, diesel fuel is replaced by surrogates such as heptane or dodecane. However, to study the effects of fully supercritical mixing at moderate conditions, a fuel with a lower critical temperature, that is, one much closer to the injection temperature in a diesel engine, is desirable. Thus, the most common hydrocarbon with critical properties that meet this criterion is propane. The experimental challenges with injecting liquid propane are addressed in the next section.

Mixture thermodynamics are best understood with a background in the behavior of individual fluids of interest. Figure 5.1 shows density versus pressure and temperature (P-T) for both nitrogen and propane. These data were computed using REFPROP software [63]. The diagrams shows the different thermodynamic regimes of the two fluids.

The density spans the same range for both fluids, however, the behavior within that range is quite different. The liquid and vapor region are separated by the vapor-liquid equilibrium line, illustrated as a density discontinuity in the P-T space. On this line, saturated vapor, saturated liquid, or two-phase composition can exist. The discontinuity across the two-phase line in the P-T space is much steeper for nitrogen and arises from the smaller, lower polarizability molecule yielding lower intermolecular dispersion forces. The smaller dispersion forces and less available valence electrons also give rise to the higher density in the liquid phase, i.e, the nitrogen must be tightly packed along with a low kinetic energy (lower temperature) before dispersion forces can dominate [66]. Other key thermodynamic regimes are defined accordingly. The compressed liquid regime is defined as pressure being above the critical pressure and subcritical with respect to temperature. The ideal gas regime exists in regions of the P-T space where the temperature is above critical but pressure is not. Finally, the supercritical state is in regions where both the temperature and pressure are above the critical point. For typical engine conditions, the pure phase of nitrogen is clearly an ideal gas, while propane may exit in all phases depending on the injection conditions as described next.

Figure 5.2 shows the P-T phase diagram for a mixture of 80% propane and 20% nitrogen. The saturated liquid and vapor lines for the mixture are illustrated as the dashed and solid red lines, respectively. The vapor-liquid equilibrium lines for pure propane and nitrogen are also shown. Several interesting phenomena occur when mixing two fluids. First, the two-phase region for a mixture is an envelope in the P-T space instead of a simple curve for pure fluids. The saturated liquid line and the saturated vapor line diverge from each other, producing a two-phase region in between. This is caused from species concentration gradients which induce mass based diffusion that results in the dissolution of one substance into another, extending the conditions for two-phase mixture to exist. The divergence of the liquid/vapor lines occurs as soon as a mixture is formed, e.g., 99.9% propane and 0.1% nitrogen. As nitrogen dissolves into propane, molecular interactions between the two species alters the phase transition points in the substance. In this case, nitrogen has a lower critical temperature (126 K) than

propane. Thus, mixing the two substances results in shifting the critical point to a lower temperature.

Note that the critical point of a mixture is defined as the intersection of the saturated vapor line and saturated liquid line in the P-T space, where the quality is undefined. In general, this does not correspond to the highest temperature and/or pressure where phase equilibria can occur. Separate from the definition of the critical point, the highest temperature and pressure where the two phases coexist is referred to as the cricondentherm and cricondenbar, respectively [96]. For pure substances, the critical point is the same as the cricondentherm and cricondenbar points. Figure 5.2 shows the cricondentherm slightly to the right of the critical point and the cricondenbar significantly above the critical point.

Because nitrogen has a lower enthalpy of vaporization than propane for all pressures, the enthalpy of vaporization of nitrogen-propane mixture is lower than that of propane. This results in a visual peeling away action of the saturated vapor line which in turn provides a large vapor region, i.e., the nitrogen-propane mixture can exist as vapor at lower temperatures than the pure propane. Mixture dynamics are even further complicated in ternary or higher number of component mixtures. Thermodynamic properties of mixtures are much more complicated to predict than those of pure fluid because of the numerous ways in which molecules can interact with each other. Generally, mixture thermodynamics are not additive with respect to their pure constituents [96]. This concept is illustrated by considering critical pressure and temperature versus propane mole fraction in Fig. 5.3. Figure 5.3 shows that the critical pressure and critical temperature vary differently for a binary mixture. Furthermore, purely supercritical mixing exceeding the maximum supercritical pressure of 1100 bar in the fuel mole fraction space is virtually impossible in a diesel environment. However, purely supercritical mixing exceeding the supercritical temperature is much more feasible.

The phase behavior for the mixture is more easily understood through the temperature - mole fraction (T-MF) space at constant pressures shown in Fig. 5.4. The lines represent the saturated vapor and saturated liquid lines and the dot refer to the point of

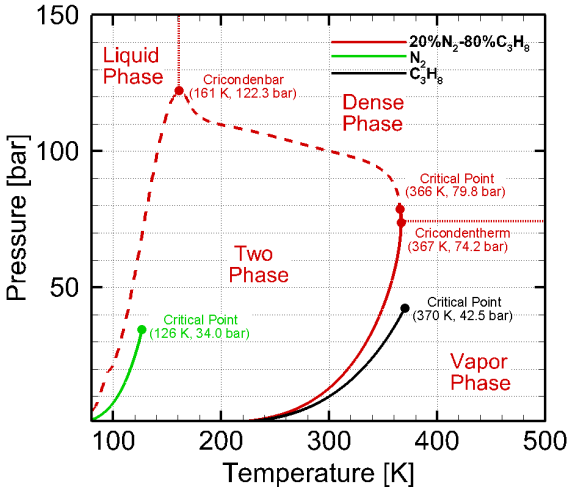

Figure 5.2: Phase diagram of a mixture with 80% propane and 20% nitrogen composition. The dashed and solid red line represents the saturated liquid and vapor lines, respectively. The individual vapor-liquid equilibrium lines are also shown for nitrogen (green) and propane (black)

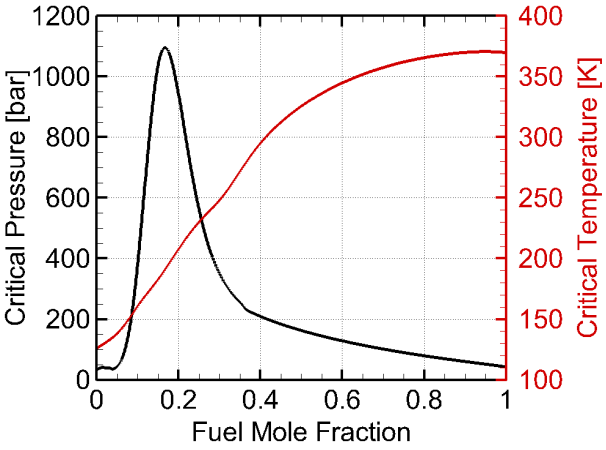

Figure 5.3: Critical pressure (black line) and critical temperature (red line) are plotted versus propane mole fraction.

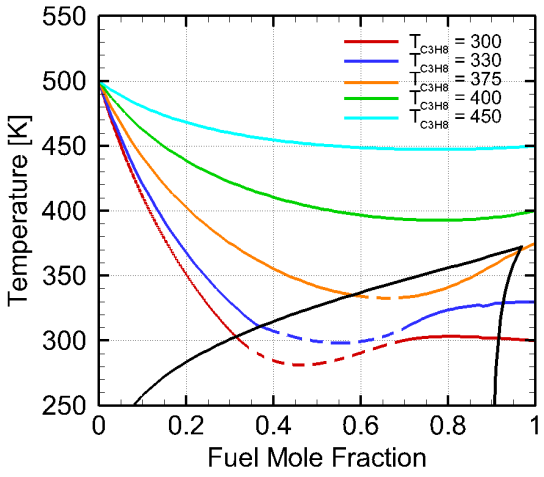

Figure 5.4: Adiabatic mixing lines are shown for propane mixing with nitrogen at 50 bar. The dashed lines represent where REFPROP failed to converge to a solution for the two-phase mixture.

intersection. For pressures below the critical pressure of propane (i.e., 42.5 bar), the dots represent liquid-vapor equilibrium for the pure-propane along its saturation line, e.g., the blue and red dots, whereas the orange dot is the critical pressure for pure propane. At pressure above 42.5 bar, the dots represent the critical point of the mixture for the given isobar. In the T-MF space, two-phase exists inside the enclosed region, whereas liquid and vapor exist to the right and left of the enclosed region, respectively. The mixture is supercritical when it is above the critical point (orange, green, black, and cyan dots) of each isobar. Figure 5.4 clearly illustrates that once the critical pressure is exceeded, the critical temperature increases (orange to green) initially until reaching a maximum, and then it begins to decrease. This trend is also observed in Fig. 5.3. Also, as the pressure increases, the critical point shifts so that the propane-nitrogen mixture can exist as liquid over a wider fuel mole fraction regime. Higher ambient pressures extend the liquid regime and push the two-phase region to a smaller fuel mole fraction region.

In diesel engines, the fuel temperature is generally less than the ambient temperature, and hence, fuel is heated as it mixes with the air. Thus, non-isothermal mixing is investigated at a fixed pressure of 50 bar and various fuel inlet temperatures. Thermodynamic properties for non-isothermal mixing between propane and nitrogen are determined by assuming the same adiabatic (isenthalpic) mixing concepts developed in Chapter 4.

Analysis is performed for fixed pressure and temperature of nitrogen, 50 bar and 500 K, respectively. Propane inlet temperature is varied between 300 and 450 K. Figure 5.5 shows interesting non-monotonic mixing behavior for all propane inlet temperatures. For temperatures below propane's critical temperature, the mixture is heated until it become two-phase when the temperature decreases. Mixtures have a range of two-phase temperatures at a fixed pressure as opposed to pure fluids which have a single two-phase temperature. Throughout the mixture space enthalpy of vaporization continually varies.

Figure 5.5 indicates that at small mole fractions, the propane-nitrogen mixture converts more of its composition to the vapor phase at the expense of the overall energy of the mixture (temperature). Once the quality is sufficiently high, enough energy resides in the vapor state to no longer result in a temperature change (mole fraction around 0.5). After this point, the enthalpy of vaporization is sufficiently low so that energy addition from the hot nitrogen results in a temperature rise. Interestingly, Fig. 5.5 shows a substantial decrease in the mixture temperature for 375 K propane line. Pure propane at this temperature is a supercritical fluid. However, when introducing nitrogen (lower density) the overall mixture density is reduced. The expansion has a cooling effect as shown in Figure 5.5. Similar behavior occurs at higher pressure. The temperature change is reduced because the density of the higher temperature propane is lower, resulting in a less dramatic mixture density change. Figure 5.5 shows that it is not enough to be slightly above the critical temperature of the pure fluid in order for supercritical mixing to occur.

Each of the lines in Fig 5.5 can be represented by a single value on a contour map illustrating if supercritical continuous mixing has occurred or if two-phase formed somewhere in the mixture space, i.e., if the adiabatic mixing occurs above the dome. Figure 4.6 shows the results of adiabatic mixing of propane at different inlet temperatures (300 to 500 K) and nitrogen at 500 K at various pressure (10 bar to 100 bar). This contour map collapses all of the previous analysis to a simple binary plot. Interestingly, the two-phase cutoff point for the mixing space initially corresponds with the liquid-vapor equilibrium line for pure propane. The significance of this is that if propane is initially a vapor, it

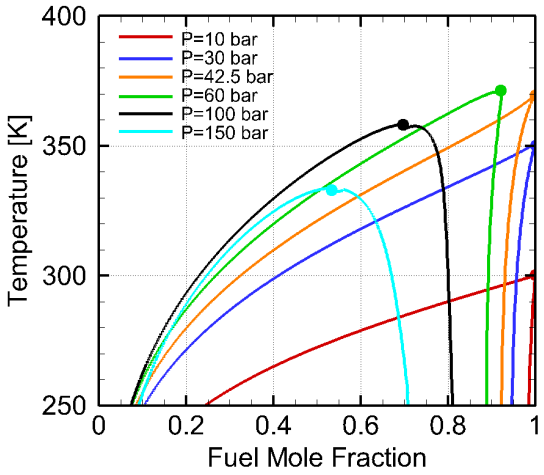

Figure 5.5: Liquid-vapor equilibria is shown with respect to temperature and propane mole fraction. The dots represent the intersection of the saturated liquid and vapor lines.

will stay above the two-phase dome and follow continuous phase mixing. It also reveals continuous phase mixing can occur in two different fashions: 1) propane can enter as vapor and stay above the two-phase dome or 2) propane can enter as a supercritical fluid and stay above the dome. From a thermodynamic standpoint, the only difference between these two phenomena is density. The latter is of more significance for diesel engines in that vapor injection through a traditional diesel injector is problematic. Thus, only points above propane's critical point are viable from fuel injection standpoint. The analysis moving forward will thus consider an ambient pressure of 50 bar.

The results from Fig. 4.6 reveal important considerations for enabling a fully supercritical mixing process, however, in order to apply these results to an actual diesel injection system and engine environment, information is needed about the state of the fuel through the injector. A typical throttling process can be considered isenthalpic. For diesel injection processes however, due to the large pressure drops across the injector, a large change in the kinetic energy invalidates this assumption. At the other extreme, the fuel injection is not necessarily isothermal. Thus, the injection process is approximated as isenthalpic, although a more accurate approach would include the change in the kinetic energy. Figure 5.7 shows the temperature-density phase space for pure propane where the two-phase dome is outlined by the saturation lines (black lines) along with two iso-

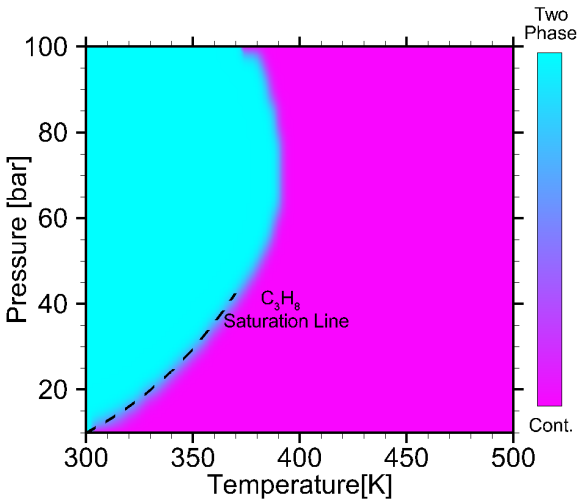

Figure 5.6: A binary contour map is shown delineating fully continuous phase mixing versus the occurrence two-phase throughout the adiabatic mixing space. Nitrogen is kept at 500 K while propane inlet temperature is varied along with the ambient pressure.

bars: one at a typical diesel injection pressure of 1500 bar (orange line) and a second at a chamber environment of 50 bar (blue line). This phase space shows two different pathways as the propane travels from the injector sac at 400 K to the inlet of the chamber. The isenthalpic pathway and the pathway including kinetic energy are shown as green dashed and purple dashed line, respectively. Kinetic energy is estimated using Bernoulli's equation and a discharge coefficient of 0.86 recommended for Bosch common-rail injectors [89]. The incompressible assumption used to estimate velocity provides a first order approximation. While it is not completely accurate, trends can still be observed.

The first observation to be noted is that both isenthalpic and an included kinetic energy pathway are far from isothermal. The isenthalpic pathway has an initial rise in temperature before reaching a maximum, and then decreasing about 387 at the chamber inlet. The initial increase in temperature is due to the relatively low compressibility of propane at 1500 bar. Enthalpy ($h = u + PV$) in this process is constant, and because volume is not changing as much as pressure is in this region, internal energy must decrease to compensate - causing an increase in temperature. Once propane's compressibility becomes significant then volume changes more than pressure causing internal energy to decrease; thus lowering the temperature. The kinetic energy pathway has very different behavior. As pressure drop first occurs, the fluid is nearly incompressible resulting in a

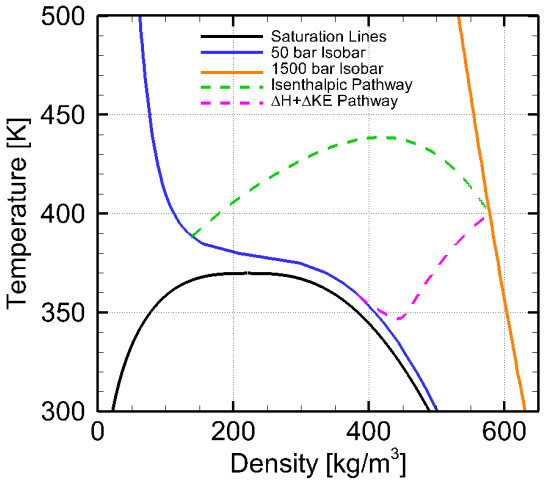

Figure 5.7

change in kinetic energy that is twice that of the change in pressure in Eq. 5.1.

$$\Delta u + \frac{1}{\rho}\Delta P + P\Delta\frac{1}{\rho} + \Delta ke = 0, \quad \Delta ke = 2\frac{\Delta P}{\rho} \tag{5.1}$$

Internal energy compensates by decreasing to satisfy conservation of energy. This occurs until the compressibility effect are non-negligible around $450\frac{kg}{m^3}$ where the change in density is the dominate term and internal energy must increase to balance the equation. The results is a final inlet temperature of 359 K.

The simple analysis shown in Fig. 5.7 clearly outlines the importance of properly accounting for the injector state when attempting to define initial conditions for such an experiment. Results demonstrate that at this high injection pressure, even a fuel injection temperature of 400 K would not be sufficient to achieve fully supercritical mixing. Also, the uncertainty of the inlet fuel temperature increases with injection pressure. To further investigate the effects of injection temperature and pressure, the same analysis for binarizing two-phase versus continuous mixing is utilized next.

Figure 5.8 shows the binarized contour analysis for propane injecting into an environment of nitrogen at 500 K and 50 bar at various injection pressures and temperatures for an isenthalpic process (Fig. 5.8a) and considering kinetic energy (Fig. 5.8b). Two important conclusions can be made from this analysis. 1) Low injection pressures approximate

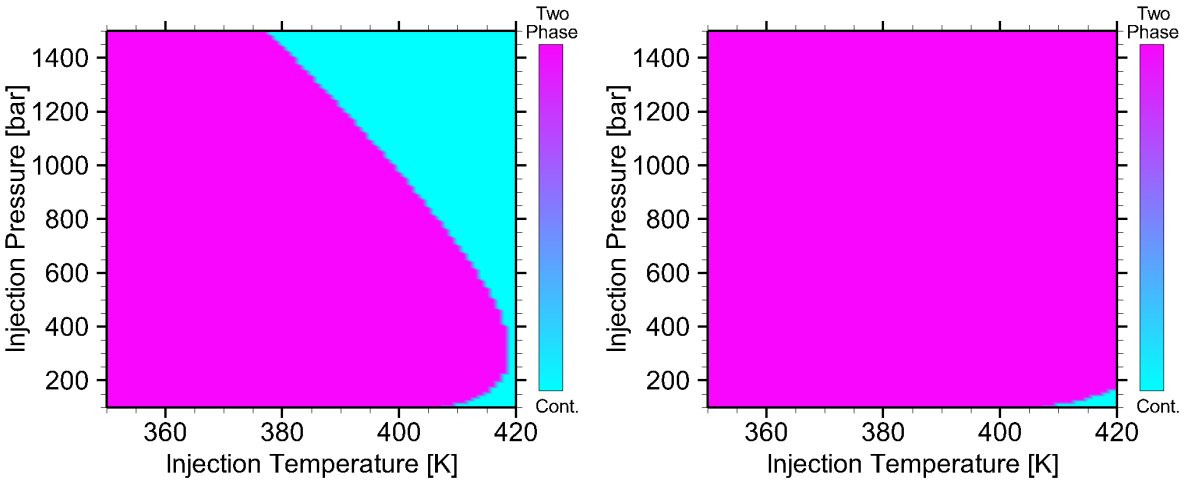

Figure 5.8: A binary contour map is shown delineating fully continuous phase mixing versus the occurrence two-phase of propane injected into an environment of nitrogen at 50 bar and 500 K. The adiabatic mixing space is a function of the injection pressure and temperature where the injection state is modelled as (a) isenthalpic and (b) accounting for kinetic energy.

an isenthalpic process and therefore are a more viable option to achieve supercritical mixing. Another beneficial consequence of using a low injection pressure is the increased validity of equilibrium thermodynamics and adiabatic mixing promoted by much slower jet velocities and much longer mixing timescales. 2) The fuel needs to be pre-heated to at least 410 K - 40° higher than propane's critical temperature (T/T_c=1.1) - if the process is fully isenthalpic.

Experimental results shown in Section 5.5 demonstrate that an injection pressure of 190 bar - the lowest functional injection pressure realized for the commonrail injector - gives inlet velocities less than 10 $\frac{m}{s}$. This velocity corresponds to negligible kinetic energy effects compared to the pressure drops and density changes through the nozzle and thus it is more reasonable to assume that the process for this particular injection pressure is isenthalpic as the fuel flows through the injector nozzle. At this pressure, the injection temperature required for fully supercritical mixing according to isenthalpic analysis is 417 K. A secondary case of transcritical mixing (initially supercritical at injector exit, followed by mixing induced condensation) is determined from the same analysis. To maintain momentum continuity between a transcritical mixing case and a supercritical mixing

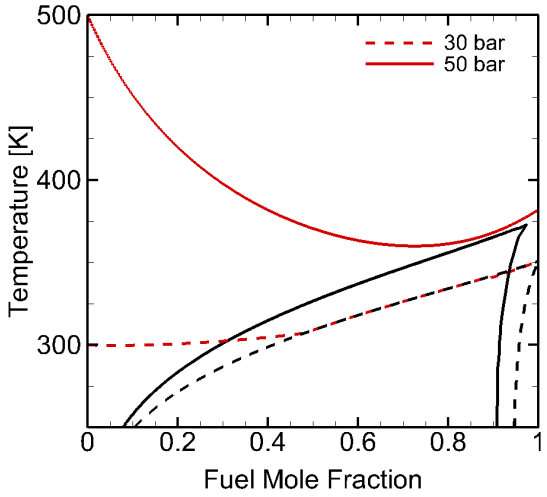

Figure 5.9: Adiabatic mixing lines (red lines) are show for an ambient pressure and temperature of (a) 50 bar and 500 K and (b) 30 bar and 300 K. Both cases start at the same injector conditions (190 bar and 417 K). The saturation lines for each case are shown in black.

case, the ambient density and injector conditions should be kept constant. Momentum continuity in the boundary conditions would suggest that mixing differences are driven by thermodynamic phase change effects. The two ambient conditions that provide this contrast is 1) $P_{amb} = 50$, $T_{amb} = 500K$ and 2) $P_{amb} = 30$, $T_{amb} = 300K$. The results are shown from adiabatic mixing are shown in Fig. 5.9. Both cases start at the same injection pressure (190 bar) and temperature (417 K). The 50 bar case gives continuous mixing, whereas the 30 bar case dips in the dome. These results provide a baseline for comparing transcritical versus supercritical mixing in an experimental system.

5.4 Experimental Setup

5.4.1 Constant Pressure Flow Rig (CPFR)

Figure 5.10 illustrates the test apparatus used in this study. A constant pressure flow rig (CPFR) with vertical continuous flow is designed to provide line-of-sight optical access of fuel injection into an ideally nearly quiescent environment to generate large datasets (>100 injections) in about an hour. The experimental facilities are capable of supplying the chamber with bottled high pressure nitrogen while air from an upstream compressor is used to warm up the chamber. Prior to entering the chamber the pressurized gas is

electrically preheated (up to 1100 K). The supply mass flow rate required by the heater is 2 aCFM. For the cases in this study, the given mass flow rate corresponds to average speed of approximately <0.01 m/s (low temperature case) and 0.1 m/s (high temperature case) in a counter-flow arrangement shown in Fig. 5.10. The counter-flow gas enters through a flow conditioner consisting of six 0.5 mm thick, 100 micron mesh elements followed by a diffuser section to uniformly distribute the flow across the CPFR. The gas exits at the top of the rig through four 3 mm diameter holes placed symmetrically in an annulus around the injector cooling jacket. The ambient gas supply pressure is controlled by an upstream dome regulator and the gas flow rate is regulated by a downstream control valve. Table 5.1 shows the test conditions recorded during the experiment. The available facilities limited the maximum operating pressure to 50 bar, which remains below typical compression ignition engine cylinder conditions during injection (as well as ECN Spray A test conditions) at this time.

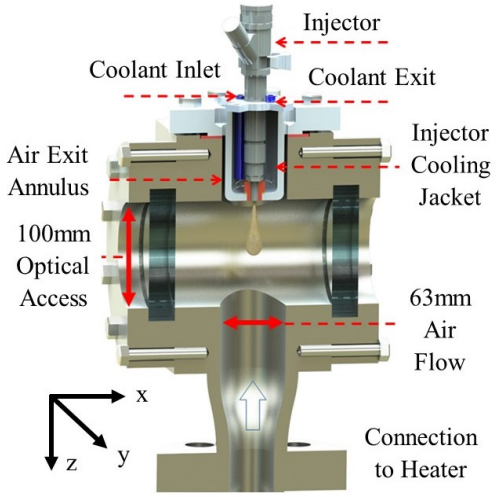

Figure 5.10: Constant pressure flow rig (CPFR) illustration.

Fuel is injected by a Bosch CRIN3-18 injector modified to have a single 100 μm hole at the tip to create a spray along the axis of the rig. The fuel temperature is assumed to be that of the injector body which was maintained at an average of 402 °C by a surrounding temperature controlled coolant jacket; this temperature is the maximum operating temperature of the Bosch injector above which apparent thermal expansion within the injector body results in no injection when triggered regardless of injection pressure. The

Table 5.1: **Air flow and fuel injection conditions for the CPFR along with camera acquisition rates.**

Case	Amb. Temp. (K)	Amb. Pres. (bar)	Spatial Res. ($\frac{\mu m}{px}$)	Framing Rate (kHz)	Cam. Exp. Time (μs)
1	300	30	38	60	16.7
2	500	50	38	60	16.7
3	300	30	8	10	100
4	500	50	8	10	100

coolant jacket temperature is feedback controlled by an externally heated coolant reservoir that uses the two thermocouples on the inlet and exit of the injector jacket thermocouple. The injector pressure is controlled by a pneumatic pressure multiplying fuel cart with a 300 to 1 pressure ratio. The fuel cart is capable of conventional liquid fuels as well as unorthodox fuels such as propane, which is gaseous at ambient conditions. For fuels that would be gaseous at room conditions, a back pressure nitrogen tank is used to pressurize and liquefy the fuel, and thus, enable it to be pumped through the system. The modifications allow for propane injections up to 1500 bar. However, the injection pressure in this study is 190 bar - the lowest realizable injection pressure for the injector - as per the recommendations in the previous section.

The experiment begins by heating the chamber with air to the desired temperature. The preheat time is determined by the set temperature. For examples, steady state conditions at 500 K (near injector temperature) occur in approximately 2.5 hours. Steady state operation is defined by minimizing the ΔT between the near injector and chamber wall temperature, e.g., at 500 K $\pm$ $\approx$15. After reaching steady state conditions, the supply gas is switched from air to nitrogen - the ambient gas during data acquisition. A wait time of 5-10 minutes was used to ensure adequate purging of any remaining air. Once nitrogen is flowing through the chamber, the fuel cart is enabled pressurizing the injector to the set pressure of 190 bar and data acquisition ensues.

5.4.2 Optical Diagnostics

Measurements are obtained by the RSD system shown in Fig. 5.11 to visualize the fuel-air mixing inside the CPFR. An Energetiq EQ-99X fiber coupled broadband light source is collected and focused onto a 3 mm x 150 μm rectangular aperture placed at

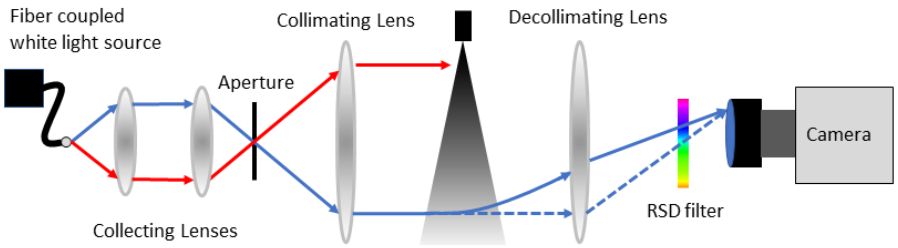

Figure 5.11: Illustration of the RSD system.

the focal point of a 75 mm diameter, 250 mm focal length achromatic doublet lens. The collimated light enters the left and exits the right window of the CPFR. As light rays propagate through the test media, they either become deflected by density gradients (blue line), scattered by the presence of liquid droplets (red line), or absorbed by the dense fluid (also red line). After exiting, it is decollimated by a matching achromatic doublet lens. The light rays are focused onto a 5 mm asymmetric filter with a hue range of 20° to 340° placed at the focal point of the decollimating lens. The color filter color codes the images that are acquired by a Photron Nova S9 color camera. The camera is outfitted with two different lens setups in this study. The first provides a full field visualization of the fuel injection using a Nikon AF FX DC-NIKKOR 135 mm lens to provide a spatial resolution of 38 μm per pixel. The second provides a zoomed-in near field visualization using a long range microscopy system. A Nikon AF-S NIKKOR 300 mm coupled with a designed extension tube arrangement (470 mm of extension tubes) to focus at the injector plane with a spatial resolution of 8 μm per pixel. The imaging parameters for the cases in this study are provided in Table 5.1.

5.5 Results

The theoretical analysis developed in this work provided the target experimental conditions for this study. However, due to experimental limitations, the maximum pre-injection temperature is 402 K. At injector temperature much higher than this, the Bosch injector becomes unreliable. It is worth noting that a pre-injection temperature 417 K and 402 K correspond to a post injection temperature of 381 K and 378 K, respectively,

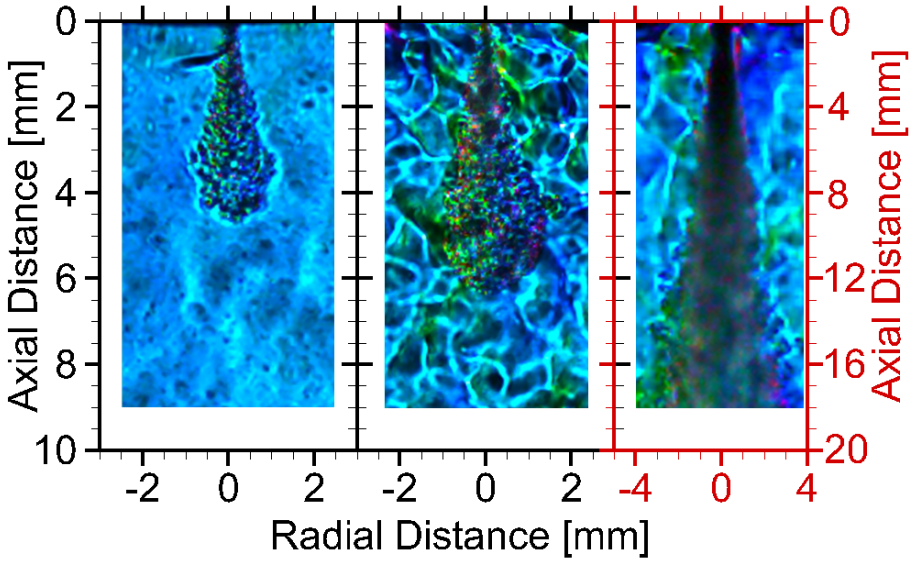

Figure 5.12: A sample raw RSD image is shown for a propane injected at 190 bar, 402 K into a (left) 30 bar, 300 K and (middle) 50 bar, 500 K ambient environment. The right image illustrates a high injection pressure of 1500 bar and 402 K into 50 bar, 500 K bar ambient environment. All images are at 4.58 ms ASOI.

through isenthalpic analysis - a 3 K difference. This analysis does not include any heat transfer effects from the hot ambient chamber of 500 K heating the outside of the injector body. Conduction effects will occur as the propane travels through the injector body, perhaps heating the fuel 3 or more degrees. Regardless, a 3 degree difference at the inlet is the difference between the adiabatic mixing line having a slight gap between the two-phase dome and briefly touching the saturated vapor line. The experimental evidence presented next suggests that the 402 K injection temperature is sufficient for continuous phase mixing.

Figure 5.12 shows farfield raw RSD images for a sample injection at 4.58 ASOI for (left) case 1, (middle) case 2, and reference high pressure injection at 1500 bar into the 50 bar environment. Note the axis for the reference high pressure case is scaled twice that of the others. A lower spatial resolution ($90\frac{\mu m}{px}$) was used to accommodate the larger expansion of the jet. The high pressure injection image provides visual evidence of light scattering due to a large liquid core/droplet region near the injector as described in Chapter 3. This liquid region (0-6 mm) appears black in the image. Figure 5.12 illustrates that case 1 and case 2 are distinctly different than the high pressure reference case. There

seems to not be direct evidence of light scattering from liquid droplets at this resolution for case 1 or 2, i.e., the signal intensity near the injector is on the order of the background intensity. The absence of significant light scattering in fully supercritical mixing was also observed in [34]. Although both cases do not show clear evidence of liquid formation, there are discrepancies in penetration distance (about 1.5 mm) between the 30 bar and 50 bar case. Recalling that the boundary conditions (injection pressure/temperature and ambient density) are the same for both cases, these clear differences support the hypothesis that thermodynamic phases differences are causing mixing deviations that affect the jet penetration processes. Also, Fig. 5.12 shows how the increased counter-flow required by the heater in the supercritical environment causes a much noisier background than the subcritical environment. Some of the background structures have density gradients on the order of the signal. The implications of this will be considered further in discussion to follow.

More quantitative results are generated using the analysis in Chapter 3 to determine the average jet tip penetration based on all 100 injections acquired during the experiment. The results are plotted in Fig. 5.13 for both the case 1 (subcritical environment) and case 2 (supercritical environment). Figure 5.13 depicts how the noisier background present in the supercritical environment causes higher levels of noise in the jet penetration. The noisy background further present challenges in algorithmically detecting the jet tip in the initial evolution (t<1.3 ms) and thus, the data is excluded in this region. Nevertheless, a clear trend is observed whereby the jet injected into the supercritical environment diverges from the subcritical environment around 2 ms ASOI. By the end of the injection, the jet injected into the supercritical environment has penetration about 0.7 mm longer than the jet in the subcritical environment (≈10% longer). The green dashed line for both cases represent a curve fit based on an equation used for spray tip penetration from Ref. [80], where velocity initially follows a constant trajectory with time followed by power law scaling.

However, jet penetration does not account for the greater counter-flow present in the supercritical ambient case. Therefore, jet velocity is determined by differentiating

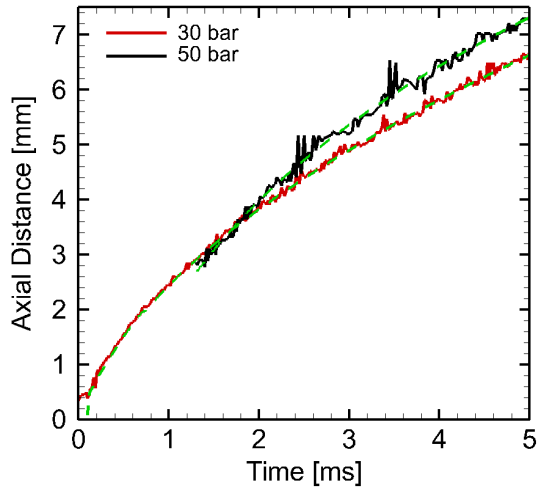

Figure 5.13: The average jet penetration is shown versus injection duration for 30 bar (red line) and 50 bar (black line) along with a curve fit (green-dashed line) based on the analytical jet penetrations profiles from Ref. [80].

the curve fit data and including the average counter-flow bulk velocity. Figure 5.14 shows velocity versus time (Fig. 5.14a) and versus distance (5.14b) for the two cases. Figure 5.14a illustrates that velocity is greater at all times where data is available. The implication of a greater velocity and equal jet penetration behavior observed at $t = 1.4\,\text{ms}$ in Fig. 5.13 is average SOI for the supercritical ambient cases is delayed. This is perhaps due to the higher ambient pressure in the supercritical case inhibiting the initial flow when the needle first opens, i.e., a lower pressure drop across the injector. To account for the possible mismatch in average SOI, velocity is plotted verse distance in Fig. 5.14b. The results show that the supercritical ambient environment where fully supercritical mixing is potentially occurring provides approximately a 50% increase in jet velocity for nearly all distances to the subcritical ambient counterpart; despite a lower pressure drop across the injector.

The significant velocity differences are hypothesized to result from phase change differences between the two cases. Roy *et al.* [98] has also conducted similar experiments in which a supercritical jet is injected into a sub- and supercritical environment. They observed the subcritical environment to cause local subcritical conditions where reassertion of surface tension occurs producing a formation of droplets. In order to observe if droplet formation is occurring, the spatial resolution is enhanced by over a factor of 4

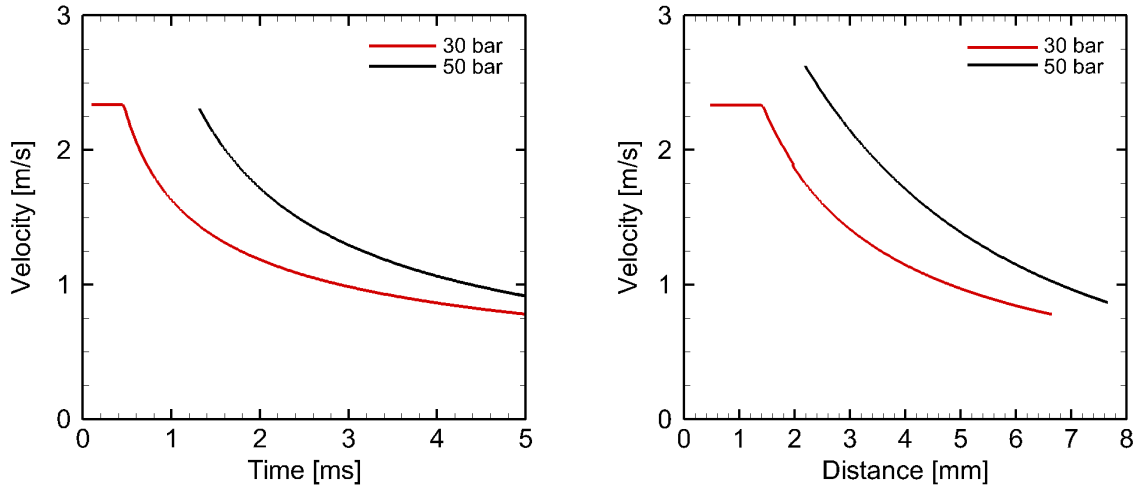

(a) (b)

Figure 5.14: Average jet velocity is plotted versus (a) time and (b) distance for 30 bar (red line) and 50 bar (black line).

using an in-house designed long range microscopy system. The details are provided in the experimental setup.

Figure 5.15 shows an instantaneous nearfield RSD image at 3.2 ms ASOI at a spatial resolution of $8\frac{\mu m}{px}$, that is, around 12 to 13 pixels across the injector hole. This frame is where the supercritical ambient case penetrates to the edge of the field of view. Figure 5.15 shows how the injector is slightly (≈ 10 μ m) recessed into the cooling jacket to help protect from overheating, and thus, the injector tip cannot fully be observed. Also, Fig. 5.15 illustrates the that the greater counter-flow velocity and greater background density gradients amplify diffraction effects near the injector, likely due to local cooling from injector cooling jacket, thus interfering with the signal at this location. However, the subcritical ambient case provides a cleaner signal present near the injector. First, it is worth noting that the longer jet penetration (>1 mm) is also observed in the near field. Figure 5.15 clearly shows that at this spatial resolution liquid formation is observed along the shear layer of the subcritical ambient environment, confirming observations in Ref. [98]. Observing dark regions caused by liquid surface scattering along the edge of the jet in a line of sight technique implies that liquid is forming along the cone of the jet. However, due to either small droplet sizes and/or the low droplet density complete light occlusion only occurs where the optical thickness is the greatest, i.e., along the 2-D jet

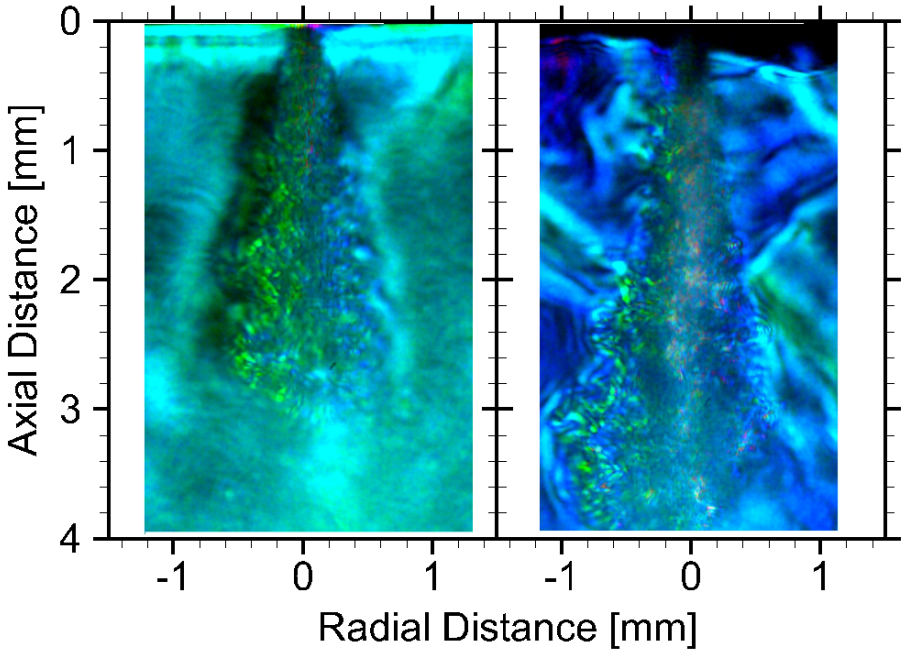

Figure 5.15: The near field is visualized using RSD for a sample propane injection into a (a) 30 bar, 300 K and (b) 50 bar, 500 K ambient environment at 3.2 ms ASOI.

periphery. Note that even a resolution of $8\frac{\mu m}{px}$ is not enough to detect individual droplet formation. Droplet sizes at these conditions are extremely small. The supercritical ambient case shows no sign of liquid formation, indicating that fully supercritical mixing is likely occurring. Only close to the injector (<0.5 mm) is dark. However, it is unclear if this darkness is a result of diffraction effects or absorption from the dense fluid - also observed in initial supercritical mixture in Ref. [34]. It is unlikely that liquid is forming in the supercritical environment near the injector because the signal in the subcritical ambient case is mostly translucent at an axial distance less than 0.5 mm. If the subcritical environment promotes supercritical, mostly translucent behavior at the nozzle exit it is reasonable to assume that a higher pressure and temperature ambient case would provide an even more supercritical tendency. Also, as propane initially emerges from the injector it is a pure fluid, and from the aforementioned theory, pure fluids above the critical point are supercritical.

Next, liquid existence on a probabilistic basis (out of 100 injections) is determined following the methodology presented in Chapter 3. Figure 5.16 shows the liquid probability for both cases along with the jet boundary detected by the hue signal as described

in Chapter 3. Figure 5.16 confirms that liquid formation is occurring along the shear layer. The initially supercritical propane jet shows appears to be experiencing retrograde condensation as it mixes with the subcritical ambient. The asymmetry is most likely caused from local uneven temperature distributions in the counter-flow coupled with re-circulation. Also, both the liquid probability contour and the average jet boundary show bell-like expansion after the initial emergence of the supercritical jet. The ambient conditions promote low density vapor phase formation. Thus, the high density from the supercritical jet begins to undergo a density related expansion. This microscopic phenomenon is not captured for the coarser spatial resolution case. The average jet boundary at the tip of the jet is curve fit through data points represented by the dashed line. The liquid detection algorithm has detection issues in this near nozzle region due to density gradients at the jet head being on the order of the background (similar hue in raw images).

The supercritical ambient case reveals vastly different behavior. First, the same initial jet emergence present in both cases begin to expand linearly around 0.5 mm downstream. This linear growth rate is consistent with the linear growth rates observed for supercritical jets [21], that is, supercritical jet follow the same jet growth rate of variable density gas jets as described in Chapter 2. Secondly, besides the injector exit, there is no detected presence of liquid. Again, it is worth noting that the algorithm detects liquid as sufficiently attenuated light signals [115]. Thus, from the theory that the propane emerges as a purely supercritical jet, and the fact that the subcritical ambient density shows less "liquid" behavior near the injector it is reasonable that the detected "liquid" in the supercritical ambient case is from attenuation from diffraction effects or significant absorption from the supercritical fluid.

Next, the average jet spreading angle for 3.2 ms ASOI is shown in Fig. 5.17 for both cases. Figure 5.17 shows an initial decrease in the emerging jet angle for both cases. After the initial decrease the two cases shown different behavior. The supercritical ambient cases show a nominally constant angle, whereas the subcritical ambient case reveals a increase from 0.7 mm to 1 mm then a decrease - bell-like expansion. This is due to the density related expansion from ambient conditions promote low density vapor formation.

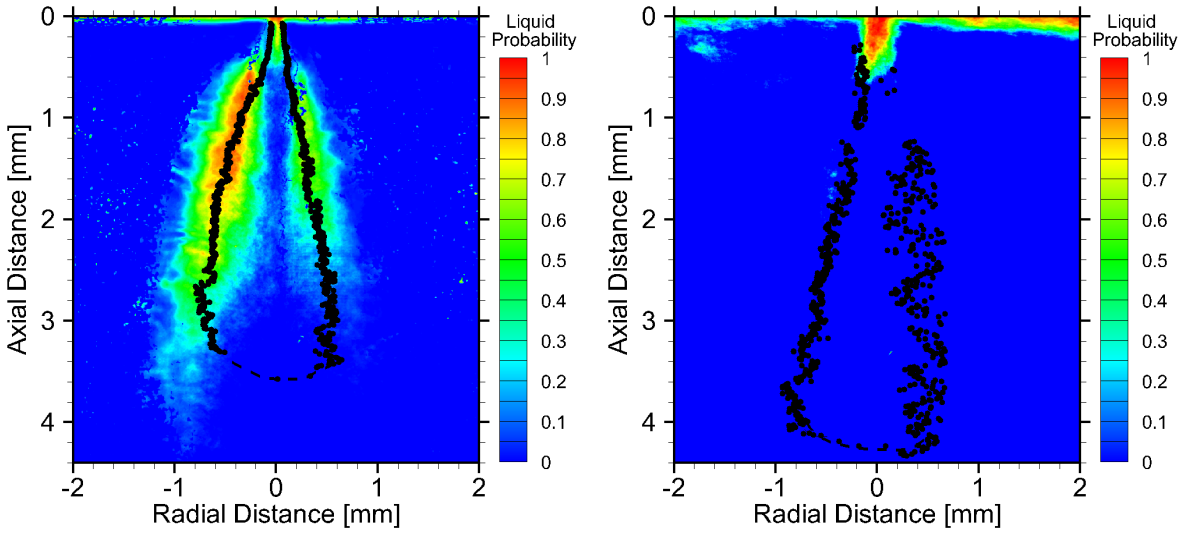

(a) (b)

Figure 5.16: Liquid probability contour maps are shown for the (a) 30 bar case and (b) the 50 bar case at 3.2 ms ASOI.

Figure 5.17 provides useful quantitative information to explain the qualitative trends previously observed.

5.6 Conclusions

The complex thermodynamics of real-fluid mixing that govern fully supercritical mixing at diesel-like conditions was investigated. The analysis was performed on a binary mixture of propane and nitrogen. The theoretical results suggest that fully supercritical mixing only exists when the fuel is injected at relatively low injection pressures ($<$ 200 bar) and at injection temperature greater than propane's reduced temperature (T_r=T/T_c) of 1.1 into a supercritical ambient environment much hotter than the fuel. These perquisites combat the two main obstacles that hinder supercritical mixing. The first obstacle is the significant temperature drop that occurs across the injector due to large pressure drops, density changes, and velocity changes. The second is the cooling effect that occurs when the initial dense propane mixes with nitrogen creating a less dense supercritical mixture that leads to expansion relating cooling. This cooling effect occurs even when the ambient (500 K) is much hotter than the initial propane (375-450 K).

These theoretical guidelines were applied to an experimental system, whereby a con-

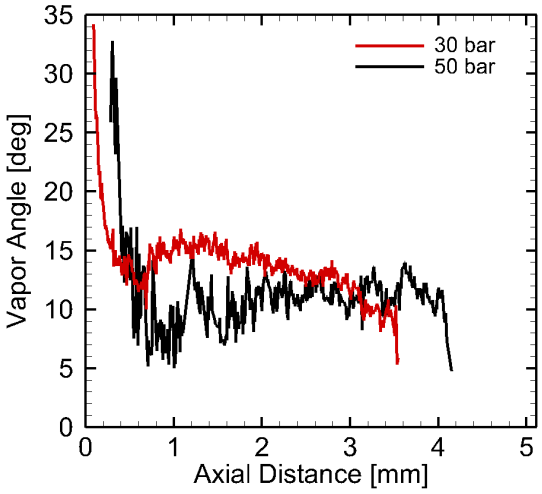

Figure 5.17: The jet spreading angle is plotted for both the 30 bar (red line) and 50 bar (black line) at 3.2 ms ASOI.

stant pressure flow rig was used in conjunction with rainbow schlieren deflectometry (RSD) to evaluate fully supercritical mixing by acquiring statistically significant dataset (100 injections). Two cases were used for comparison: a supercritical jet injected into a 1) supercritical environment or fully supercritical mixing, and 2) subcritical environment or transcritical mixing at the same density. RSD was used to measure jet boundary and penetration, spreading angle, jet velocity, and liquid detection. The results showed that fully supercritical mixing exhibited velocities 50% greater than the transcritical case. The velocity discrepancy was further investigated by using an in-house long range microscopy RSD system to study near field effects. Interestingly, the transcritical mixing case indicated extremely small droplet formation (<= 8μm) occurring along the shear layer due to to the reassertion of surface tension. Also, the transcritical case exhibited bell-shaped expansion in the near field as opposed to the linear growth rate observed in the fully supercritical case. This is due to the ambient conditions promoting vapor phase expansion for the transcritical case. Fully supercritical mixing provides several benefits for combustion system, i.e., faster mixing times (50% higher velocities), the absence of droplets which cause high levels of particulate emissions, etc. However, for diesel engines, it would be difficult to achieve in practice due to the requirements of fuels with low critical temperature and/or substantial fuel preheating.

CHAPTER 6
CONCLUSION

6.1 Summary

The present research advances RSD to study turbulent fuel sprays including the effects of supercritical mixing in CI engine environment. This is accomplished by combining several facets from turbulent gas jets, multi-phase fuel sprays, and non-ideal gas mixing - all present in fuel sprays - to develop novel methodologies for extending quantitative RSD to these unexplored areas. Each of the methodologies developed for the three areas are validated using data from the literature.

Tools developed for RSD are applied to study supercritical mixing in a CI environment. To achieve supercritical mixing, the necessary theoretical background is developed for binary mixtures. The theory is then applied in an experimental environment, in which supercritical propane is injected into a constant pressure flow rig containing nitrogen. A supercritical (fully supercritical mixing) and subcritical (transcritical mixing) ambient environment at the same density are used to evaluate potential differences due to fully supercritical mixing. The results demonstrate that fully supercritical mixing exhibited velocities 50% greater than the transcritical case. Examining near field behavior using a long range microscopy RSD system, coupled with image processing techniques discussed in Chapter 3, revealed that the discrepancies were caused from extremely small droplet formation ($<= 8\mu m$) occurring along the shear layer. The conditions in the transcritical mixing case promote mixing driven droplet condensation. Also, the ambient conditions in the transcritical mixing case promoted vapor phase expansion in the near field that caused rapid expansion as opposed to the linear growth rate observed in the fully supercritical case. Fully supercritical mixing provides several benefits for combustion systems, i.e., faster mixing times (50% higher velocities), the absence of droplets which cause high

levels of particulate emissions, etc. In diesel engines, however, this is difficult to achieve in practice due to the requirements of fuels with low critical temperature and/or substantial fuel preheating.

Several other important outcomes from the proceeding chapters are as follows:

- Chapter 2 demonstrated that RSD provides accurate full field (at the nozzle exit to 30 diameters downstream) helium concentration measurements in a turbulent helium jet for both time resolved and long exposure experiments. Also, transitional analysis of the helium jet revealed that transition on average spans a range of axial distances that decreases with increasing Reynolds number. A higher momentum provides a stabilising effect which narrows the band of transitional distances.

- In Chapter 3, RSD was applied to multi-phase fuel sprays to delineate phase boundaries transient in multi-phase fuel sprays by measuring the existence of liquid along the line of sight on a probabilistic basis. The methodology provides liquid boundaries within which liquid is always present (95 percent probability of liquid) and the outer liquid boundaries outside of which liquid is unlikely to be present (zero probability of liquid). Also, the technique allows for transient analysis of various boundary lengths and cone angles throughout the injection period. Results show that after an initial ramp-up, the liquid boundary length continues to increase, albeit slowly, indicating that a true "steady-state" might not exist in diesel combustion.

- Chapter 4 gives several important conclusions for optical and thermodynamic properties in real gas mixing scenarios. 1) The original Lorentz-Lorenz equation should be used instead of the simplified Dale-Gladstone equation to eliminate unwarranted errors that can affect the thermophysical property calculations. 2) For liquids, both polarizability and density are nearly constant. However, for non-polar gases, the polarizability is nearly constant while density varies significantly with pressure. In contrast, density variation with pressure is linear in the ideal-gas regime, but highly non-linear near the critical point and phase change boundaries of component species

and mixture. 3) Following the additive principle (e.g., Amagat law), the mixture laws for Lorentz-Loretz equation can be expressed as mole weighted sum of component refractivity (product of polarizability and density) or polarizability. For incompressible liquids (constant density) or ideal gases (linear variation in density with pressure), both formulations yield the same result. However, they are different when density varies non-linearly with pressure, for example, near the critical point and/or phase boundaries of components or mixture. 4) In the ideal-gas regime, the IG, AR, and AP models are equivalent. In the compressed liquid region where density is linear with mixture fraction, the AR and AP models are equivalent. 5) In the non-linear density regime, the IG and AR models can be highly inaccurate. The AR model performs poorly across the entire range of compression ignition conditions, yielding errors in equivalence ratio of up to 80%. 6) The AP model works well across the entire compression ignition engine regimes including conditions near the critical point and phase boundaries. The IG model is valid in the vapor region (assuming it is known) at the typical compression ignition engine operating conditions. However, IG model could introduce large errors if inadvertently applied to the two-phase region, for example, in CFD analysis.

6.2 Future Scope and Recommendations

The scope of this research has led to many important outcomes, the most significant of which is achieving and quantifying supercritical mixing in a CI environment using RSD. These findings have also identified several potential future investigations. Some of which are listed below:

- In order to apply RSD to obtain quantitative thermodynamic measurements in fuel sprays several tasks need to be addressed. First, because fuel sprays generally occur in a non-quiescent background, the calibration process needs to be more robust to handle background density gradients. One recommendation would be to calibrate at running conditions while also increasing the number of calibration images acquired at each step to drive down precision uncertainty. Second, the current average

relationship between mole fraction and refractive index is only valid if the function is linear. In non-linear scenarios (non-ideal gas portion in fuel sprays), the mean mole fraction needs to be evaluated by considering the pdf of refractive index.

- Thermodynamic variance measurements are theoretically possible [56]. The theory however, has not been validated in an experimental system. Providing validation to this concept would be an important step forward for using RSD to obtain higher order statistical thermodynamic mixing measurements.

- Use RSD to provide thermodynamic measurements in supercritical sprays to further investigate supercritical mixing behavior.

REFERENCES

[1] GN Abramovich. The theory of turbulent jets,(1963). *R411*, page 541, 1963.

[2] HJ Achtermann, G Magnus, and TK Bose. Refractivity virial coefficients of gaseous ch4, c2h4, c2h6, co2, sf6, h2, n2, he, and ar. *The Journal of chemical physics*, 94(8):5669–5684, 1991.

[3] Anne Adam, Philippe Leick, Gerd Bittlinger, and Christof Schulz. Visualization of the evaporation of a diesel spray using combined mie and rayleigh scattering techniques. *Experiments in fluids*, 47(3):439–449, 2009.

[4] A Agrawal, K Alammar, and S Gollahalli. Application of rainbow schlieren deflectometry to measure temperature and oxygen concentration in a laminar gas-jet diffusion flame. *Experiments in fluids*, 32(6):689–691, 2002.

[5] Ajay K Agrawal and C Taber Wanstall. Rainbow schlieren deflectometry for scalar measurements in fluid flows. *Journal of Flow Visualization and Image Processing*, 25(3-4), 2018.

[6] AK Agrawal, SM Cherry, and SR Gollahalli. Effects of buoyancy on steady hydrogen gas-jet diffusion flames. *Combustion science and technology*, 140(1-6):51–68, 1998.

[7] K Al-Ammar, AK Agrawal, SR Gollahalli, and DeVon Griffin. Application of rainbow schlieren deflectometry for concentration measurements in an axisymmetric helium jet. *Experiments in fluids*, 25(2):89–95, 1998.

[8] Burt W Albers and Ajay K Agrawal. Schlieren analysis of an oscillating gas-jet diffusion flame. *Combustion and flame*, 119(1-2):84–94, 1999.

[9] DE Aspnes. Local-field effects and effective-medium theory: a microscopic perspective. *American Journal of Physics*, 50(8):704–709, 1982.

[10] Mikhail V Avdeev, Aleksei N Konovalov, Viktor N Bagratashvili, Vladimir K Popov, Svetlana I Tsypina, Maia Sokolova, Jie Ke, and Martyn Poliakoff. The fibre optic reflectometer: A new and simple probe for refractive index and phase separation measurements in gases, liquids and supercritical fluids. *Physical Chemistry Chemical Physics*, 6(6):1258–1263, 2004.

[11] MEA Bardsley, Philip G Felton, and FV Bracco. 2-d visualization of liquid and vapor fuel in an ic engine. *SAE transactions*, pages 281–291, 1988.

[12] Ian H Bell and Eric W Lemmon. Automatic fitting of binary interaction parameters for multi-fluid helmholtz-energy-explicit mixture models. *Journal of Chemical & Engineering Data*, 61(11):3752–3760, 2016.

[13] Ramón Bosque and Joaquim Sales. Polarizabilities of solvents from the chemical composition. *Journal of chemical information and computer sciences*, 42(5):1154–1163, 2002.

[14] Ronald Newbold Bracewell and Ronald N Bracewell. *The Fourier transform and its applications*, volume 31999. McGraw-Hill New York, 1986.

[15] Kenneth A Buch and Werner JA Dahm. Experimental study of the fine-scale structure of conserved scalar mixing in turbulent shear flows. part 2. sc≈1. *Journal of Fluid Mechanics*, 364:1–29, 1998.

[16] AD Buckingham. The molecular refraction of an imperfect gas. *Transactions of the Faraday Society*, 52:747–753, 1956.

[17] AD Buckingham and JA Pople. The dielectric constant of an imperfect non-polar gas. *Transactions of the Faraday Society*, 51:1029–1035, 1955.

[18] AD Buckingham and JA Pople. Electromagnetic properties of compressed gases. *Discussions of the Faraday Society*, 22:17–21, 1956.

[19] AD Buckingham and RE Raab. The dielectric constant of a compressed gas mixture. *Transactions of the Faraday Society*, 54:623–628, 1958.

[20] Subrahmanyan Chandrasekhar. *Hydrodynamic and hydromagnetic stability*. Courier Corporation, 2013.

[21] B Chehroudi, D Talley, and E Coy. Visual characteristics and initial growth rates of round cryogenic jets at subcritical and supercritical pressures. *Physics of Fluids*, 14(2):850–861, 2002.

[22] Ching Jen Chen and Wolfgang Rodi. Vertical turbulent buoyant jets: a review of experimental data. *Nasa STI/Recon Technical Report A*, 80, 1980.

[23] ANDREW R Chraplyvy. Nonintrusive measurements of vapor concentrations inside sprays. *Applied Optics*, 20(15):2620–2624, 1981.

[24] Fabrizio Croccolo, Marc-Alexandre Arnaud, Didier Bégué, and Henri Bataller. Concentration dependent refractive index of a binary mixture at high pressure. *The Journal of chemical physics*, 135(3):034901, 2011.

[25] Cyril Crua, Julien Manin, and Lyle M Pickett. On the transcritical mixing of fuels at diesel engine conditions. *Fuel*, 208:535–548, 2017.

[26] Rainer N Dahms. Understanding the breakdown of classic two-phase theory and spray atomization at engine-relevant conditions. *Physics of Fluids*, 28(4):042108, 2016.

[27] Rainer N Dahms, Julien Manin, Lyle M Pickett, and Joseph C Oefelein. Understanding high-pressure gas-liquid interface phenomena in diesel engines. *Proceedings of the Combustion Institute*, 34(1):1667–1675, 2013.

[28] Rainer N Dahms and Joseph C Oefelein. On the transition between two-phase and single-phase interface dynamics in multicomponent fluids at supercritical pressures. *Physics of Fluids*, 25(9):092103, 2013.

[29] Rainer N Dahms and Joseph C Oefelein. Liquid jet breakup regimes at supercritical pressures. *Combustion and Flame*, 162(10):3648–3657, 2015.

[30] Rainer N Dahms and Joseph C Oefelein. Non-equilibrium gas–liquid interface dynamics in high-pressure liquid injection systems. *Proceedings of the Combustion Institute*, 35(2):1587–1594, 2015.

[31] MR Davis. Measurements in a subsonic turbulent jet using a quantitative schlieren technique. *Journal of Fluid Mechanics*, 46(4):631–656, 1971.

[32] MR Davis. Quantitative schlieren measurements in a supersonic turbulent jet. *Journal of Fluid Mechanics*, 51(3):435–447, 1972.

[33] MR Davis. Intensity, scale and convection of turbulent density fluctuations. *Journal of Fluid Mechanics*, 70(3):463–479, 1975.

[34] Chris De Boer, Gary Bonar, Shizuo Sasaki, and Shreeram Shetty. Application of supercritical gasoline injection to a direct injection spark ignition engine for particulate reduction. Technical report, SAE Technical Paper, 2013.

[35] John E Dec. A conceptual model of dl diesel combustion based on laser-sheet imaging. *SAE transactions*, pages 1319–1348, 1997.

[36] Jérôme Dechoz and Claude Rozé. Surface tension measurement of fuels and alkanes at high pressure under different atmospheres. *Applied surface science*, 229(1-4):175–182, 2004.

[37] JM Desantes, José María García-Oliver, JM Pastor, A Pandal, E Baldwin, and DP Schmidt. Coupled/decoupled spray simulation comparison of the ecn spray a condition with the σ-y eulerian atomization model. *International Journal of Multiphase Flow*, 80:89–99, 2016.

[38] DAVID DOWLING and PAUL DIMOTAKIS. On mixing and structure of the concentration field of turbulent jets. In *1st National Fluid Dynamics Conference*, page 3611, 1988.

[39] David R Dowling. The estimated scalar dissipation rate in gas-phase turbulent jets. *Physics of Fluids A: Fluid Dynamics*, 3(9):2229–2246, 1991.

[40] David R Dowling and Paul E Dimotakis. Similarity of the concentration field of gas-phase turbulent jets. *Journal of Fluid Mechanics*, 218:109–141, 1990.

[41] Christoph Espey, John E Dec, Thomas A Litzinger, and Domenic A Santavicca. Planar laser rayleigh scattering for quantitative vapor-fuel imaging in a diesel jet. *Combustion and flame*, 109(1-2):65–86, 1997.

[42] Zachary Falgout, Mattias Rahm, David Sedarsky, and Mark Linne. Gas/fuel jet interfaces under high pressures and temperatures. *Fuel*, 168:14–21, 2016.

[43] Zachary Falgout, Mattias Rahm, Zhenkan Wang, and Mark Linne. Evidence for supercritical mixing layers in the ecn spray a. *Proceedings of the Combustion Institute*, 35(2):1579–1586, 2015.

[44] Philip G Felton, Frediano V Bracco, and Mark EA Bardsley. On the quantitative application of exciplex fluorescence to engine sprays. *SAE Transactions*, pages 1254–1262, 1993.

[45] Jose M Garcia-Oliver, Jose M Pastor, Adrian Pandal, Nathaniel Trask, Eli Baldwin, and David P Schmidt. Diesel spray cfd simulations based on the σ-y eulerian atomization model. *Atomization and Sprays*, 23(1):71–95, 2013.

[46] WC Gardiner Jr, Y Hidaka, and T Tanzawa. Refractivity of combustion gases. *Combustion and Flame*, 40:213–219, 1981.

[47] Sibel Geacai, Irina Nita, Olga Iulian, and Elis Geacai. Refractive indices for biodiesel mixtures. *UPB Sci. Bull. Ser. B*, 74:149–160, 2012.

[48] C Giraudet, L Marlin, Didier Bégué, F Croccolo, and H Bataller. Concentration dependent refractive index of co2/ch4 mixture in gaseous and supercritical phase. *The Journal of Chemical Physics*, 144(13):134304, 2016.

[49] Dario L Goldfarb, Diego P Fernández, and Horacio R Corti. Dielectric and volumetric properties of supercritical carbon dioxide (1)+ methanol (2) mixtures at 323.15 k. *Fluid phase equilibria*, 158:1011–1019, 1999.

[50] Paul S Greenberg, Robert B Klimek, and Donald R Buchele. Quantitative rainbow schlieren deflectometry. *Applied Optics*, 34(19):3810–3825, 1995.

[51] Alan H Harvey and Eric W Lemmon. Method for estimating the dielectric constant of natural gas mixtures. *International journal of thermophysics*, 26(1):31–46, 2005.

[52] Cherian A Idicheria and Lyle M Pickett. Quantitative mixing measurements in a vaporizing diesel spray by rayleigh imaging. Technical report, SAE Technical Paper, 2007.

[53] Kemar C James, Jin Wang, Michael C Maynard, Zackery B Morris, and Brian T Fisher. Development of a high-pressure, high-temperature, optically accessible continuous-flow vessel for fuel-injection experiments. *Journal of Engineering for Gas Turbines and Power*, 136(9):091512, 2014.

[54] Pankaj S Kolhe and Ajay K Agrawal. Abel inversion of deflectometric data: comparison of accuracy and noise propagation of existing techniques. *Applied optics*, 48(20):3894–3902, 2009.

[55] Pankaj S Kolhe and Ajay K Agrawal. Density measurements in a supersonic microjet using miniature rainbow schlieren deflectometry. *AIAA journal*, 47(4):830–838, 2009.

[56] Pankaj S Kolhe and Ajay K Agrawal. A novel spectral analysis algorithm to obtain local scalar field statistics from line-of-sight measurements in turbulent flows. *Measurement Science and Technology*, 20(11):115402, 2009.

[57] Seok Jae Kwon and Il Won Seo. Reynolds number effects on the behavior of a non-buoyant round jet. *Experiments in fluids*, 38(6):801–812, 2005.

[58] Guilhem Lacaze, Antony Misdariis, Anthony Ruiz, and Joseph C Oefelein. Analysis of high-pressure diesel fuel injection processes using les with real-fluid thermodynamics and transport. *Proceedings of the Combustion Institute*, 35(2):1603–1611, 2015.

[59] HS Lee, AC Fernandez-Pello, GM Corcos, and AK Oppenheim. A mixing and deformation mechanism for a supercritical fuel droplet. *Combustion and Flame*, 81(1):50–58, 1990.

[60] Eric W Lemmon and Richard T Jacobsen. A new functional form and new fitting techniques for equations of state with application to pentafluoroethane (hfc-125). *Journal of Physical and Chemical Reference Data*, 34(1):69–108, 2005.

[61] Eric W Lemmon and RT Jacobsen. A generalized model for the thermodynamic properties of mixtures. *International journal of thermophysics*, 20(3):825–835, 1999.

[62] Eric W Lemmon and Reiner Tillner-Roth. A helmholtz energy equation of state for calculating the thermodynamic properties of fluid mixtures. *Fluid phase equilibria*, 165(1):1–21, 1999.

[63] EW Lemmon, ML Huber, and MO McLinden. Refprop 9.1. *NIST standard reference database*, 23, 2013.

[64] Paul A Libby. *An introduction to turbulence*. CRC Press, 1996.

[65] Yangang Liu and Peter H Daum. Relationship of refractive index to mass density and self-consistency of mixing rules for multicomponent mixtures like ambient aerosols. *Journal of Aerosol Science*, 39(11):974–986, 2008.

[66] Fritz London. The general theory of molecular forces. *Transactions of the Faraday Society*, 33:8b–26, 1937.

[67] Hendrik Antoon Lorentz. *The Theory of Electrons and Its Applications to the Phenomena of Light and Radiant Heart: A Course of Lectures Delivered in Columbia University, New York in March and April, 1906*, volume 29. Teubner, 1916.

[68] Julien Manin, Michele Bardi, Lyle M Pickett, RN Dahms, and JC Oefelein. Microscopic investigation of the atomization and mixing processes of diesel sprays injected into high pressure and temperature environments. *Fuel*, 134:531–543, 2014.

[69] E Mastorakos, M Shibasaki, and Koichi Hishida. Mixing enhancement in axisymmetric turbulent isothermal and buoyant jets. *Experiments in fluids*, 20(4):279–290, 1996.

[70] W Mayer, A Schik, M Schaf fler, and H Tamura. Injection and mixing processes in high-pressure liquid oxygen/gaseous hydrogen rocket combustors. *Journal of Propulsion and Power*, 16(5):823–828, 2000.

[71] Wolfgang Mayer and Hiroshi Tamura. Propellant injection in a liquid oxygen/-gaseous hydrogen rocket engine. *Journal of Propulsion and Power*, 12(6):1137–1147, 1996.

[72] Wolfgang Meier, Robert S Barlow, Y-L Chen, and J-Y Chen. Raman/rayleigh/lif measurements in a turbulent ch4/h2/n2 jet diffusion flame: experimental techniques and turbulence–chemistry interaction. *Combustion and Flame*, 123(3):326–343, 2000.

[73] Lynn A Melton. Spectrally separated fluorescence emissions for diesel fuel droplets and vapor. *Applied Optics*, 22(14):2224–2226, 1983.

[74] Lynn A Melton and James F Verdieck. Vapor/liquid visualization for fuel sprays. *Combustion Science and Technology*, 42(3-4):217–222, 1985.

[75] Richard B Miles, Walter R Lempert, and Joseph N Forkey. Laser rayleigh scattering. *Measurement Science and Technology*, 12(5):R33, 2001.

[76] Eileen M Mirynowski, Ajay K Agrawal, and Joshua A Bittle. High-speed rainbow schlieren deflectometry of n-heptane sprays using a common rail diesel injector. *Journal of Energy Resources Technology*, 139(6):062205, 2017.

[77] Dhiren Mistry, Jimmy Philip, James R Dawson, and Ivan Marusic. Entrainment at multi-scales across the turbulent/non-turbulent interface in an axisymmetric jet. *Journal of Fluid Mechanics*, 802:690–725, 2016.

[78] Mark PB Musculus and Kyle Kattke. Entrainment waves in diesel jets. *SAE International Journal of Engines*, 2(1):1170–1193, 2009.

[79] Jeffrey D Naber and Dennis L Siebers. Effects of gas density and vaporization on penetration and dispersion of diesel sprays. *SAE transactions*, pages 82–111, 1996.

[80] Keiya Nishida and Hiroyuki Hiroyasu. Simplified three-dimensional modeling of mixture formation and combustion in a di diesel engine. *SAE transactions*, pages 276–293, 1989.

[81] Joseph Oefelein, Rainer Dahms, and Guilhem Lacaze. Detailed modeling and simulation of high-pressure fuel injection processes in diesel engines. *SAE International Journal of Engines*, 5(3):1410–1419, 2012.

[82] Joseph Oefelein, Guilhem Lacaze, Rainer Dahms, Anthony Ruiz, and Antony Misdariis. Effects of real-fluid thermodynamics on high-pressure fuel injection processes. *SAE International Journal of Engines*, 7(3):1125–1136, 2014.

[83] Panos N Papanicolaou and E John List. Investigations of round vertical turbulent buoyant jets. *Journal of Fluid Mechanics*, 195:341–391, 1988.

[84] José V Pastor, José M García, José M Pastor, and L Daniel Zapata. Evaporating diesel spray visualization using a double-pass shadowgraphy/schlieren imaging. Technical report, SAE Technical Paper, 2007.

[85] Jose V Pastor, Jose J Lopez, J Enrique Juliá, and Jesús V Benajes. Planar laser-induced fluorescence fuel concentration measurements in isothermal diesel sprays. *Optics Express*, 10(7):309–323, 2002.

[86] Kasyap S Pasumarthi and Ajay K Agrawal. Schlieren measurements and analysis of concentration field in self-excited helium jets. *Physics of Fluids*, 15(12):3683–3692, 2003.

[87] Raul Payri, Jose M García-Oliver, Michele Bardi, and Julien Manin. Fuel temperature influence on diesel sprays in inert and reacting conditions. *Applied Thermal Engineering*, 35:185–195, 2012.

[88] BJ Pelliccia-Kraft and DW Watt. Three-dimensional imaging of a turbulent jet using shearing interferometry and optical tomography. *Experiments in fluids*, 29(6):573–581, 2000.

[89] LM Pickett, G Bruneaux, and R Payri. Engine combustion network. *Sandia National Laboratories, Livermore, CA, http://www. ca. sandia. gov/ecn*, 2014.

[90] Lyle M Pickett, Caroline L Genzale, Gilles Bruneaux, Louis-Marie Malbec, Laurent Hermant, Caspar Christiansen, and Jesper Schramm. Comparison of diesel spray combustion in different high-temperature, high-pressure facilities. *SAE International Journal of Engines*, 3(2):156–181, 2010.

[91] Lyle M Pickett, Julien Manin, Caroline L Genzale, Dennis L Siebers, Mark PB Musculus, and Cherian A Idicheria. Relationship between diesel fuel spray vapor penetration/dispersion and local fuel mixture fraction. *SAE International Journal of Engines*, 4(1):764–799, 2011.

[92] William M Pitts. Effects of global density ratio on the centerline mixing behavior of axisymmetric turbulent jets. *Experiments in Fluids*, 11(2-3):125–134, 1991.

[93] William M Pitts. Reynolds number effects on the mixing behavior of axisymmetric turbulent jets. *Experiments in fluids*, 11(2-3):135–141, 1991.

[94] William M Pitts and Takashi Kashiwagi. The application of laser-induced rayleigh light scattering to the study of turbulent mixing. *Journal of Fluid Mechanics*, 141:391–429, 1984.

[95] Ludwig Prandtl. 7. bericht über untersuchungen zur ausgebildeten turbulenz. *ZAMM-Journal of Applied Mathematics and Mechanics/Zeitschrift für Angewandte Mathematik und Mechanik*, 5(2):136–139, 1925.

[96] William C Reynolds and Piero Colonna. *Thermodynamics*. Cambridge University Press, 2018.

[97] Cecilia D Richards, William M Pitts, et al. Global density effects on the self-preservation behaviour of turbulent free jets. *Journal of Fluid Mechanics*, 254:417–417, 1993.

[98] Arnab Roy, Clement Joly, and Corin Segal. Disintegrating supercritical jets in a subcritical environment. *Journal of Fluid Mechanics*, 717:193–202, 2013.

[99] Arnab Roy and Corin Segal. Experimental study of fluid jet mixing at supercritical conditions. *Journal of Propulsion and Power*, 26(6):1205–1211, 2010.

[100] James W Schmidt and Michael R Moldover. Dielectric permittivity of eight gases measured with cross capacitors. *International Journal of Thermophysics*, 24(2):375–403, 2003.

[101] C Segal and SA Polikhov. Subcritical to supercritical mixing. *Physics of Fluids*, 20(5):052101, 2008.

[102] J Shinjo and A Umemura. Simulation of liquid jet primary breakup: Dynamics of ligament and droplet formation. *International Journal of Multiphase Flow*, 36(7):513–532, 2010.

[103] JS Shuen, Vigor Yang, and CC Hsiao. Combustion of liquid-fuel droplets in supercritical conditions. *Combustion and Flame*, 89(3-4):299–319, 1992.

[104] Dennis L Siebers. Liquid-phase fuel penetration in diesel sprays. Technical report, SAE technical paper, 1998.

[105] Dennis L Siebers. Scaling liquid-phase fuel penetration in diesel sprays based on mixing-limited vaporization. *SAE transactions*, pages 703–728, 1999.

[106] Roland Span. *Multiparameter equations of state: an accurate source of thermodynamic property data*. Springer Science & Business Media, 2013.

[107] LK Su, DB Helmer, and CJ Brownell. Quantitative planar imaging of turbulent buoyant jet mixing. *Journal of fluid mechanics*, 643:59–95, 2010.

[108] Yongda Sun, Boris Y Shekunov, and Peter York. Refractive index of supercritical co 2-ethanol solvents. *Chemical Engineering Communications*, 190(1):1–14, 2003.

[109] Mamoru Suzuki, Keiya Nishida, and Hiroyuki Hiroyasu. Simultaneous concentration measurement of vapor and liquid in an evaporating diesel spray. *SAE Transactions*, pages 1164–1186, 1993.

[110] Lev Aleksandrovich Vasil′ev. *Schlieren methods*. Israel Program;[distributed by Keter Inc.] New York, 1971.

[111] Jin Wang, Eileen M Mirynowski, Joshua A Bittle, and Brian T Fisher. Experimental measurements of n-heptane liquid penetration distance and spray cone angle for steady conditions relevant to early direct-injection low-temperature combustion in diesel engines. *International Journal of Engine Research*, 17(4):371–390, 2016.

[112] Xingjian Wang, Hongfa Huo, Umesh Unnikrishnan, and Vigor Yang. A systematic approach to high-fidelity modeling and efficient simulation of supercritical fluid mixing and combustion. *Combustion and Flame*, 195:203–215, 2018.

[113] C Taber Wanstall, Ajay K Agrawal, and Joshua A Bittle. Quantifying liquid boundary and vapor distributions in a fuel spray by rainbow schlieren deflectometry. *Applied optics*, 56(30):8385–8393, 2017.

[114] C Taber Wanstall, Ajay K Agrawal, and Joshua A Bittle. Phase boundary detection in transient, evaporating high-pressure fuel sprays by rainbow schlieren deflectometry. *Applied optics*, 58(25):6791–6801, 2019.

[115] C Taber Wanstall, Ajay K Agrawal, and Joshua A Bittle. Phase boundary detection in transient, evaporating high-pressure fuel sprays by rainbow schlieren deflectometry. *Applied Optics*, 2019.

[116] T Watanabe, Y Sakai, K Nagata, Y Ito, and T Hayase. Enstrophy and passive scalar transport near the turbulent/non-turbulent interface in a turbulent planar jet flow. *Physics of Fluids*, 26(10):105103, 2014.

[117] DW Watt and Charles M Vest. Turbulent flow visualization by interferometric integral imaging and computed tomography. *Experiments in fluids*, 8(6):301–311, 1990.

[118] J Westerweel, C Fukushima, JM Pedersen, and JCR Hunt. Mechanics of the turbulent-nonturbulent interface of a jet. *Physical review letters*, 95(17):174501, 2005.

[119] J Westerweel, T Hofmann, C Fukushima, and J Hunt. The turbulent/non-turbulent interface at the outer boundary of a self-similar turbulent jet. *Experiments in Fluids*, 33(6):873–878, 2002.

[120] Fredrik R Westlye, Keith Penney, Anders Ivarsson, Lyle M Pickett, Julien Manin, and Scott A Skeen. Diffuse back-illumination setup for high temporally resolved extinction imaging. *Applied optics*, 56(17):5028–5038, 2017.

[121] Tommy Wong and Ajay K Agrawal. Quantitative measurements in an unsteady flame using high-speed rainbow schlieren deflectometry. *Measurement Science and Technology*, 17(6):1503, 2006.

[122] BS Yildirim and AK Agrawal. Full-field measurements of self-excited oscillations in momentum-dominated helium jets. *Experiments in fluids*, 38(2):161–173, 2005.

[123] Yu-yin Zhang, Takuo Yoshizaki, and Keiya Nishida. Imaging of droplets and vapor distributions in a diesel fuel spray by means of a laser absorption–scattering technique. *Applied Optics*, 39(33):6221–6229, 2000.

[124] Fu-Quan Zhao and Hiroyuki Hiroyasu. The applications of laser rayleigh scattering to combustion diagnostics. *Progress in energy and combustion science*, 19(6):447–485, 1993.